


Review

The Chemistry and Mineralogy (CheMin) X-ray Diffractometer on the MSL Curiosity Rover: A Decade of Mineralogy from Gale Crater, Mars

David Blake ^{1,*}, Valerie Tu ^{2,*}, Thomas Bristow ¹, Elizabeth Rampe ³, David Vaniman ⁴, Steve Chipera ⁴, Philippe Sarrazin ⁵, Richard Morris ³, Shaunna Morrison ⁶, Albert Yen ⁷, Robert Downs ⁸, Robert Hazen ⁶, Allan Treiman ⁹, Douglas Ming ³, Gordon Downs ⁵, Cherie Achilles ¹⁰, Nicholas Castle ⁴, Tanya Peretyazhko ², David De Marais ¹, Patricia Craig ⁴, Barbara Lafuente ⁵, Benjamin Tutolo ¹¹, Elisabeth Hausrath ¹², Sarah Simpson ³, Richard Walroth ¹³, Michael Thorpe ¹⁴, Johannes Meusbürger ¹, Aditi Pandey ^{3,9}, Marc Gailhanou ¹⁵, Przemyslaw Dera ¹⁶, Jeffrey Berger ², Lucy Thompson ¹⁷, Ralf Gellert ¹⁸, Amy McAdam ¹⁰, Catherine O'Connell-Cooper ¹⁷, Brad Sutter ², John Michael Morookian ⁷, Abigail Fraeman ⁷, John Grotzinger ¹⁹, Kirsten Siebach ²⁰, Soren Madsen ⁷ and Ashwin Vasavada ⁷

¹ NASA Ames Research Center, Moffett Field, CA 94043, USA; thomas.f.bristow@nasa.gov (T.B.); david.j.desmarais@nasa.gov (D.D.M.); johannes.m.meusbuerger@nasa.gov (J.M.)

² Jacobs JETSII, NASA Johnson Space Center, Houston, TX 77058, USA; tanya.peretyazhko@nasa.gov (T.P.); jeff.berger@nasa.gov (J.B.); brad.sutter-2@nasa.gov (B.S.)

³ NASA Johnson Space Center, Houston, TX 77058, USA; elizabeth.b.rampe@nasa.gov (E.R.); richard.v.morris@nasa.gov (R.M.); douglas.w.ming@nasa.gov (D.M.); sarah.l.simpson@nasa.gov (S.S.); aditi.pandey@nasa.gov (A.P.)

⁴ Planetary Science Institute, Tucson, AZ 85719, USA; dvaniman@psi.edu (D.V.); steve.chipera@gmail.com (S.C.); nicholas.castle@gmail.com (N.C.); pcraig@psi.edu (P.C.)

⁵ SETI Institute, Mountain View, CA 94043, USA; philippe.sarrazin@examinaart.com (P.S.); gordie1997@gmail.com (G.D.); barbara.lafuente@examinaart.com (B.L.)

⁶ Carnegie Institute for Science, Washington, DC 20015, USA; smorrison@carnegiescience.edu (S.M.); rhazen@carnegiescience.edu (R.H.)

⁷ Jet Propulsion Laboratory, California Institute of Technology, Pasadena, CA 91011, USA; albert.s.yen@jpl.nasa.gov (A.Y.); johnmichael.morookian@jpl.nasa.gov (J.M.M.); abigail.a.fraeman@jpl.nasa.gov (A.F.); soren.n.madsen@jpl.nasa.gov (S.M.); ashwin.r.vasavada@jpl.nasa.gov (A.V.)

⁸ Department of Geosciences, University of Arizona, Tucson, AZ 85721, USA; rdowns@arizona.edu

⁹ The Lunar and Planetary Institute, Houston, TX 77058, USA; treiman@lpi.usra.edu

¹⁰ NASA Goddard Space Flight Center, Greenbelt, MD 20771, USA; cherie.n.achilles@nasa.gov (C.A.); amy.mcadam-1@nasa.gov (A.M.)

¹¹ University of Calgary, Calgary, AB T2N 1N4, Canada; benjamin.tutolo@ucalgary.ca

¹² University of Nevada, Las Vegas, NV 89154, USA; elisabeth.hausrath@unlv.edu

¹³ Genetech, South San Francisco, CA 94080, USA; rwalroth89@gmail.com

¹⁴ Goddard Space Flight Center/CRESST II, University of Maryland, Greenbelt, MD 20771, USA; michael.t.thorpe@nasa.gov

¹⁵ CNRS, IM2NP, 13397 Marseille, France; marc.gailhanou@im2np.fr

¹⁶ University of Hawaii, Honolulu, HI 96822, USA; pdera@hawaii.edu

¹⁷ University of New Brunswick, Fredericton, NB E3B 5A3, Canada; lthomps@unb.ca (L.T.); catoconnell@gmail.com (C.O.-C.)

¹⁸ Department of Physics, University of Guelph, Guelph, ON N1G 2W1, Canada; rgellert@uoguelph.ca

¹⁹ Division of Geologic and Planetary Sciences, California Institute of Technology, Pasadena, CA 91125, USA; grotz@gps.caltech.edu

²⁰ Rice University, Houston, TX 77005, USA; ksiebach@rice.edu

* Correspondence: david.blake@nasa.gov (D.B.); valerie.m.tu@nasa.gov (V.T.)



Citation: Blake, D.; Tu, V.; Bristow, T.; Rampe, E.; Vaniman, D.; Chipera, S.; Sarrazin, P.; Morris, R.; Morrison, S.; Yen, A.; et al. The Chemistry and Mineralogy (CheMin) X-ray Diffractometer on the MSL Curiosity Rover: A Decade of Mineralogy from Gale Crater, Mars. *Minerals* **2024**, *14*, 568. <https://doi.org/10.3390/min14060568>

Academic Editor: Leonid Dubrovinsky

Received: 7 May 2024

Revised: 25 May 2024

Accepted: 27 May 2024

Published: 29 May 2024



Copyright: © 2024 by the authors. Licensee MDPI, Basel, Switzerland. This article is an open access article distributed under the terms and conditions of the Creative Commons Attribution (CC BY) license (<https://creativecommons.org/licenses/by/4.0/>).

Abstract: For more than a decade, the CheMin X-ray diffraction instrument on the Mars Science Laboratory rover, *Curiosity*, has been returning definitive and quantitative mineralogical and mineral-chemistry data from ~3.5-billion-year-old (Ga) sediments in Gale crater, Mars. To date, 40 drilled rock samples and three scooped soil samples have been analyzed during the rover's 30+ km transit. These samples document the mineralogy of over 800 m of flat-lying fluvial, lacustrine, and aeolian sedimentary rocks that comprise the lower strata of the central mound of Gale crater (Aeolis Mons,

informally known as Mt. Sharp) and the surrounding plains (Aeolis Palus, informally known as the Bradbury Rise). The principal mineralogy of the sedimentary rocks is of basaltic composition, with evidence of post-depositional diagenetic overprinting. The rocks in many cases preserve much of their primary mineralogy and sedimentary features, suggesting that they were never strongly heated or deformed. Using aeolian soil composition as a proxy for the composition of the deposited and lithified sediment, it appears that, in many cases, the diagenetic changes observed are principally isochemical. Exceptions to this trend include secondary nodules, calcium sulfate veining, and rare Si-rich alteration halos. A surprising and yet poorly understood observation is that nearly all of the ~3.5 Ga sedimentary rocks analyzed to date contain 15–70 wt.% of X-ray amorphous material. Overall, this >800 m section of sedimentary rock explored in lower Mt. Sharp documents a perennial shallow lake environment grading upward into alternating lacustrine/fluvial and aeolian environments, many of which would have been habitable to microbial life.

Keywords: powder X-ray diffraction; Mars; extraterrestrial mineralogy; Mars science laboratory; *Curiosity* rover

1. Introduction

The Mars Science Laboratory (MSL) rover, *Curiosity*, landed in Gale crater, Mars, on 6 August 2012, and has been exploring its floor (Aeolis Palus, informally called the Bradbury Rise) and central peak (Aeolis Mons, informally called Mount Sharp) for nearly twelve Earth years. During its decade-long traverse, *Curiosity* has travelled more than 30 km and analyzed and documented over 800 vertical meters of flat-lying sedimentary rock. As part of MSL *Curiosity*'s laboratory instrument suite, the Chemistry and Mineralogy (CheMin) instrument determines the mineralogy of scooped or drilled samples delivered to it by the Sample Acquisition, Sample Processing, and Handling (SA/SPaH) system [1] or delivered directly from the drill bit. Mineralogical analysis is an invaluable technique for deciphering geologically ancient environments because, as thermodynamic phases, minerals have well-defined stability ranges of pressure, temperature, and chemical composition (P, T, X). A full knowledge of the mineralogy of a geologic sample provides insight into the conditions of its formation (paragenesis) and any subsequent changes that have occurred (diagenesis).

CheMin is a powder X-ray diffraction (pXRD) instrument [2] that can identify, quantify, and determine the structure states and major element compositions of minerals in complex polymineralic assemblages, such as volcanic rocks and sediments. Here, we describe CheMin's geometry, its mode of operation, and the techniques used to process and analyze the downlinked data. We summarize some of the major mineralogical and geochemical discoveries made during the last eleven years and discuss implications for ancient igneous processes, aqueous environments, early habitability, and the gradual drying out and oxidation of the Mars surface environment in the Hesperian (3.7–2.9 Ga) and early Amazonian (2.6 Ga–present) periods.

Gale crater is an ancient 155 km diameter impact crater that sits astride a planet-wide feature on Mars called the “dichotomy boundary” (Figure 1). This boundary separates Mars' two distinct geomorphological terranes: to the north, a relatively flat, topographically low, less cratered (and therefore younger) plain and, to the south, a topographically high, more heavily cratered, and geologically older highland. Gale crater was a deep depression in the Mars crust (4650 m below the average elevation of Mars) at a time when the Mars atmosphere was dense enough and the climate warm enough to allow liquid water to flow on its surface.

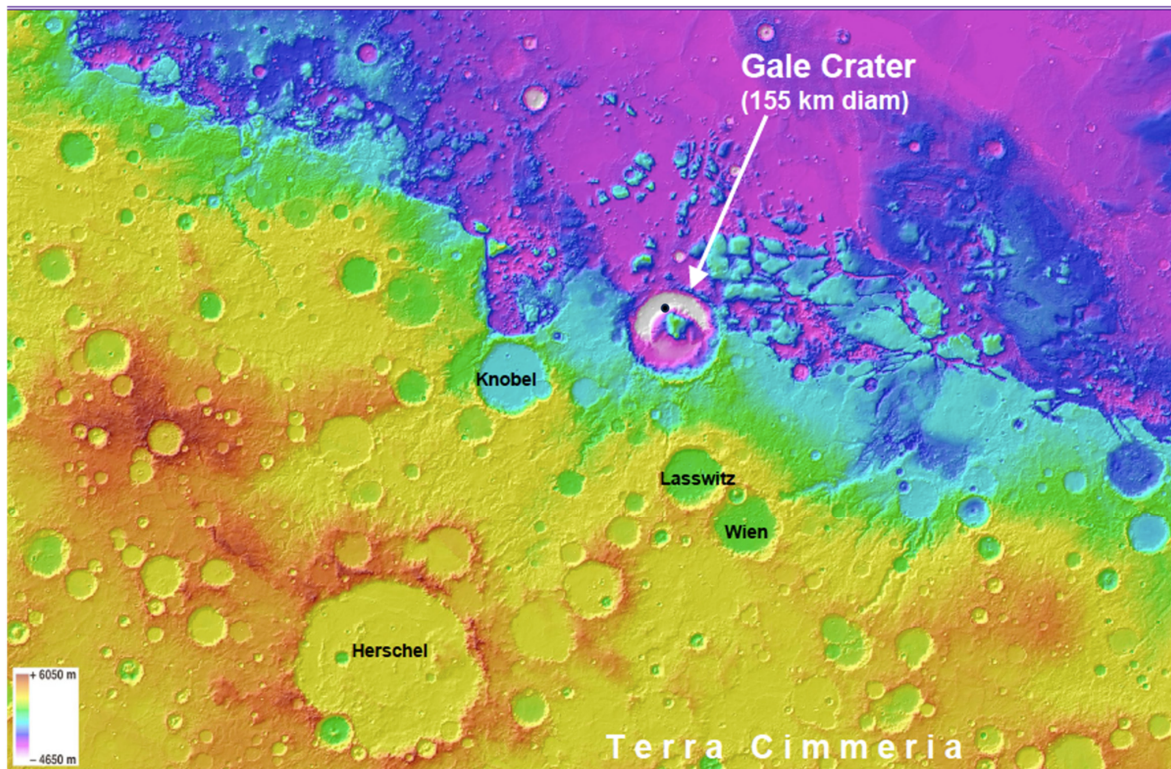


Figure 1. Color-coded topographic map of Gale crater, located near the Mars equator and sitting astride the Mars dichotomy boundary. The floor of the crater is -4650 m relative to the Mars datum (average elevation on Mars). MSL *Curiosity* landed in the white area, north of the central mound. A black dot marks the approximate position of the landing site.

Gale crater's formation dates to $\sim 3.6\text{--}3.8$ Ga [3]. Gale is one of a class of “overfilled” craters [4,5]: craters that after their formation filled with sediment, later to be partially exhumed by aeolian processes. The central peak of Gale is comprised of the remnants of this infilling sediment. Orbital infrared imagery and reflectance spectra revealed a vertical succession of sedimentary strata containing hydrous minerals (clay minerals, hydrated Mg sulfates, etc.) on lower Mt. Sharp that were hypothesized to have been formed in the presence of water (Figure 2) [6,7]. Gale crater was chosen as the landing site for MSL *Curiosity* based on these and other orbital images that were interpreted as the morphological remnants of an ancient crater lake, replete with stream channels and alluvial fans extending down from the crater's northern rim, and flat-lying laterally extensive sedimentary strata shrouding Mt. Sharp.

MSL *Curiosity* [8] brought to Gale crater a full complement of scientific instruments for characterizing surface geology and mineralogy. Optical images of surface materials were acquired with a spatial resolution of tens of microns by the Mars Hand Lens Imager, MAHLI [9], and far-field optical and near-IR imagery at the mm scale with Mastcam [10]. Quantitative compositional data were obtained from surface areas of 2–3 cm diameter using Alpha Particle X-ray Spectroscopy, APXS [11,12]. Sub-mm point-size elemental data were obtained with the Laser-Induced Breakdown Spectrometry, LIBS instrument [13] on ChemCam [14]. Mineralogical data from powdered 1 cm diameter by 6 cm deep rock cores, or scooped soils, were obtained with CheMin [2], augmented by thermally Evolved Gas Analysis (EGA) data from the Sample Analysis at Mars, SAM instrument [15], near-IR spectral imagery from Mastcam, compositional data from ChemCam-LIBS, and bulk compositional data from the APXS instrument.

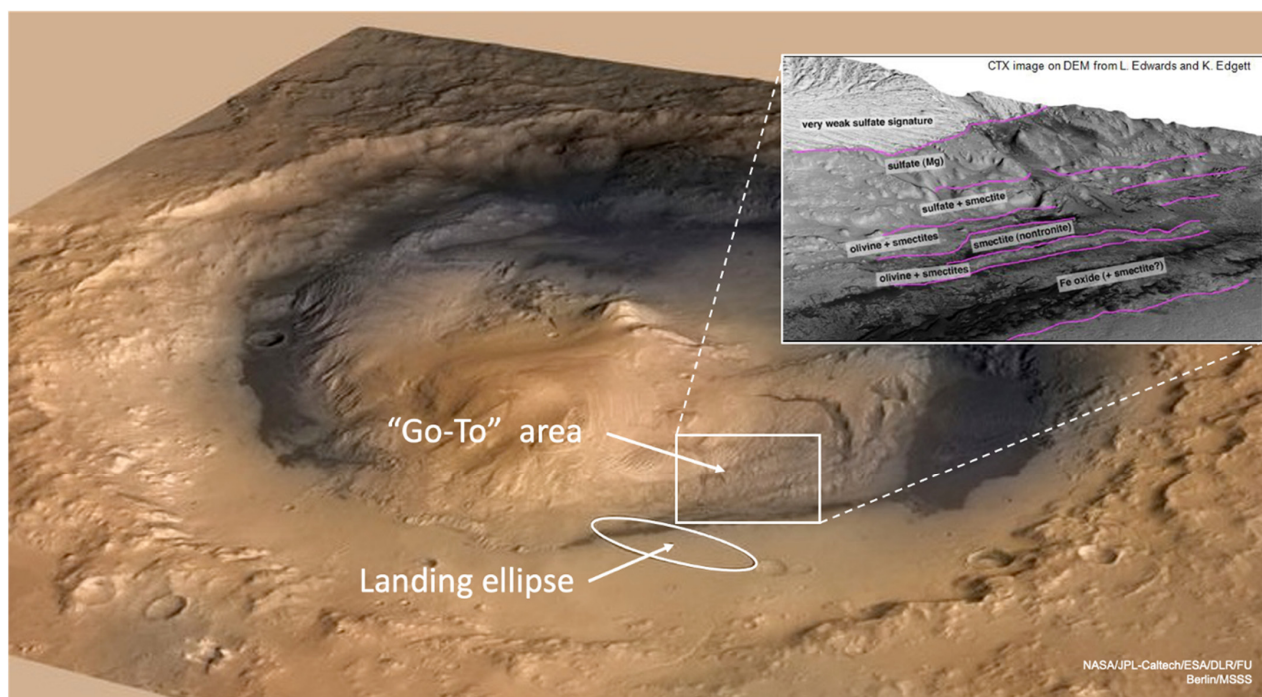


Figure 2. Oblique view, looking down on Gale crater from the north. The landing ellipse is 20 km × 6 km and represents the predicted landing area (*Curiosity* landed within 2 km of the center of the ellipse). While several CheMin analyses were performed within the landing ellipse, the rectangle south and west of the site shows the area of most interest during the mission, and the inset shows the mineral signals as seen from orbit.

2. Description of the CheMin Instrument

2.1. The CheMin Geometry

CheMin is a self-contained lunchbox-sized powder X-ray diffractometer, 30 cm × 30 cm × 30 cm, with a mass of 10 kg. (Figure 3). The geometry of the CheMin instrument is based on that of an X-ray transmission pinhole camera (Figure 4). A micro-focus cobalt anode X-ray tube, operated at 25 KeV and 100 μA, emits a cone of X-rays that is intercepted by a 70 μm collimating aperture. The collimated beam strikes the center of a transmission sample cell 8 mm in diameter and 170 μm thick, bounded by 7 μm thick X-ray transparent Mylar or Kapton windows (Figure 5a,b). The samples analyzed by CheMin consist of 50–100 mg aliquots of powdered rock or scooped soil (sieved to a grain size < 150 μm) delivered to the cell by the SA/SPaH system (midway through the mission, as a result of a failure of the drill feed mechanism, a modified sample delivery procedure was adopted in which unsieved drill powder was delivered directly to CheMin). During an analysis, the powder in the cell is shaken by piezoelectric vibration, inducing a turbulent flow of randomly oriented grains through the beam over time. Crystalline grains that pass through the beam in Bragg orientation contribute to the diffraction pattern, one photon at a time. CheMin’s sample cells are arranged in pairs on the periphery of a wheel (Figure 5c) that holds 27 cells and can be filled with sample material, analyzed, and emptied several times, plus 5 sealed cells containing diffraction and fluorescence standards for instrument health checks and calibration.

CheMin’s transmission geometry makes it susceptible to sample self-absorption, depending upon the anode material chosen for the X-ray tube. Because Mars is an iron-rich planet, a cobalt anode was chosen rather than a standard copper anode typical of laboratory instruments because CuKα photons with an energy of 8.04 KeV strongly fluoresce Fe, which has its K absorption edge at 7.11 KeV. Indeed, on an iron-rich planet like Mars, if a Cu anode were used in a transmission-geometry instrument, ordinary basaltic composition samples would appear nearly opaque to the beam. An additional performance benefit is that, while

the longer wavelength of $\text{CoK}\alpha$ results in decreased d-value coverage relative to $\text{CuK}\alpha$, the major diffraction maxima of clay minerals and those of most rock-forming minerals fall within a range for which CheMin’s 2θ resolution is optimized. The CheMin team simulated and measured the diffraction patterns of a wide variety of rock types and specific Mars-relevant minerals at 2θ resolutions, ranging from 0.1° to 0.6° . A design specification of 0.35° 2θ was chosen as the minimum (worst) resolution that would still allow the identification of virtually all minerals thought to be on Mars. Changes in the geometry of the instrument could of course result in improved resolution, but only at the expense of count rate, detector size, or overall instrument dimensions—critical factors in spacecraft instrument design. Figure 6 shows a ray-tracing simulation of the CheMin geometry, illustrating its range and 2θ resolution. The CheMin flight instrument collects diffraction data over a 2θ range of 3° to 53° ($\text{CoK}\alpha$) with a Full Width at Half Maximum (FWHM) figure of merit ranging from 0.25° to 0.35° 2θ , sufficient to discriminate virtually all minerals in complex mixtures. Plotted on the 2θ resolution curves in Figure 6 are FWHM peak widths for the four diffraction standards on the CheMin sample wheel. Despite CheMin’s relatively poor 2θ resolution, Rietveld refinement and other whole-pattern fitting techniques can nevertheless be used to identify, quantify, and determine the lattice parameters and crystal chemistry of virtually all minerals.

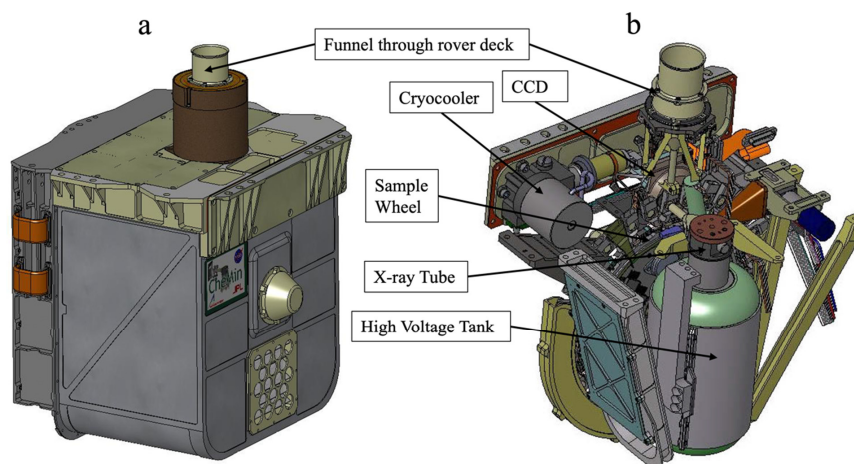


Figure 3. The CheMin XRD/XRF instrument, 30 cm × 30 cm × 30 cm, 10 kg. (a) The SA/SPaH delivers a sieved aliquot of powdered rock or soil through the funnel located at the top of the instrument, which penetrates the upper deck of the rover. (b) Internal components of the instrument (the image is rotated 180° about the vertical axis from (a), for clarity).

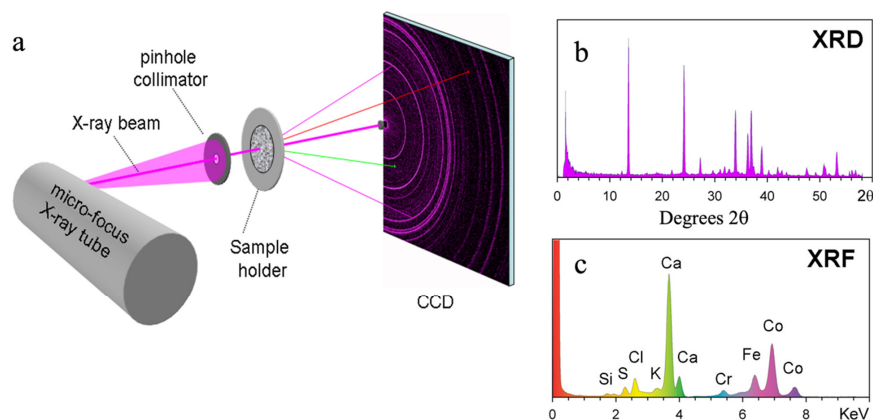


Figure 4. Geometry of the CheMin instrument. (a) Overall geometry of CheMin. (b) XRD 2θ plot obtained by summing diffracted photons from the characteristic $\text{K}\alpha$ line of the X-ray source ($\text{CoK}\alpha$ X-rays colored magenta in (a)). (c) X-ray energy-dispersive histogram (EDH) obtained by summing all X-ray photons detected by the CCD, with fluoresced photons from the sample shown schematically in green and red in (a).

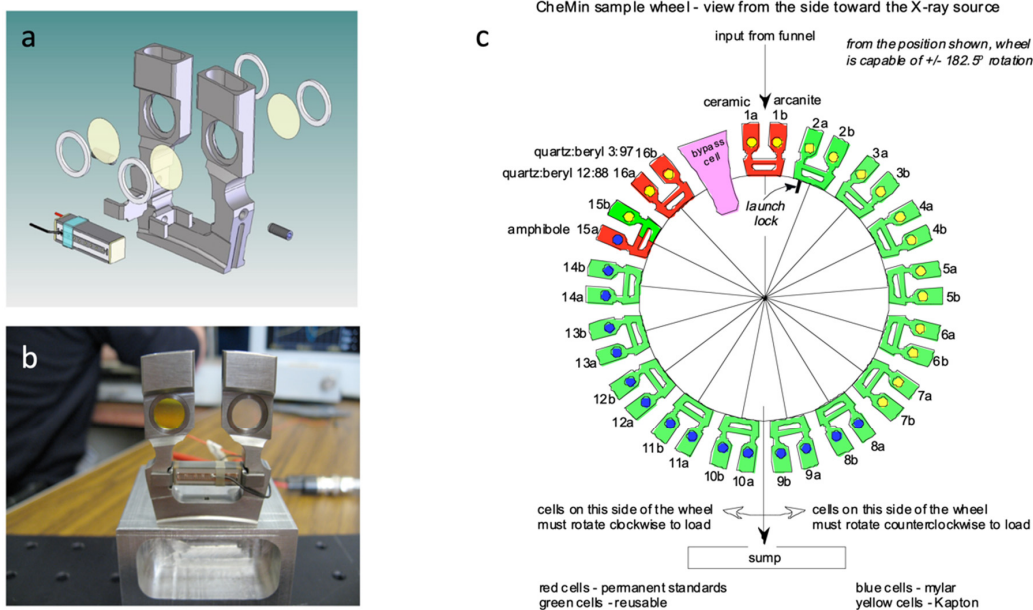


Figure 5. CheMin cell geometry. (a) Exploded view of dual-cell assembly, showing windows, tuning-fork assembly and piezodriver. (b) Assembled cell, ready for testing (Yellow Kapton window on left, clear mylar window on right). (c) The CheMin sample wheel, showing the location of sealed standard cells and open cells used for powder samples delivered by the SA/SPaH system. The cells are filled and analyzed at the top, then rotated 180° and emptied into a sump at the bottom of the instrument.

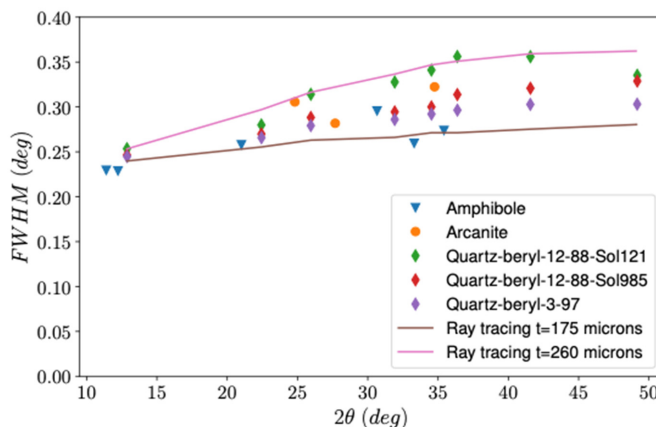


Figure 6. Measured FWHM peak widths for CheMin’s five standards (symbols) vs. ray-tracing results for 175 μm and 260 μm sample widths that best bracket the measured data. Cell windows are mounted on either side of a 170 μm spacer in the cell, yielding a nominal sample thickness of 170 μm. However, piezovibration during analysis causes the windows to beat like a drum, which increases the effective sample thickness in some cases.

2.2. The CheMin Detector and CheMin Data Products

Diffraction and fluoresced photons from the sample are directly detected by CheMin’s image sensor, a 2.5 cm square Charge Coupled Device (CCD) with a 600 × 582 array of 40 μm square pixels. When an X-ray photon is absorbed into the silicon of the detector it dissipates into a cloud of electron–hole pairs that can be tens of μm in diameter depending on the photon’s energy. The pixel size of the detector was chosen so that, in most cases, the charge cloud generated by the photon would be absorbed within a single pixel. CheMin’s CCD-224 imager is a custom e2v (Now Teledyne e2v, Chelmsford, UK) frame-transfer device. The front-illuminated design has an open gate structure on its surface to optimize detection of low-energy photons and is deep-depleted to maximize the absorption of higher energy photons (e.g., detection efficiency of 0.35 for CoKα). The CCD is actively cooled by a

Rycor™ tactical cryocooler to reduce background [16]. The cryocooler dissipates heat into *Curiosity's* Rover Avionic Mounting Platform (“RAMP”). The temperature of the RAMP varies depending on season and time of day from -5° to 20° C. As the cryocooler is only able to maintain a ΔT of -45° C between the RAMP and the CCD, CheMin is operated at night, when the temperature during analysis stays at $\sim -50^{\circ}$ C. Operating the CCD at this temperature lowers background noise to improve the signal-to-noise ratio of the detector.

The CCD is operated in single-photon counting mode, meaning that single frames of data are collected and read often enough so that, in the vast majority of cases, each pixel will contain either a charge equivalent to the energy of a single detected photon or background. When operated in this fashion, the detector records both the energy and the x, y pixel position of each photon. The energy of a single electron–hole pair generated in silicon is 3.65 eV; if a $\text{CoK}\alpha$ photon is absorbed into a single pixel in the array, on average $6930 \text{ eV} / 3.65 \text{ eV} = 1899$ electron–hole pairs will be generated, which sum to the energy of the $\text{CoK}\alpha$ photon. Some energy losses can occur, for example, due to the secondary fluorescence of Si X-rays from the detector itself, or charge splitting between adjacent pixels. Figure 7 shows a histogram of X-ray energy (displayed as raw digital numbers or “DN” from the CCD) from a synthetic ceramic standard containing most of the elements of geologic interest above $Z = 12$, obtained with the CheMin flight instrument during cryogenic vacuum testing on Earth. CheMin was initially designed to have a capability for both XRD and XRF analysis of received samples, however, its XRF analysis capability was descope for technical and cost reasons early in the flight instrument build.

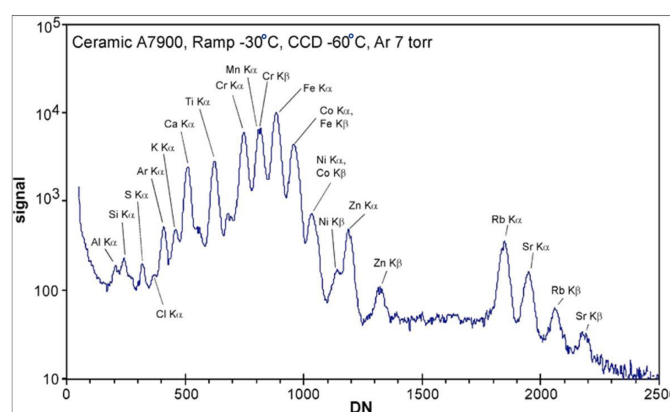


Figure 7. Energy-dispersive histogram (EDH) of the ceramic standard analyzed during Cryo-Vac testing of the CheMin instrument on Earth. RAMP (Rover Avionics Mounting Platform) held at -30° C and CCD at -60° C, and 7 torr of Argon was used to simulate the Mars atmosphere.

In a typical sample analysis lasting 10–30 h and occurring over 2–3 Mars nights, hundreds of ten-second integrations are collected and stored. Raw data consist of 600×582 arrays that store charge collected from individual CCD frames. The data are stored as DN (digital number energy bins) that are transformed to energy (in KeV) after downlink. Ideally, all raw frames would be transmitted to ground for processing, but the data volume is too large for this to be feasible. As a result, only a few frames of raw data are returned to monitor background, assess the health of the CCD, and to choose DN values suitable for background and high and low DN limits for energy-discriminated diffraction products. During the on-board processing of individual raw single frames, photons that fall within a window that brackets the energy of $\text{CoK}\alpha$ (6.93 keV) are summed into a 600×582 2D counting number array that constitutes an energy-selected $\text{CoK}\alpha$ Debye–Scherrer pattern of the sample. An energy histogram of all photons summed from the frames constitutes an X-ray fluorescence spectrum of the sample. An example of energy-selected diffraction and fluorescence data is shown in Figure 8. A minor frame is typically comprised of 180 10 s exposures. As many as 45 minor frames are summed to yield a high signal-to-noise 2D diffraction pattern for analysis. As a contingency measure, a diffraction product is

constructed that is comprised of individual frames summed into a 600×582 array as raw data without energy selection (called “film mode” because the CCD collects photons in the same fashion as X-ray-sensitive photographic film). A single real number array holds the summed images for each minor frame. Figure 9a shows a single minor frame of film mode data from Rocknest, the first sample analyzed on Mars. The degradation of the image is due to the detection of a flood of neutrons and cascades of secondary X-ray photons from the rover’s Radioisotope Thermal Generator (RTG) power source (which contains several kg of plutonium) and cosmic ray background. For comparison, Figure 9b shows CoK α energy-selected data from six summed minor frames of a modern regolith target Rocknest (RN, sol 0095). All downlinked higher-level data products are described in [2] and can be downloaded from the “Gale Crater Mineralogy and Geochemistry Sample Database” [17]. However, in all cases, energy-selected CoK α data are used in our published analyses.

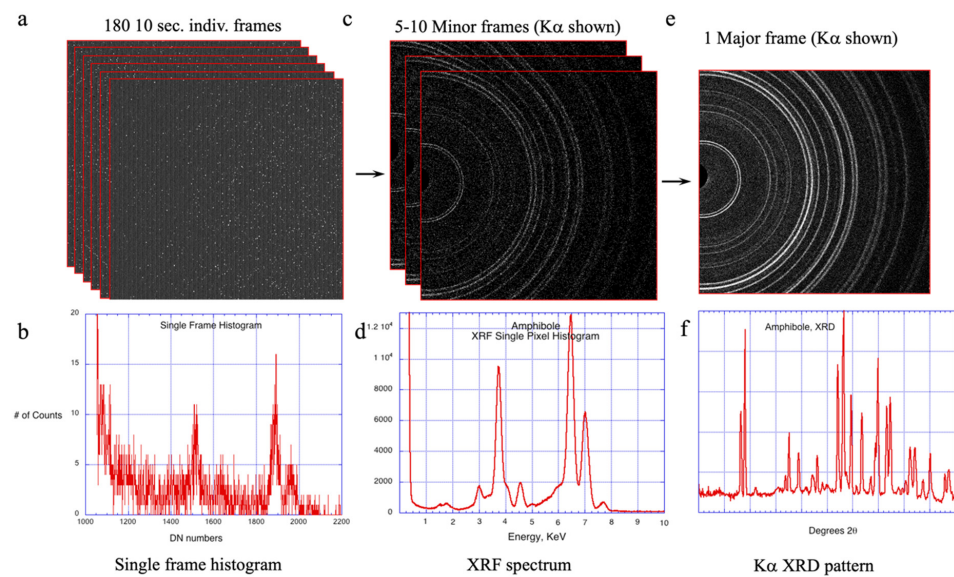


Figure 8. 2D diffractograms of the Gore Mountain amphibole standard (analyzed during CryoVac testing of the CheMin instrument on Earth). (a) Stack of 180 individual 10 s frames of data. (b) EDH from a single 10 s frame of data. (c) Stack of 10 minor frames of energy-selected CoK α data. (d) XRF spectrum from 10 minor frames of data. (e) Major frame of 10 summed minor frames of energy-selected CoK α data. (f) 1D diffractogram from (e).

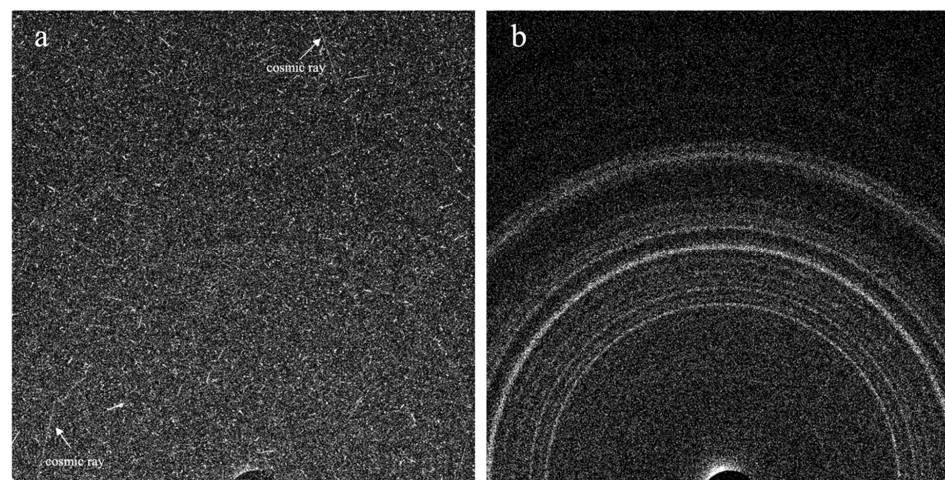


Figure 9. Comparison of film mode vs. energy-selected CoK α mode CheMin 2D data. (a) Minor frame (sum of 180 10 s images) of raw energy data. (b) Sum of 6 minor frames of energy-selected CoK α data.

2.3. CheMin 2 θ Calibration

The total X-ray beam path from the sample to the detector is 18.5 mm. As a result of this compact geometry, the largest error in 2 θ pattern measurement is introduced by the ± 50 μm machining tolerances of individual sample cells. Morrison et al. [18] describe a method to correct for these sample displacement errors using the refined lattice parameters of plagioclase feldspar, a mineral found in sufficient abundance in all but one sample analyzed on Mars to date. A compilation of the published lattice parameters of terrestrial plagioclase feldspars is found in the RRUFF database [19], and see also [18], their Appendix A. If one plots the relationship of the plagioclase γ vs. c parameters for terrestrial examples, the points lie on a linear regression line [18], their Figure 3. Using a sample–detector distance calculated from an analysis of one of CheMin’s standards as a starting point, refined lattice parameters for γ and c are determined. The sample–detector distance for each cell is then adjusted by increments until γ vs. c from the Martian plagioclase falls on the γ vs. c parameter regression line for terrestrial plagioclase.

2.4. Analysis of CheMin Diffraction Patterns

Data are downlinked from the spacecraft as 2D “minor frames.” Each minor frame is a 600×582 counting number array of CoK α photons, summed from 180 individual 10 s exposures of the CCD. A complete analysis typically includes the data from 15 to 45 minor frames of 30 min, each collected over two or more Martian sols. However, in some off-nominal analyses, for example when grain motion is poor due to clogging, the mineralogy of patterns containing as few as four minor frames has been successfully quantified, albeit with higher mineral detection limits (e.g., the Buckskin sample reported in [20]). All minor frames contain some off-ring blobs and spots due to cosmic rays, detector defects, etc. These are removed and replaced with local background values prior to the 2D to 1D conversion. Once downlinked, CheMin’s 2D Debye diffraction rings, corrected for arc length, are summed circumferentially around the central beam to yield a conventional 1D diffraction pattern using a modified version of GSE_ADA software v1.09 [21]. However, commercial software such as FilmScanTM (ICDD, Newtown Square, PA, USA) can be used as well.

All raw data from the CheMin instrument are downloadable from the “Gale Crater Mineralogy and Geochemistry Sample Database” [17], as well as 2D and 1D diffraction patterns, crystallographic information files (CIFs) files chosen for quantitative analyses and cell parameter refinement, our preferred analytical result, companion data from other instruments, and all papers published by the CheMin science team.

There are three components that commonly contribute to CheMin’s diffraction patterns: a crystalline component, a poorly crystalline clay mineral component, and an X-ray amorphous component. The treatment of these three components during quantitative analysis is described below.

2.4.1. Analysis of the Crystalline Component

In each pattern, a small contribution to the background is due to the Kapton or mylar cell windows, and this “empty cell” contribution is subtracted during the refinement process. An aluminized mylar film in the beam path between the sample and the detector is used to shield the CCD from sample-generated optical fluorescence. The crystalline Al on this “light shield” produces diffracted intensity at approximately 25.5° and 32° 2θ that must be subtracted from the pattern. A custom light shield CIF was constructed for this purpose, however, because the most intense light shield peak occurs at the position of the principal peak of cristobalite, a cristobalite CIF can also be used. If clay minerals are present, patterns obtained from clay mineral standards with CheMin-IV, a ground-based instrument with the same geometry as CheMin, are fitted to the pattern and subtracted. Finally, nearly all samples analyzed to date contain X-ray amorphous components, manifested as a broad scattering background having a maximum of between 26° and 31° 2θ , and a low angle rise extending from 4° to 14° 2θ . This scattering intensity is modeled and fitted to the pattern so that proper peak intensities and backgrounds can be retrieved

from the crystalline component. For the identification and refinement of the crystalline component, CIFs from the AMCSDB database (<http://rruff.geo.arizona.edu/AMS/amcsd.php>, accessed on 3 May 2024) are used, in addition to a small number of CIFs created from structure refinements of minerals hand-picked from Martian meteorites. The identities, amounts, and refined lattice parameters of crystalline phases present in the sample are determined through search-match and Rietveld refinement (e.g., [22,23]) using the Jade™ code (ICDD, Newtown Square, PA, USA). Immediately after initial data are downlinked, independent refinements are performed by four or five members of the CheMin team, and a synopsis of these results is provided to the MSL Science Team for planning purposes. Once an entire analysis (comprising two or more nights of data) has been downlinked, a sample displacement offset is calculated and applied to the pattern and a second round of Rietveld refinements is conducted. The reported mineral identifications, abundances, and mineral lattice parameters are a consensus result of these refinements. Compositions are calculated for those minerals having variable compositions and contents >~3 wt. % using regression equations of lattice parameter vs. composition from [24]. These minerals typically include plagioclase and alkali feldspars, Mg-Fe-Ca C2/c clinopyroxene, Mg-Fe-Ca P21/c clinopyroxene, Mg-Fe-Ca orthopyroxene, Mg-Fe olivine, magnetite and other spinel oxides, and alunite–jarosite. A compilation of CheMin’s mineralogical analyses to date, including quantitative mineralogy, refined lattice parameters for major minerals in each sample, and their associated elemental compositions is presented in Morrison et al. [25] In some cases, the Scherrer equation [26] is used to identify crystal sizes when the FWHM peak width of a particular mineral exceeds the instrument FWHM.

2.4.2. Analysis of Clay Mineral Components

In terrestrial laboratories, the identification of clay minerals with X-ray diffraction typically involves the use of oriented sample mounts and sample processing techniques such as humidity variation, sample heating, or treatment with ethylene glycol; none of these methods were implemented for the CheMin instrument on Mars. In the low relative humidity (RH) environment of the CheMin sample cell, expandable clay minerals lose their interlayer water, with the result that collapsed smectite cannot be discriminated from illite and other 2:1 clay minerals such as mixed layer illite–smectite (I/S) solely on the basis of the position of the (001) diffraction maximum (e.g., [27]). However, the breadth of the (001) diffraction peak and lack of correlation between clay mineral content (determined with CheMin) and bulk K content of the sample (determined with the APXS instrument) suggest that discrete illite (which contains K as its interlayer cation) or illite-rich I/S are not present [28].

The collapse of smectite interlayers to a d_{001} -spacing of approximately 10 Å induced by low RH conditions in CheMin permits identification of chlorite (d_{001} of about 14 Å) and mixed-layer chlorite–smectite (d_{001} between 10 and 14 Å). Indeed, the position of the 001-diffraction maximum of smectite in the Cumberland sample indicates partial intercalation by metal–hydroxyl groups (incipient chloritization), thought to indicate the presence of high pH fluids in these rocks [27,29]. The presence of other mixed-layer clays in Gale samples from the Glen Torridon region has been hypothesized based on a diffraction maximum at 9.2 Å. This peak is consistent with the presence of mixed-layer serpentine–talc-like mineral [30,31]. Kaolinite-group clay minerals have a distinctive diffraction peak at low 2θ that has not been observed in any sample to date.

For 2:1 clay minerals, the occupancy and cation species within the octahedral sheet (i.e., dioctahedral vs. trioctahedral) are used for clay mineral identification and have important implications for mineral paragenesis. In terrestrial laboratories, the 06 l band is used for this purpose, but this is beyond CheMin’s 2θ range. The 02 l band (22.5° to 23.1° 2θ CoK α ; 4.53 Å to 4.47 Å) is used for this purpose [29], albeit with occasional interferences from diffractions from other minerals. NEWMOD software [30] is used for detailed modeling of the (001) maximum of clay minerals (e.g., see [31,32]) and the BGMN software [33] is used for detailed modeling of the 02 l band in clay minerals (e.g., see [27,28]). Water release EGA data from SAM complement

CheMin data and can also be used to discriminate between the types of smectite clays present in a drill target based on the temperature of the water evolution (e.g., [34]).

The amount of clay mineral in a sample vs. other components is determined using the full-pattern fitting program FULLPAT [35,36]. Purified clay mineral standards, heated prior to analysis to collapse the interlayer to 10 Å, were analyzed in CheMin-IV. A combination of trioctahedral and dioctahedral smectite clays accounts for the majority of clay mineral components in the Martian samples at Gale.

2.4.3. Analysis of X-ray Amorphous Components

All CheMin samples analyzed to date on Mars contain an X-ray amorphous component. The proportion of the X-ray amorphous component relative to the crystalline and clay mineral components is determined by two complimentary methods.

They are determined by diffraction: the presence of X-ray amorphous components in XRD patterns can be inferred from the appearance of a low angle rise ($< \sim 10^\circ 2\theta$) and by a broad peak in the background spanning from approximately 15 to $45^\circ 2\theta$. Because amorphous peaks are broad and have limited distinguishing features, XRD patterns of amorphous materials are significantly less distinct than for crystalline phases and thus it is more difficult to determine accurate quantitative abundances. With full-pattern fitting of entire patterns, slight variations in shape and positions of the broad features can allow specific amorphous phases to be identified as possible candidates in the pattern of a multicomponent sample. FULLPAT uses a least squares minimization to optimize the fit between standard patterns and measured patterns. Quantitative analysis is facilitated by adding a known amount of a corundum (Al_2O_3) internal standard to both library standards and unknowns. All individual library patterns are normalized on an equal-corundum basis so that the corundum in each library standard is at the same intensity as the corundum in the observed pattern, thereby removing instrumental and sample-related effects. FULLPAT is similar to the traditional Reference Ratio Intensity (RIR) method [37] except that instead of using individual peaks, FULLPAT uses entire diffraction patterns. In laboratory application, because the amount of corundum added to standards and unknowns is identical (20%), each analysis is reduced to nothing more than scaling and matching of corundum-normalized library patterns to the patterns of those phases in the observed pattern and produces unconstrained analyses that should sum to $\sim 100\%$ [35]. Internal standards are not used in the CheMin instrument on Mars. However, since all standard phases are normalized to be equal on the basis of the intensity of their corundum internal standard, an 'external standard' or 'adiabatic' analysis can be conducted without addition of an internal standard to the unknown [38]. External-standard analyses are performed by scaling each library pattern to match the observed pattern, thereby yielding relative percentages for all phases, and then the relative percentages are normalized to sum to 100%.

A requirement for FULLPAT is that for each individual phase/material, including the amorphous materials, the XRD pattern has either been measured on a similar XRD instrument or calculated using the same instrument parameters as the samples being analyzed. X-ray amorphous standards (allophane, palagonite, hisingerite, synthetic basaltic composition glass, opal-A, amorphous MgSO_4 , etc.) spiked with a beryl or corundum standard were analyzed in the CheMin IV instrument to determine their RIR values [39,40].

The version of FULLPAT adapted for the MSL mission contains a standards library that has an extensive suite of crystalline minerals, X-ray amorphous and poorly ordered phases (e.g., rhyolitic glass, basaltic glass, palagonite, allophane, ferrihydrite, etc.), Kapton (X-ray window material), and linear backgrounds that can all be included in a regression. As all patterns are normalized to an equal intensity as if an internal standard had been added to the sample (e.g., RIR, [37]), amorphous patterns are simply intensity-normalized phases in the regression whose abundances will be determined alongside the crystalline minerals.

One limitation in the analysis of amorphous materials is that it is not known for certain what the amorphous components are on Mars. FULLPAT may contain library standards whose patterns appear to be similar in shape and features, but similarity in the chemical

composition and other properties is unknown. On Mars, due to power requirements, shorter analysis times are used than what would be typical on Earth. Consequently, a lower signal-to-noise ratio is observed in the pattern and it becomes increasingly difficult to distinguish the subtle differences between amorphous species.

The amorphous component(s) found in the Martian samples are almost certainly not of the same structure or composition as their lab-measured surrogates. For this reason, the relative amounts of the amorphous component(s) determined with FULLPAT are stated as $\pm 2s$ of the amount present.

They are determined by elemental composition: a second method utilizes the bulk elemental composition of the sample as determined by APXS, obtained from the “dump pile” of material collected for analysis (this is not the same aliquot of sample analyzed by CheMin, and could have subtle compositional differences). The composition of the crystalline component (as determined by CheMin using refined lattice parameter vs. composition equations in [24]), multiplied by a scalar value, is subtracted from the bulk composition determined by APXS. The scalar value is increased until one of the major oxides in the bulk composition is reduced to zero. These two methods produce the same result within the stated error limits.

Smith et al. [41] performed X-ray laboratory analyses of natural samples containing amorphous components using three different quantitation methods (Rietveld refinement, full-pattern fitting analysis, and mass balance calculations) and compared them to a commonly used quantitative XRD method using internal standards. Amorphous abundance and amorphous composition measurements were found to be comparable for all methods. Results from CheMin analog methods were comparable to quantitative XRD results using internal standards. These results suggest that the amorphous abundances and compositions determined with CheMin XRD data and APXS bulk compositional data are reasonably accurate, albeit with the caveat that the structures of the amorphous components (and therefore the scattering distribution of the broad amorphous maxima) are unknown.

Lattice parameters are not sensitive to the presence of minor or trace elements incorporated into the minerals; without a correction, these elements measured in the bulk sample would be assigned to the amorphous component. To correct for this, minor and trace elements were measured from mineral phases found in Martian meteorites and added to their respective mineral phases in the samples analyzed on Mars.

3. Major Discoveries (“CheMin’s Diary of Discovery”)

As of sol ~4100 (a Martian sol, or day, is ~40 min longer than an Earth day), 40 drilled samples of sedimentary rock and three scooped samples of soil have been analyzed over the course of *Curiosity’s* 30+ km transect. These samples document the mineralogy of over 800 vertical meters of flat-lying fluvial, lacustrine, and occasional aeolian sedimentary rocks that comprise the lower strata of Mt. Sharp and the surrounding plains (Figure 10). Table A1 lists the attributes of all samples analyzed to date, and Figure A1 shows images of the drill holes and scooped samples. Figure 11 traces *Curiosity’s* path across the Bradbury Rise and its ascent up lower Mt. Sharp. The clastic sedimentary rocks contain minerals of basaltic origin with evidence of post-depositional diagenesis, involving connate and possibly low-temperature hydrothermal fluids. The rocks in many cases preserve much of their primary mineralogy and depositional sedimentary structures, suggesting that they were never strongly heated or deeply buried. Using the composition of present-day aeolian regolith as a proxy for the composition of the deposited and lithified sediment, it appears that in many cases the diagenetic changes that occurred were isochemical and that the minerals present are authigenic. Exceptions include secondary nodules and crystal dendrites, calcium sulfate veining, silica enrichment of the amorphous component in Mt. Sharp sedimentary strata, and Si-rich alteration halos. A striking hematite-rich feature in lower Mt. Sharp called Vera Rubin ridge is interpreted to be lake sediment altered by post-depositional diagenesis, involving either acidic or high-salinity groundwater fluids with elevated sulfate content, or the dissolution of silicate minerals by dense silica-poor brines, as detailed in Section 3.7.1. A surprising and still poorly understood observation is that all

of the ~3.5 Ga sedimentary rocks analyzed to date contain 15–70 wt.% X-ray amorphous material. Two very distinct types of amorphous material are modeled in sample patterns: basaltic glass, opal-A, and amorphous MgSO₄ best fit the broad maximum at mid-range 2q, and palagonite/allophane/ferrhydrite best fit the low-2q rise in the patterns. Hypotheses as to the origin of this material are presented in Section 3.9. Overall, the >800-m section of sedimentary rock explored in lower Mt. Sharp documents a perennial shallow lake environment, grading upward into alternating lacustrine/fluuvial and aeolian environments. The measured mineralogy of the sedimentary rocks reflects the mineralogy of the sediment source areas modified by post-depositional diagenetic alteration occurring over hundreds of millions of years. Taken together, the sedimentology and mineralogy of the strata appear to document the drying out and oxidation of the Mars surface environment in Hesperian time (3.7–2.6 Ga).

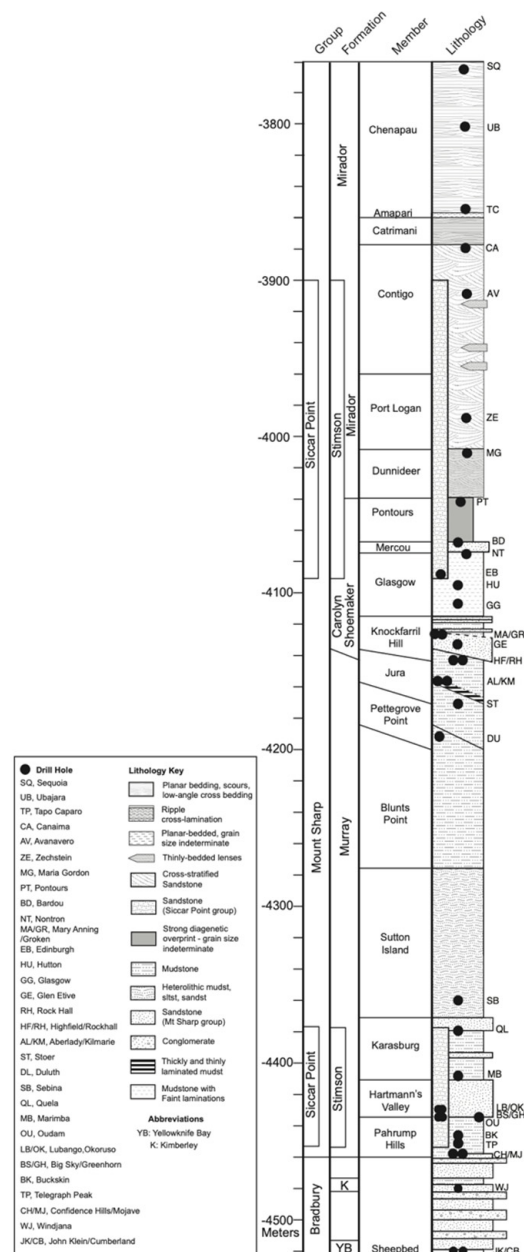


Figure 10. Stratigraphic column of units investigated by *Curiosity* from Yellowknife Bay to the Sulfate-Bearing Unit. Black dots denote drilled samples (Table A1 lists the attributes of all samples analyzed to date). Figure credit: the MSL sedimentology and stratigraphy working group.

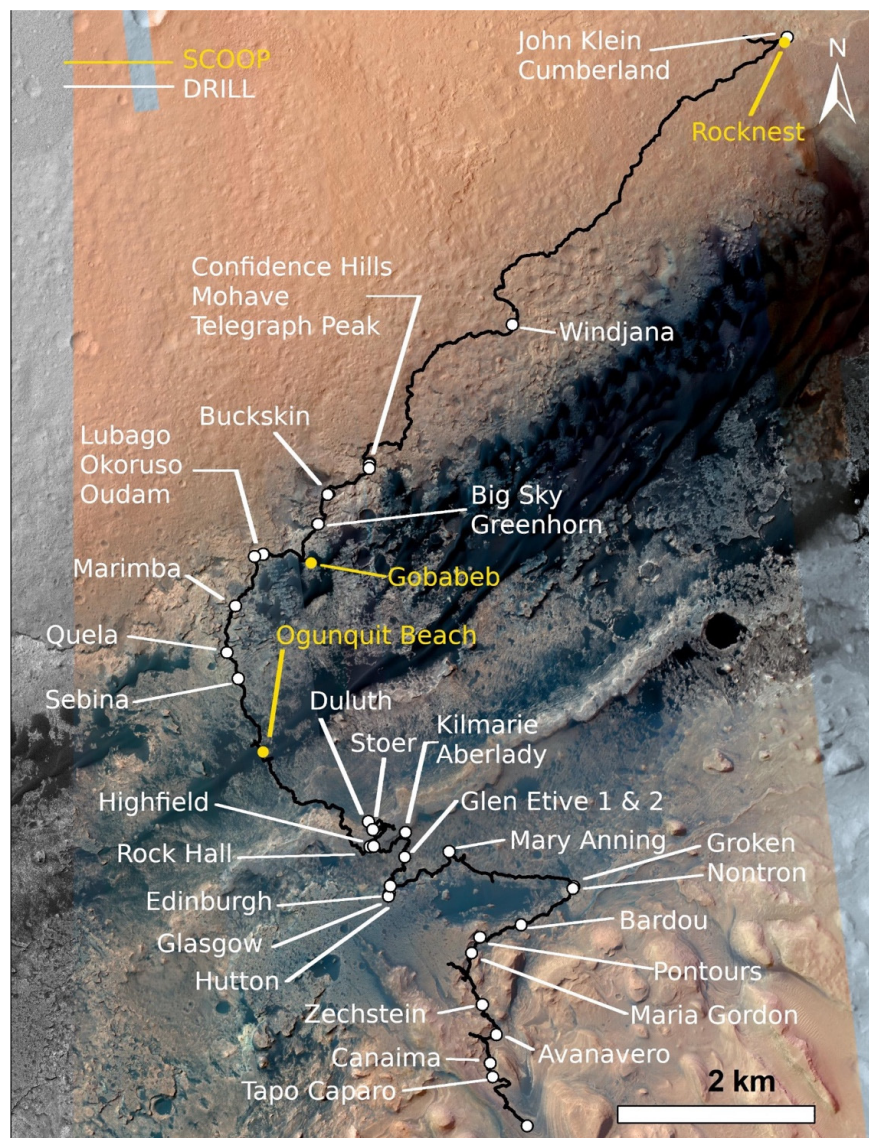


Figure 11. Plan view of *Curiosity*'s 12 year journey across Gale crater. Drilled rock samples are shown in white, scooped aeolian soil samples are shown in yellow.

3.1. The Mineralogy and Composition of the Mars' Global Soil

Curiosity investigated three unconsolidated aeolian features during its traverse of Gale crater. Rocknest (RN) is an inactive near-recent sand shadow investigated by *Curiosity* from sol 57 to sol 100 [42–44], Namib Dune (Gobabeb, GB) is part of the active Bagnold Dune Field that was investigated from sol 1164 to 1244 [45,46], and the Mount Desert Island ripple field (Ogunquit Beach, OG), also part of the Bagnold Dune Field, was investigated from sol 1602 to 1660 [47,48].

CheMin's analysis of the scooped and sieved <150 μm grain size component of Rocknest provided the first quantitative mineralogic analysis of Mars soil [42–44]. Rocknest is an accumulation of aeolian sediment deposited in the lee of a high relief cluster of rocks in the path of the wind (called a "sand shadow"). The surface is comprised of rounded 1 to 2 mm sand grains that form an armored surface ~2 to 3 mm in thickness. Beneath this armored surface, the bedform interior (analyzed by CheMin) consists of finer-grained material whose size distribution extends through the lower resolution limit of MAHLI images (~30 μm per pixel [9]). Rocknest is similar to coarse-grained granule ripples encountered at both Gusev crater and at Meridiani Planum by the MER *Spirit* and *Opportunity* rovers [49–52]. At Meridiani Planum, where a cratering record postdates the deposition

of a field of pristine granule ripples, crater counting yields an estimated bedform age of 50,000 to 200,000 years [53]. If one assumes that the coarse-grained bedform armor at Rocknest was deposited by the same high-wind event (perhaps during the most recent period of Mars obliquity [54,55]), the Rocknest sand shadow would have been inactive for that period of time as well. Figure 12 shows the first X-ray diffraction pattern returned from Mars, 100 years after the discovery of X-ray diffraction by Max von Laue [56].

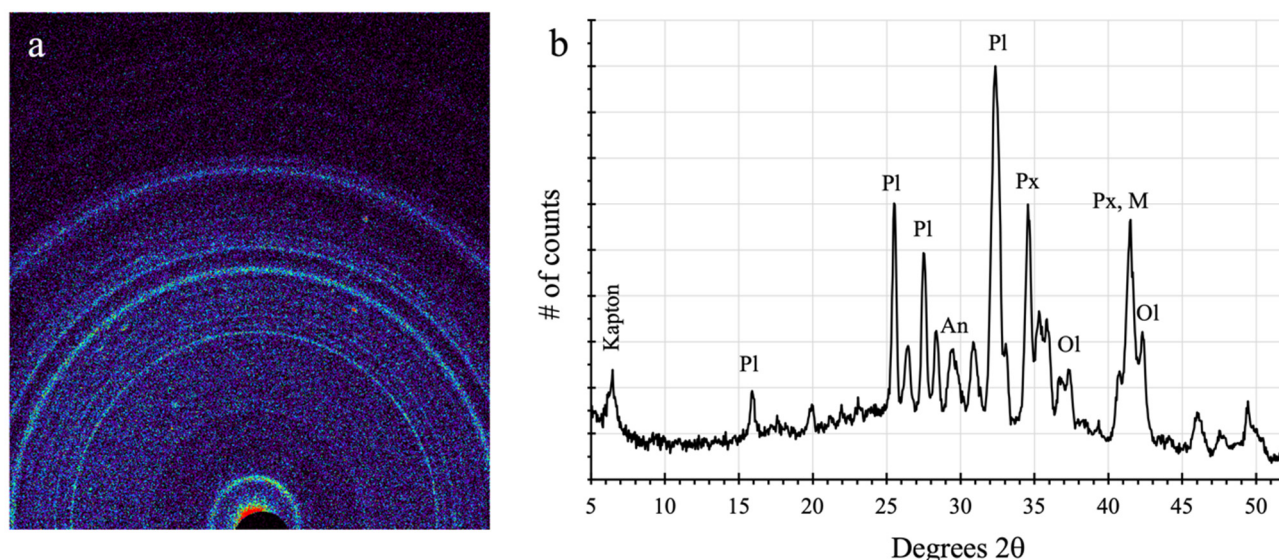


Figure 12. First X-ray diffraction pattern to be returned from Mars. (a) Colorized 2D pattern. (b) Obtained from (a), 1D pattern; most intense peaks of major minerals shown (Pl = plagioclase feldspar, An = anhydrite, Px = pyroxene, Ol = olivine, M = magnetite).

Table 1 lists the APXS compositions of aeolian materials from RN and GB (MSL) compared with average soils from Meridiani Planum and Gusev crater (MER). The striking similarity in composition between modern soil samples measured at various locations on Mars is compelling evidence that these materials represent a global soil average composition [42–44]. The mineralogy of soils analyzed by the MER rovers was determined from mid-IR spectral deconvolutions, normative geochemical calculations, and Mössbauer spectroscopy [57–59]. The mineralogy of RN, GB, and OG as determined by CheMin is chemically and mineralogically similar to that inferred for Martian basalts across the planet and broadly similar to estimates of the average Martian crust [59,60]. These basalts contain (or have normative chemical compositions consistent with) olivine, augite, pigeonite, and plagioclase feldspar. The mineral proportions of the crystalline components of RN, GB, and OG are virtually identical to those determined from normative calculations for the unaltered Adirondack class basalts from Gusev crater [57,59] (Table 2). The compositions of plagioclase, olivine, augite, and pigeonite from Rocknest and Gobabeb (determined from their refined lattice parameters [18,24,25]) shown in Table 3 are a significant revision of those shown in [42] and are the preferred values. The molar Mg/(Mg + Fe) ratios for olivine and pigeonite in both samples are similar: permissive evidence that they formed in the same environment. However, the augite is distinctly more magnesian and could not have formed in equilibrium with the pigeonite and olivine, suggesting that either the source basalts had a complex cooling history, or the pyroxenes came from different basalts [24,45,46]. It should be noted, however, that the refined unit cell parameters and calculated crystal chemistries of pyroxenes in samples with more than one pyroxene species present have significant errors associated with them due to the relatively low 2θ resolution of CheMin.

Table 1. APXS compositions of modern basaltic soils in Gale crater, Meridiani Planum, and Gusev crater, normalized to 100% totals ¹ (after [42]).

| | Gale ² | | Meridiani | Gusev |
|--------------------------------|-------------------|---------|----------------------|----------------------|
| | Rocknest | Gobabeb | Average ³ | Average ³ |
| SiO ₂ | 43.02 | 47.90 | 45.7 ± 1.3 | 46.1 ± 0.9 |
| TiO ₂ | 1.19 | 0.88 | 1.03 ± 0.12 | 0.88 ± 0.19 |
| Al ₂ O ₃ | 9.38 | 9.78 | 9.25 ± 0.50 | 10.19 ± 0.69 |
| FeO _T | 19.20 | 17.92 | 18.8 ± 1.2 | 16.3 ± 1.1 |
| MnO | 0.42 | 0.37 | 0.37 ± 0.02 | 0.32 ± 0.03 |
| MgO | 8.70 | 7.57 | 7.38 ± 0.29 | 8.67 ± 0.60 |
| CaO | 7.27 | 7.30 | 6.93 ± 0.32 | 6.3 ± 0.29 |
| Na ₂ O | 2.70 | 2.75 | 2.21 ± 0.18 | 3.01 ± 0.30 |
| K ₂ O | 0.49 | 0.49 | 0.48 ± 0.05 | 0.44 ± 0.07 |
| P ₂ O ₅ | 0.95 | 0.79 | 0.84 ± 0.06 | 0.91 ± 0.31 |
| Cr ₂ O ₃ | 0.49 | 0.39 | 0.41 ± 0.06 | 0.33 ± 0.07 |
| Cl | 0.69 | 0.50 | 0.65 ± 0.09 | 0.70 ± 0.16 |
| SO ₃ | 5.48 | 3.36 | 5.83 ± 1.04 | 5.78 ± 1.25 |
| Ni | 456 | 504 | 457 ± 97 | 476 ± 142 |
| Zn | 327 | 190 | 309 ± 87 | 270 ± 90 |
| Br | 34 | 37 | 100 ± 111 | 53 ± 46 |

¹ Oxides and Cl are reported in wt. % and normalized to 100%; Ni, Zn, and Br are reported as ppm. ² Values from [18]. ³ Values from [57].

Table 2. Adirondack, Rocknest, and Gobabeb mineral abundances (crystalline phases only) from normative APXS data and Rietveld refinement and FULLPAT analyses of CheMin XRD data ² (after [18,25,42]).

| Location | Gusev ¹ | | Gale ² | |
|------------------|--------------------|----------------------|----------------------|----------------------|
| | Adirondack | Rocknest | Rocknest | Gobabeb |
| Plagioclase | 39 | 40.7 (5) | 40.7 (5) | 36.5 (8) |
| Olivine | 20 | 20.5 (4) | 20.5 (4) | 25.8 (4) |
| Augite | 15 | 18.1 (13) | 18.1 (13) | 22.0 (4) |
| Pigeonite | 15 | 12.3 (12) | 12.3 (12) | 10.6 (4) |
| Magnetite | 6 | 2.8 (5) | 2.8 (5) | 2.1 (2) |
| Anhydrite | ---- | 1.4 (3) ³ | 1.4 (3) ³ | 1.3 (1) ³ |
| Hematite | ---- | 1.6 (1) ³ | 1.6 (1) ³ | 0.9 (1) ³ |
| Quartz | 0 | 1.3 (3) ³ | 1.3 (3) ³ | 0.8 (1) ³ |
| Ilmenite | 1 | ---- | ---- | 1.3 (5) ³ |
| Mg# ⁴ | ---- | 57(5) | 57(5) | 56 (6) |
| Ca# ⁵ | ---- | 50(4) | 50(4) | 63 (5) |

¹ Normative calculation from APXS data. ² Abundances in wt. %; uncertainties reported as 1s. ³ At or below detection limit. ⁴ Percent Mg in forsterite/fayalite. ⁵ Percent Ca in plagioclase feldspar.

Table 3. Mineral formulas and associated errors (1σ) for the major minerals present in the Rocknest and Gobabeb aeolian dunes (after [18,25]).

| Mineral | Rocknest | Gobabeb |
|-------------|---|--|
| Plagioclase | Ca _{0.49(4)} Na _{0.51(4)} Al _{1.49} Si _{2.51} O ₈ | Ca _{0.63(6)} Na _{0.37(6)} Al _{1.63} Si _{2.37} O ₈ |
| Olivine | Mg _{1.14(3)} Fe _{0.86(3)} SiO ₄ | Mg _{1.08(3)} Fe _{0.92(3)} SiO ₄ |
| Augite | Mg _{0.94(9)} Ca _{0.72(4)} Fe _{0.34(10)} Si ₂ O ₆ | Mg _{0.89(8)} Ca _{0.73(3)} Fe _{0.38(9)} Si ₂ O ₆ |
| Pigeonite | Mg _{0.97(8)} Fe _{1.03(9)} Si ₂ O ₆ | Mg _{0.95(12)} Fe _{0.99(17)} Ca _{0.06(8)} Si ₂ O ₆ |

The fraction of RN soil < 150 μm in particle size analyzed by CheMin contains ~80% crystalline material consistent with a basaltic heritage and ~20% X-ray amorphous material. The amorphous component of RN is iron-rich and silicon-poor, is the host of the volatiles (water, oxygen, sulfur dioxide, carbon dioxide, and chlorine) detected by SAM [61], and likely constitutes the fine-grained nanophase oxide component first described from basaltic soils analyzed by MERs [58].

3.2. Discovery and Characterization of an Ancient Habitable Environment on Mars

In its first drilled sample, acquired on sol 192, *Curiosity* documented a section of fluvio-lacustrine strata at Yellowknife Bay (YKB), an embayment on the floor of Gale crater, approximately 500 m east of the Bradbury landing site (elevation, -4520 m) [62,63]. X-ray diffraction data from CheMin show that two powdered mudstone samples (John Klein (JK) and Cumberland (CB)) drilled from the Sheepbed member of this formation contain up to 20 wt% clay minerals. Figure 13a shows the bit of the percussion drill that is used to produce the powder, and Figure 13b shows the test drill hole (upper left) and the final drill hole (lower right) of JK (the diameter of the drill hole is 16 mm). Figure 13c shows the sieved powder held in the sample cup. A trioctahedral smectite, characterized as a ferrian saponite [27,29,64], is the only clay mineral phase detected in these samples (Figure 14). The mudstones are part of a section of the fluvio-lacustrine YKB formation, derived from erosion of rocks along the Gale crater rim, as confirmed by a bulk K-Ar age of 4.21 ± 0.35 Ga [65]. The stratigraphic relationships between the YKB formation and either the Peace Vallis fan or the strata of lower Mt. Sharp are uncertain. However, strata of the YKB formation, including the clay-mineral-bearing Sheepbed member, post-date the Noachian–Hesperian boundary (~ 3.7 Ga) and are younger than the majority of clay minerals documented on Mars from orbit [29,66,67].

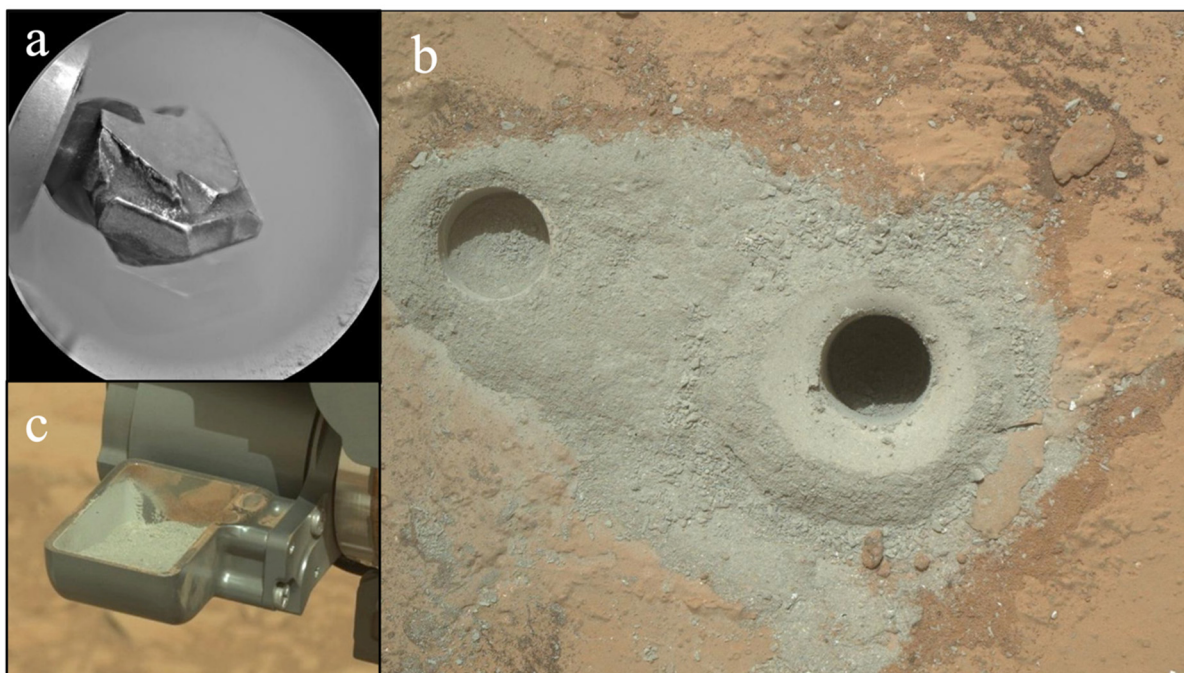


Figure 13. (a). Percussion drill bit used to drill and collect samples (16 mm dia). Powdered material is retained in the drill stem and transferred to the SA/SPaH system for sieving. (b) Image of shallow (1 cm deep) test drill hole (left) and the sampled drill hole (6.5 cm deep) from John Klein. (c) John Klein drill sample in the scoop reservoir before sieving to $<150 \mu\text{m}$ (note red residue powder in the scoop which is contamination from the previous sample (Rocknest)). The delivered samples typically contain $\sim 3\%$ contamination from the previously drilled sample [29].

The clay minerals at YKB are interpreted to have formed in situ and indicate that paleoenvironmental conditions within the fluvio-lacustrine system were potentially habitable for life [29,67]. The relatively low abundance of olivine (note: olivine is considered to be a contaminant from the previously drilled sample (RN) since it was not seen in CB, drilled 1 m away from JK) and enriched level of magnetite in the Sheepbed mudstone, when compared with regional basalt compositions derived from orbital data and directly determined from the Rocknest sand shadow, suggest that clay minerals and magnetite

formed in situ via aqueous alteration of olivine. Mass-balance calculations are permissive of such a reaction [27]. Early diagenetic fabrics (e.g., evidence of soft-sediment deformation, raised ridges in the sediment likely caused by volume expansion during clay mineral formation, hollow sedimentary concretions, etc.) indicate that clay mineral formation occurred prior to lithification [67]. Thermodynamic modeling [27] suggests that the production of authigenic magnetite and Fe-saponite at surficial temperatures requires a moderate supply of oxidants, allowing circum-neutral pH. The sluggish kinetics of olivine alteration at low temperatures imply the presence of fluids for thousands to hundreds of thousands of years.

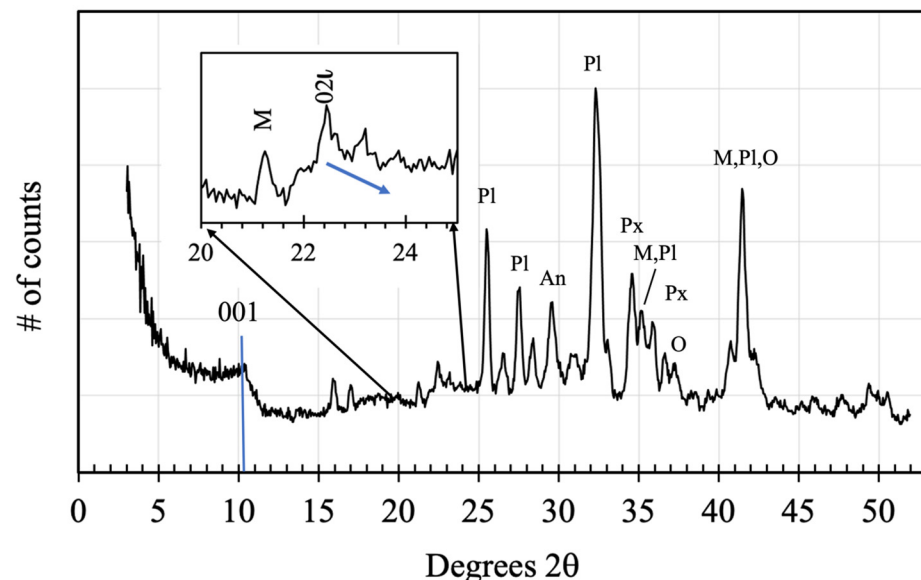


Figure 14. Diffraction pattern of John Klein, showing the position of the (001) reflection of smectite. Inset: portion of the pattern that contains the (02l) diffraction band of smectite. The maximum at 22.5° 2θ indicates that the clay mineral is trioctahedral. Blue arrow denotes the turbostratic nature of the 02l band, extending beyond the band maximum. Phase assignments labeled for major peaks (Pl = plagioclase feldspar, An = anhydrite, Px = pyroxene, M = magnetite, Ol = olivine) (redrawn from [27,29]).

The mineral assemblage at JK (and CB), as well as the physical sedimentology of the Yellowknife Bay formation were found sufficient by the MSL team to identify a habitable environment in ~ 3.7 Ga lakebed sediments in Gale crater, the criterion for MSL mission success [67]. Other habitable environments have been discovered and characterized during *Curiosity's* traverse through lower Mt. Sharp, both in the depositional environment (as in Yellowknife Bay), and in the shallow subsurface diagenetic environment. Indeed, the unexpected abundance and diversity of clay minerals in sedimentary rocks in Gale crater and the apparent longevity of this lacustrine sedimentary system indicate that near-surface aqueous alteration (and habitability) continued into the early Hesperian (~ 3.5 Ga) on Mars. Examples have also been found of post-depositional diagenetic alteration that would have destroyed evidence of a habitable environment had it existed. The conclusion is that mineralogy, contextualized with sedimentological observations, is quite capable of evaluating habitability in ancient rocks and elucidating post-depositional diagenetic changes that would preserve or destroy such evidence.

3.3. Evidence for a Diverse Basalt Mineralogy on Mars

Curiosity arrived at the Windjana drill site in the Bradbury group on sol 0623. Windjana, (WJ, elevation -4481 m), the fourth sample analyzed by CheMin, is the most potassic alkali-rich rock on Mars to be analyzed for its mineralogy by XRD. The source lithologies for WJ sediments represent a complex igneous province which includes (from their mineralogies) potassic trachyte, plagioclase-rich basalt (i.e., tholeiitic), and mafic basalt (i.e.,

shergottitic) [68]. This result implies that the northern rim of Gale crater, the source of these sediments, exposes an igneous complex that is at least as diverse as those found in similar-age terranes on Earth.

Curiosity crossed the landing ellipse boundary and began to climb Mt. Sharp on sol 0753. This ascent demarks the boundary between Bradbury Group rocks of the crater floor and the rocks of the Mt. Sharp Group (Figure 10).

3.4. Clay Mineral Diversity in the Sedimentary Strata of Gale Crater

CheMin analyses within Gale crater have documented changes in the amounts and species of environmentally sensitive minerals including pyroxenes, sulfates, clay minerals, and Fe-oxides as a function of stratigraphic position [28,69]. There is also an observed increase in the chemical index of alteration (extent of alteration of mafic detritus) derived from geochemical analysis in the upper part of the Murray Fm. [70]. Coupled with the observed sedimentological changes (e.g., depositional and early diagenetic features that indicate a shallowing of the lake and episodic lake desiccation [71,72]), these mineralogical changes document the drying out and oxidation of the local Gale crater environment. Because planet-wide orbital IR observations show similar sequences of mineralogical change, this is thought to be representative of the drying out and oxidation of the planet-wide Martian environment [28].

In lower Mt. Sharp, clay minerals were found in virtually all analyzed samples. For samples in which clay minerals were not detected within the Mt. Sharp Group rocks, evidence of post-depositional diagenetic alteration is sufficient to explain their absence. For all but two clay mineral detections (in which the 02 l band is either weak or obstructed by diffraction peaks from other minerals), the clay minerals can be identified as trioctahedral smectites, dioctahedral smectites, or mixtures of both. Rare exceptions include the sample Oudam (OU, sol 1363, −4435 m), which exhibited a peak at 9.6 Å, and the samples Kilmorie (KM, sol 2384, elevation −4155 m) and Groken (GR, sol 2912, elevation −4130 m), which exhibited a peak at 9.22 Å (in the case of KM and GR, a robust 10 Å smectite clay peak is present as well). Bristow et al. [28] characterized the 9.6 Å basal spacing clay mineral in OU as ferripyrophyllite, likely exogenous material transported into the crater as sedimentary detritus from older bedrock. However, analyses of samples drilled higher in the section at Vera Rubin Ridge identified clay minerals having a 9.6 Å basal spacing in mineral assemblages that would support in situ diagenetic formation [73]. The 9.22 Å peak observed in the KM and GR samples is assigned to a mixed layer of serpentine/talc [31] or minnesotaite/greenalite [32]. Bristow et al. [28,31] concluded that these clay minerals were likely exogenous material, transported into the crater as sedimentary detritus from older bedrock, whereas [32] postulated that the mixed-layer clay formed via groundwater–lake water mixing.

The clay mineral changes observed going up-section from the Yellowknife Bay Fm. of the Bradbury Group into the Murray Fm. of the Mt. Sharp Group include a transition from trioctahedral to dioctahedral clay minerals. Figure 15 shows diffraction patterns of samples analyzed from JK (elevation −4520 m), Marimba (MB, elevation −4400 m), and Glen Etive 2 (GE, elevation −4120 m), representative of a 400 m thick section of flat-lying sedimentary strata, along with measured patterns for clay mineral standards SAz-1 (dioctahedral) and SapCa-1 (trioctahedral) (note: the MSL drill was not available between elevations −4380 m and −4220 m; as a result, no CheMin data were recorded from this interval). The position of the 02 l band shifts from 22.5° to 23.1° 2 θ CoK α (4.53 Å to 4.47 Å), indicating a shift in the proportion of trioctahedral to dioctahedral smectite. The formation of dioctahedral smectite clays from basaltic precursors or from preexisting trioctahedral smectite clays requires greater elemental mobility and more oxidizing conditions than those of the trioctahedral smectites seen in Yellowknife Bay [28]. In samples like Glen Etive (from the Glen Torridon region), which contain dioctahedral smectites exclusively, the position of the 02 l band and derived unit cell lengths of smectite crystals along the b axis indicate that approximately half of the octahedral cations are Fe⁺³, with Al⁺³ filling

the remaining sites [28]. Similar Fe⁺³-rich dioctahedral smectites are inferred to be mixed (albeit in varying proportions) with Mg-rich trioctahedral smectites in lower strata, based on the modeling of XRD patterns, SAM-EGA analyses of the same samples, and regional orbital IR observations [28]. These authors argue that the observed mineralogical changes are early diagenetic, perhaps occurring in the shallow subsurface prior to lithification. Other mineralogical changes include the removal of some of the more reactive minerals in the original basaltic sediment (i.e., pyroxenes and olivine) and a change in the iron oxide mineralogy from magnetite (Fe₂⁺³Fe⁺²O₄) to hematite (Fe₂⁺³O₃).

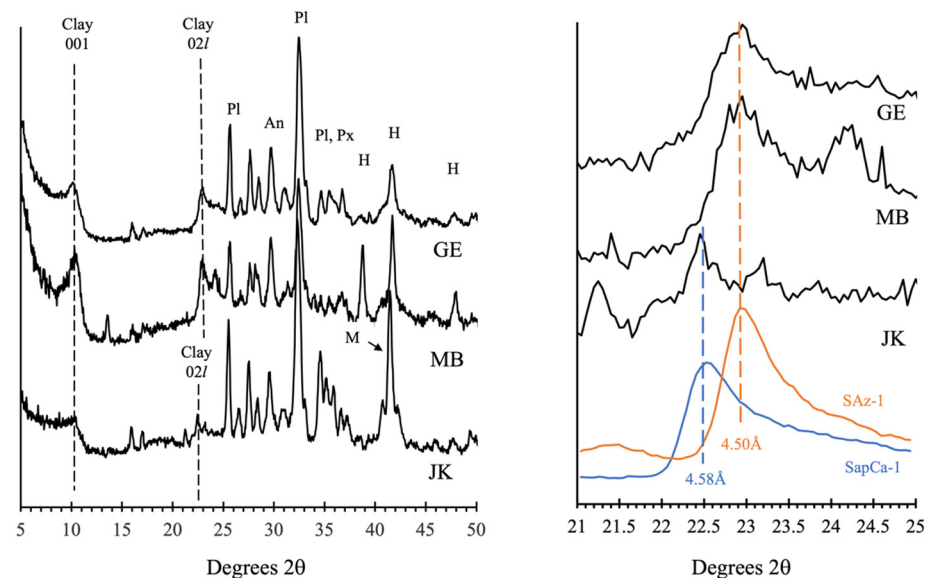


Figure 15. Diffraction patterns of John Klein, Marimba, and Glen Etive 2, showing transition from trioctahedral smectite to dioctahedral smectite. (a) Overall diffraction patterns showing clay mineral (001) reflection and 02l diffraction band. Major mineral peaks labeled (Pl = plagioclase feldspar, An = anhydrite, Px = pyroxene, M = magnetite, H = hematite). (b) The 21° to 25° 2θ region of the pattern, showing transition from trioctahedral to dioctahedral occupancy. Clay mineral standards SAz-1 (dioctahedral) and SapCa-1 (trioctahedral) shown for comparison.

3.5. Depositional and Post-Depositional Features in the Lower Murray Formation

Curiosity reached Mt. Sharp on sol 0753. The lower Murray formation at the base of Mt. Sharp is comprised of finely laminated mudstone with near-horizontal laminae, deposited in a subaqueous lacustrine environment [74]. Other depositional environments in this interval include sandstones interpreted as distal deltaic facies and fluvial facies discharging into the lake [75]. The lower Murray formation is time equivalent to and interfingers with coarser-grained strata of the Bradbury group [76]. Primary depositional textures are preserved, such as fine-scale laminations in the mudstone facies. However, there is also evidence of diagenetic features in the form of crystal molds, secondary crystallization, and calcium sulfate veins. The sediments could not have been deeply buried or heated, as much of the original mineralogy persists and depositional sedimentary features are preserved. In the Pahrump Hills—Marais Pass region, CheMin documented the loss of mafic igneous phases and clay minerals and the introduction of secondary minerals such as jarosite, suggesting the action of weakly acidic fluids [75]. Figure 16 shows diffraction patterns obtained from the drill samples Confidence Hills (CH, sol 0765, elevation −4460 m), Mojave 2 (MJ, sol 0885, elevation 4459 m), Telegraph Peak (TP, sol 0923, elevation −4454 m), and Buckskin (BK, sol 1062, elevation −4447 m). Table 4 (from [75]) lists the mineralogical compositions of the four samples. Hematite is seen in abundance for the first time on the mission (and its detection marked *Curiosity*'s arrival at Mt. Sharp), magnetite is present in all samples (and in increased abundance in the TP sample), and pyroxenes are seen to decrease in abundance going up section. Phyllosilicates are present in small amounts in

CH and MJ but absent in TP and BK. Relative to the Bradbury formation rocks, the lower Murray formation rocks exhibit an overall enrichment in SiO₂. Bulk SiO₂ abundance (from APXS), the SiO₂ abundance of the crystalline component (from CheMin), and the SiO₂ abundance of the amorphous component (bulk composition—crystalline composition) all increase going up-section.

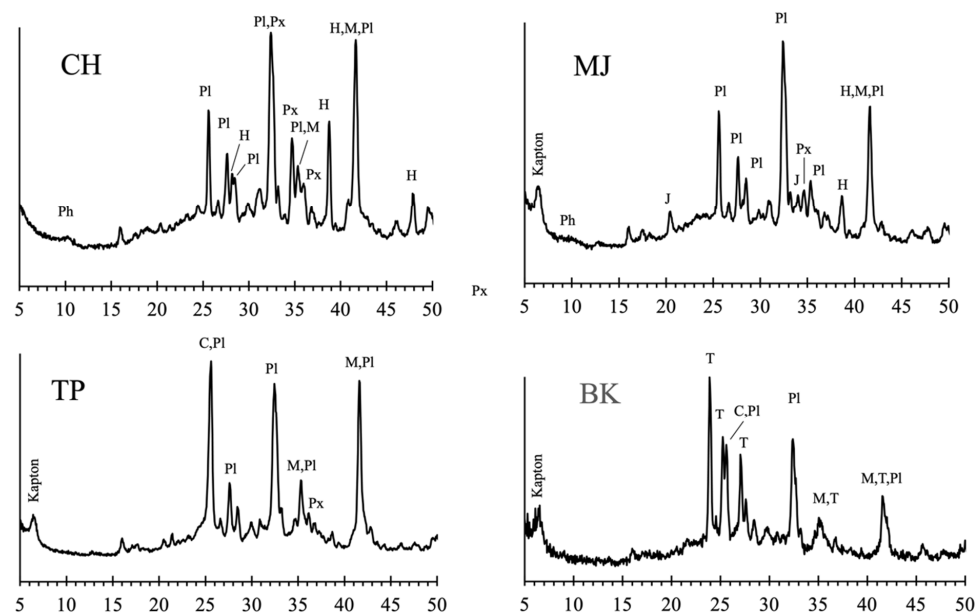


Figure 16. CheMin 1D X-ray diffraction patterns of drill samples Cumberland Hills (CH), Mojave (MJ), Telegraph Peak (TP), and Buckskin (BK) from the lower Murray formation. Major peaks are labelled (C = cristobalite, H = hematite, J = jarosite, M = magnetite, Ph = phyllosilicate, Pl = plagioclase, Px = pyroxene, T = tridymite).

Table 4. Mineral and amorphous abundances of samples in the lower Murray formation measured by CheMin, 2s errors are denoted in parentheses (after [75]).

| Mineral | Confidence Hills | Mojave 2 | Telegraph Peak | Buckskin ¹ |
|---|------------------------|-----------------|------------------------|-----------------------|
| Plagioclase | 20.4 (2.3) | 23.5 (1.6) | 27.1 (2.8) | 17.1 (1.2) |
| Sanidine | 5.0 (0.7) | -- | 5.2 (2.2) | 3.4 (0.7) |
| Forsterite | 1.2 (0.7) | 0.2 (0.8) | 1.1 (1.2) | -- |
| Augite | 6.4 (2.2) | 2.2 (1.1) | -- | -- |
| Pigeonite | 5.3 (1.7) | 4.6 (0.7) | 4.2 (1.0) | -- |
| Orthopyroxene | 2.1 (3.1) | -- | 3.4 (2.6) | -- |
| Magnetite | 3.0 (0.7) | 3.0 (0.6) | 8.2 (0.9) | 2.8 (0.3) |
| Hematite | 6.8 (1.5) | 3.0 (0.6) | 1.1 (0.5) | -- |
| Quartz | 0.7 (0.5) | 0.8 (0.3) | 0.9 (0.4) | -- |
| Cristobalite | -- | -- | 7.3 (1.7) | 2.4 (0.3) |
| Tridymite | -- | -- | -- | 13.6 (0.8) |
| (H ₃ O ⁺ , K ⁺ , Na ⁺) | 1.1 (0.7) | 3.1 (1.6) | 1.5 (1.8) | -- |
| Jarosite | -- | -- | -- | 0.7 (0.2) |
| Anhydrite | -- | -- | -- | -- |
| Fluorapatite | 1.3 (1.5) | 1.8 (1.0) | 1.9 (0.5) | -- |
| Phyllosilicate ² | 7.6 | 4.7 | -- | -- |
| Amorphous | 39.2 ± 15 ² | 53 ³ | 38.1 ± 15 ² | 60 ³ |

¹ Values from [22]. ² Values from FULLPAT analyses alone. ³ Values from amorphous component calculations using CheMin and APXS results.

Rampe et al. [75] hypothesized that sediments at the base of the Pahrump Hills were deposited in a lake with near-pH-neutral waters. Initially deposited sediments contained magnetite. The refined unit cell of the magnetite (~8.35–8.36 Å) is decreased relative to

stoichiometric magnetite (8.396 Å; e.g., [77]). The decreased unit cell length can represent vacancies in the structure, for example $3\text{Fe}^{+2} = 2\text{Fe}^{+3} + [\]$ (e.g., [18], their Figure 9). Cation-deficient magnetite can occur by leaching of Fe^{+2} from the structure with acidic solutions (pH 2–2.5; [78]). This cation deficiency supports the Rampe et al. [75] proposed model of diagenesis in acidic groundwater.

Multiple circulations of acidic groundwaters resulted in the dissolution/transformation of original minerals and the precipitation of new minerals (oxidation of magnetite to hematite, precipitation of jarosite/natrojarosite $(\text{K,Na})\text{Fe}_3(\text{SO}_4)_2(\text{OH})_6$ and gypsum). Pore fluids were hypothesized to be mildly acidic and oxidic [75] and mobilized minor elements such as Zn and Ni (identified by APXS) were precipitated as sulfate salts (Mg-Ni sulfate concretions) identified by ChemCam. An alternative view is expressed in [79], in which the sequence of observed mineralogical changes is viewed as primary rather than diagenetic, resulting from redox stratification in the lake.

Radiometric K/Ar dating of the jarosite from MJ from the SAM instrument indicates that it was formed at 2.57 ± 0.39 Ga [80], thus documenting a long history of aqueous interactions in Gale crater sediments extending from the deposition of the Yellowknife Bay formation to the deposition and diagenesis of the Murray formation (a period of nearly 1 Gy).

At the top of the Pahrump Hills, crystalline silica phases were identified in abundance for the first time. TP and BK each contain significant amounts of the SiO_2 polymorph cristobalite, and the BK sample collected at Marais Pass (surprisingly) contains the SiO_2 polymorph tridymite [20]. On Earth, tridymite is found as a high-temperature, low-pressure, vapor-deposited mineral associated with silicic volcanism (typical in continental crust settings [81]). It was hypothesized in [20] that this material could have been washed into the lake as exogenous detrital volcanic material from an unknown silicic source (see also [82,83], which propose instead an in situ hydrothermal, fumarolic mechanism for formation). The mineralogy of the Buckskin sample is consistent with terrestrial fumarolic deposits, and the temperature could have been within tridymite's thermodynamic stability field (>870 °C) driven by a yet undetected subsurface volcanic heat source. However, there is no sedimentological evidence in the localized strata indicating extremes of heat and primary bedding is in many cases preserved.

It is clear that a post-depositional diagenetic event occurred which involved silica-rich fluids (probably associated with the alteration halos observed in Stimson Fm. aeolian sandstone described in Section 3.6). The petrogenesis of tridymite therefore remains an open question and may be associated with this post-depositional event in a paragenetic mode not seen on Earth.

3.6. Si-rich Alteration Halos in the Stimson Formation Aeolian Sandstone

In the Marais Pass area at the top of the Pahrump Hills, *Curiosity* first encountered and drilled the Stimson formation, an aeolian sandstone overlying the Murray formation. Where it has not been removed by erosion, the Stimson sandstone is observed as a cap rock that truncates bedding in the Murray formation, thus defining a disconformity between the two units [84–86]. Watkins et al. [84] noted that the discovery of this disconformity reveals what constitutes the rock cycle on Mars, a planet in which plate tectonics is not an active geologic agent: older lacustrine sediments (Murray Fm.) are deposited, lithified, and eroded. Younger aeolian sediments (Stimson Fm.) are deposited over the eroded Murray Fm. and are then themselves lithified. The entire sequence is then eroded and exhumed by aeolian abrasion over an extended interval of time up to the present. The lithified aeolian sandstones of the Stimson are seen to extend laterally for kilometers, and, vertically through nearly 400 m of flat-lying Murray formation strata up to the Greenhugh pediment, an erosional remnant of the Stimson [86].

Light-toned, fracture-associated alteration halos crosscut both the Murray formation and the overlying Stimson formation in the vicinity of Marais Pass [87], e.g., Figure 17. ChemMin performed mineralogical analyses of the parent rock and the fracture-associated alteration halos at Big Sky/Greenhorn (BS, sol 1122 (parent Stimson)/GH, sol 1140 (altered

Stimson), elevation –4460 m) and Okoruso/Lubango (OK, sol 1335 (parent Stimson)/LB, sol 1325 (altered Stimson), elevation –4450 m). Figure 18 shows the BS and GH diffraction patterns as well as a diffraction pattern from Edinburgh (EB, sol 2715, elevation –4060 (parent Stimson)), a sample drilled from the Greenheugh pediment, ~400 m higher in the section than BS. Dotted lines denote the differences between what is likely the most pristine Stimson (EB), slightly altered Stimson (BS), and highly altered Stimson (GH). Major mineralogical changes include the overall loss of pyroxene in altered Stimson, the presence of olivine in EB (likely an original mineral of the parent sandstone) and its absence in BS and GH, and the presence of a major amount of anhydrite in the altered Stimson (GH). Table 5 lists the mineral abundances for each. The mineralogical changes in the fracture-associated halos require multiple aqueous alteration stages with fluid chemistries encompassing a wide range of pH. Significant mineralogical changes include the dissolution of original basaltic mineral components (plagioclase, pyroxenes) resulting in the passive enrichment of silica, but mass-balance calculations from APXS data suggest that additional silica and sulfate were incorporated as well [87]. Amorphous silica enrichment and calcium sulfate veining are pervasive features of the Murray formation, the former without disruption of original sedimentary features and the latter commonly crosscutting them. Calcium sulfate veining occurred both before deposition of the Stimson formation [86] and after the Stimson formation was deposited and lithified [87]. Silica enrichment appears to be the latest diagenetic change observed by *Curiosity* in Mt. Sharp rocks, occurring after the lithification of the Stimson formation. The silica-rich fluids must have been introduced at some depth, since the alteration halos seen in the Stimson sandstone at Marais Pass result from exposure of the host Stimson to hydrothermal fluids emanating from veins under confining pressure. Yen et al. [83] present evidence that these halos are hydrothermal in origin, associated with the same fluid system that formed the tridymite in BK. Yen et al. [83] propose that the high-silica crystalline and amorphous components found in the Buckskin drill sample Murray Fm. formed through similar processes involving in situ hydrothermal silicification.

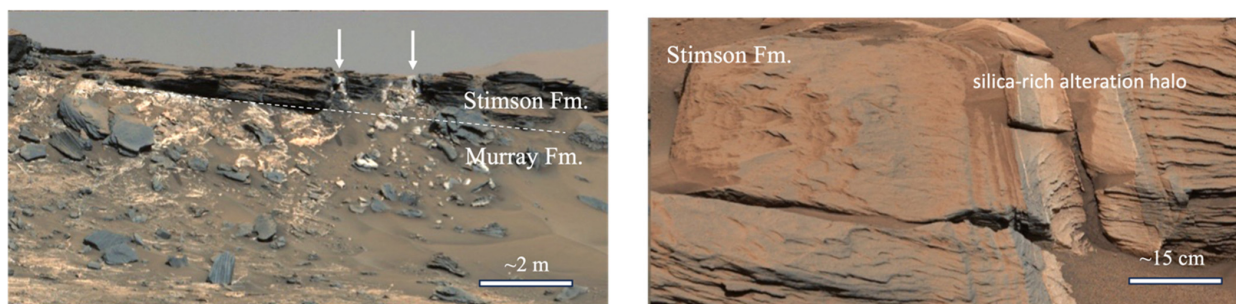


Figure 17. (a) MastCam image of the disconformal boundary between Murray Fm. mudstone (lower slope-forming unit) and Stimson Fm. aeolian sandstone (upper cliff-forming unit). A white dashed line marks the approximate position of the disconformity. Light-toned material in the figure is of two types: anhydrite veins (light reddish-brown) that are terminated and crosscut by the disconformity, and Si-rich alteration halos (white, marked with arrows) that extend through the boundary (albeit with differing manifestations in the two units). (b) Silica-rich alteration halo in the Stimson sandstone. CheMin mineralogical analyses of the alteration halo and the parent sandstone provide information as to the nature of the fluids that produced the alteration.

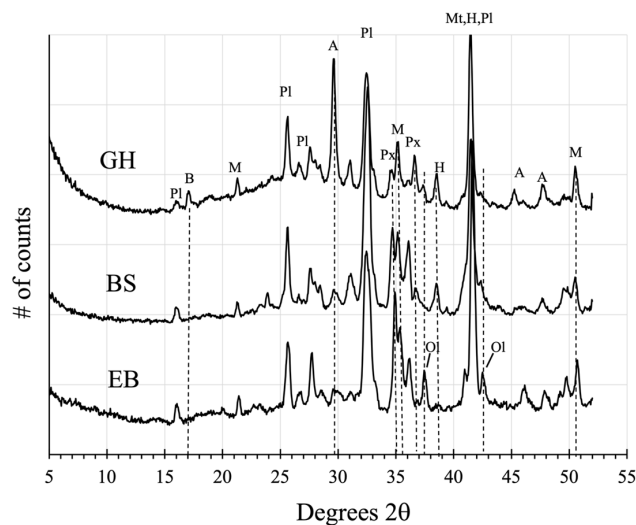


Figure 18. Diffraction patterns of Stimson Fm. sandstone. Edinburgh (EB), likely the least altered Stimson sandstone; Big Sky (BS), slightly altered Stimson; and Greenhorn (GH), pervasively altered Stimson, in the light-toned alteration halo. Dotted lines identify major mineralogical changes to the Stimson due to hydrothermal or post-depositional diagenetic alteration (Pl = plagioclase feldspar, B = bassanite, M = magnetite, A = anhydrite, Px = pyroxene, H = hematite, Ol = olivine).

Table 5. Mineralogical composition of Edinburgh (least altered Stimson sandstone), Big Sky (slightly altered Stimson sandstone), and Greenhorn (highly altered Stimson sandstone within the light-toned alteration halos, e.g., see Figure 17). The large amorphous component in Greenhorn includes a passive enrichment of silica from dissolution of pyroxene and the addition of silica from the invading fluid.

| | Edinburgh | Big Sky | Greenhorn |
|------------------------|-----------|------------------|-----------|
| Plagioclase | 39.6 | 45.7 | 42.1 |
| Tot. Px | 27.6 | 30.2 | 12.3 |
| Sanidine | 4.6 | 1.7 | -- |
| Magnetite | 14.0 | 12.6 | 17.3 |
| Hematite | 0.5 | 3.6 | 6.0 |
| Quartz | | 1.6 | 2.2 |
| Forsterite | 11.5 | -- | -- |
| Fluorapatite | 0.02 | 1.4 | -- |
| Anhydrite | | 1.5 | 16.1 |
| Tridymite ¹ | -- | 1.8 ¹ | -- |
| Basanite | | -- | 4.0 |
| Total xtal. | 100% | 100% | 100% |
| % Amorphous | 20% | 20% | 65% |

¹ Contamination from previous sample (Buckskin).

3.7. Vera Rubin Ridge and the Glen Torridon Region

The most striking features observed in orbital IR images of Gale crater prior to the arrival of MSL *Curiosity* (and, indeed, a principal reason for choosing Gale as *Curiosity's* landing site) are the juxtaposed hematite-rich and phyllosilicate-rich layers on lower Mt. Sharp that transition upslope into a sulfate-rich horizon (Figures 2 and 19). These minerals either require liquid water for their formation or contain water in their structures. Because similar mineral sequences have been observed planet-wide in overfilled and exhumed craters like Gale [4], it was hypothesized that the local conditions that existed in Gale crater during their formation may be representative of planet-wide environmental events. It is noteworthy that CheMin has identified clay minerals and Fe-oxides along *Curiosity's* entire transect up to this point in Gale crater, not just in regions where these minerals were detected from orbit. Orbital IR spectra can be obscured by a few microns of dust, highlighting the

need for in situ observations by mineralogy instruments such as CheMin. However, the Fe-oxides in Vera Rubin ridge (the hematite-rich exposure) and the phyllosilicates in Glen Torridon (the phyllosilicate-rich exposure) are present in the highest concentrations measured by CheMin in Gale crater.

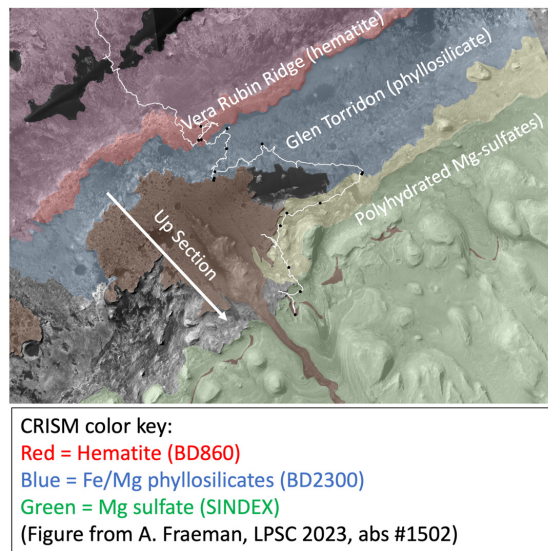


Figure 19. CRISM (Compact Reconnaissance Imaging Spectrometer for Mars) image of the Vera Rubin Ridge–Glen Torridon region of Mt. Sharp.

3.7.1. Vera Rubin Ridge

Curiosity arrived at Vera Rubin ridge (VRR), the erosion resistant, hematite-rich feature identified from orbit, and drilled the Stoer sample (ST, sol 2136, elevation −4170 m) at a location near the strongest hematite spectral signature seen from orbit, followed by two other VRR samples, Highfield (HF, sol 2223, elevation −4147 m) and Rock Hall (RH, sol 2261, elevation of −4144 m). A fourth sample, Duluth (DU, sol 2057, elevation −4192 m) was drilled immediately below VRR in a region that lacked the strong orbital hematite spectral signal for comparison. The drill tailings from the four samples are markedly dissimilar in appearance (Figure 20) due to mineralogical differences, compositional differences, and the presence of nanophase hematite. Mineralogical compositions of the four samples are shown in Table 6.

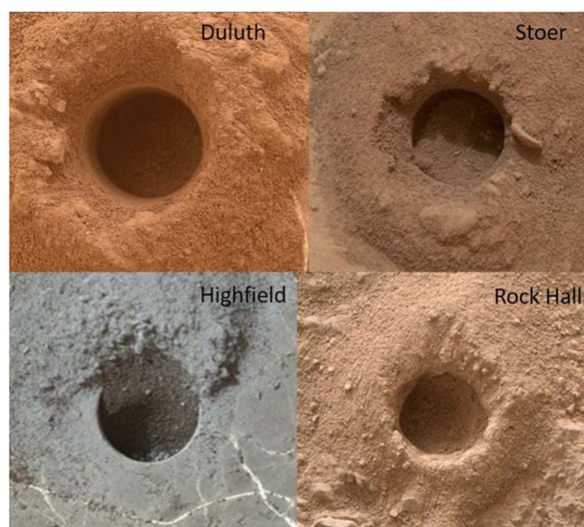


Figure 20. Drill holes for Duluth (DU), Stoer (ST), Highfield (HF), and Rock Hall (RH). ST, HF, and RH were drilled from Vera Rubin ridge, a hematite-rich ridge-forming feature seen from orbit, and DU, which lacks the orbital hematite signature, was drilled immediately below the ridge for comparison.

Table 6. Mineralogical composition of Murray Fm. mudstone (Duluth) and diagenetically altered Murray Fm. mudstone in the Vera Rubin ridge (Stoer, Highfield, and Rock Hall)¹.

| Phase | Drilled Sample | | | |
|----------------|-----------------|-----------------|-----------------|---------------------|
| | Duluth | Stoer | Highfield | Rock Hall |
| Plagioclase | 27.1 (6) | 23.2 (10) | 19.9 (9) | 20.2 (22) |
| K-spar | 3.2 (4) | 1.6 (13) | 1.6 (5) | --- |
| Pyroxene | 4.5 (11) | 3.3 (9) | 4.2 (15) | 9.1 (10) |
| Hematite | 6.1 (10) | 14.7 (8) | 8.5 (5) | 2.9 (2) |
| Magnetite | 0.7 (4) | 0.3 (3) | 0.5 (5) | --- |
| Akaganeite | --- | 1.2 (7) | --- | 6.0 (5) |
| Jarosite | --- | 1.0 (3) | --- | 2.3 (5) |
| Anhydrite | 1.7 (4) | 3.1 (3) | 3.5 (5) | 11.2 (4) |
| Bassanite | 3.5 (3) | 0.5 (2) | 1.1 (3) | --- |
| Gypsum | 0.1 (1) | 2.4 (8) | 2.2 (5) | --- |
| Quartz | 1.0 (4) | 0.7 (4) | 0.5 (3) | --- |
| Fluorapatite | --- | --- | --- | 1.3 (4) |
| Phyllosilicate | 15 (4) | 10 (3) | 5 (1) | 13 (3) |
| Opal-CT | --- | --- | 4 (1) | --- |
| Amorphous | 37 ² | 38 ² | 49 ² | 38 (8) ³ |

¹ 1 s errors reported in parentheses, applied to the last decimal place. ² Minimum amorphous abundance based on mass balance calculations. ³ Amorphous abundance based on FULLPAT analysis.

The continuity of primary sedimentary features (e.g., bed forms, fine-scale laminations, etc.) above, below, and within VRR demonstrates that the ridge is part of the Murray Fm. mudstone; diagenetic features that define the ridge are seen to crosscut Murray Fm. depositional features. The differences in FeO_x crystallinity, the composition of the X-ray amorphous component, and the overall mineralogy of VRR samples (ST, HF, RH) vs. “typical” Murray Fm. mudstone directly below the ridge (DU) can be used to constrain the nature of the diagenetic event(s). For example, while hematite is known to form in a variety of thermal and chemical environments on Earth and is present in all four samples, its origin can be constrained based on crystallography. The FWHM resolution of CheMin is ~0.35° 2 θ , with the result that the Scherrer equation [26] can be used to determine crystallite sizes smaller than about 40 nm [75]. The FWHM of the hematite (110), (104), and (113) peaks in the VRR samples match the 2 θ resolution of the instrument so that the crystallite size must be larger than this (and the gray color of the HF sample suggests that there are localized regions of coarse-grained hematite). However, the FWHM of hematite (104) in DU is 0.66° 2 θ , yielding a crystallite size of ~18 nm [73]. Szczerba et al. [88] measured the FWHM of hematite diffraction maxima in 20 drilled samples analyzed with CheMin. The smallest crystallite sizes (~3 nm) were found in the drilled samples highest in the section (above VRR), while the largest (~40 nm) were in the lower sections (and in VRR, whose crystallites were too large to be measured by line broadening). Figure 21 shows the 2 θ region of the DU and HF patterns that contains hematite (104), hematite (110), and hematite (113) maxima. The smaller hematite crystallite sizes in DU and other Murray Fm. samples (exclusive of VRR) imply a nanophase precursor (e.g., ferrihydrite or goethite), typically formed at low temperatures. The coarser hematite crystallite sizes in VRR may have been a result of warmer temperatures involving Ostwald ripening and/or the aggregation of smaller hematite particles in saline solutions.

The compositions of the X-ray amorphous components of these samples provide additional evidence. The X-ray amorphous component of DU contains an especially high concentration of FeO_t, suggesting the presence of an X-ray amorphous Fe phase such as ferrihydrite. In the VRR samples, Fe in the X-ray amorphous component is more highly correlated with sulfate and elevated SiO₂ concentrations. Indeed, in the ST sample, all Fe is taken up in the crystalline component.

Taken together, mineralogical observations within VRR suggest localized post-lithification diagenesis of the Murray sediments involving acidic or high-salinity groundwater fluids with

elevated sulfate content [73]. Alternative hypotheses have been presented, for example, the interaction of lake waters with sub-surface ground water in the mixing zone prior to lithification [32], or the dissolution of silicate minerals by dense silica-poor brines [31].

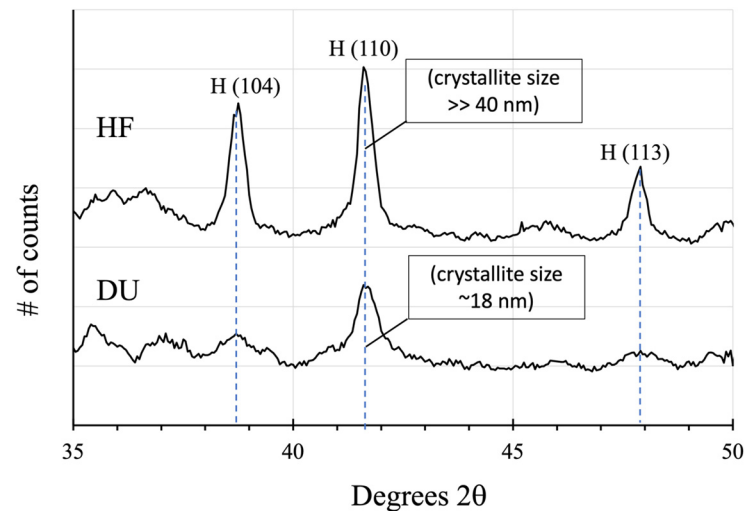


Figure 21. Comparison of hematite (104), (110), and (113) diffraction maxima (marked as “H”) between DU (Murray Fm. mudstone below VRR) and HF (altered Murray Fm. mudstone within VRR).

3.7.2. Glen Torridon Region

Globally, a wide variety of clay minerals has been identified from orbit in ancient rocks (e.g., [89,90]). In some occurrences, clay minerals are associated with what are interpreted to be paleosol sequences (ancient soil horizons), for example, at Mawrth Vallis (e.g., [91]), or as detrital or authigenic clays in the distal facies of deltaic sediments and lacustrine deposits [92–94]. Gale crater was chosen as MSL’s landing site, in part based on orbital IR detections of clay minerals in the Glen Torridon region that were interpreted to be strata-bound deposits of sedimentary origin. CheMin’s in situ analyses of Gale crater sediments have in fact shown that clay minerals are ubiquitous throughout at least 400 m of sedimentary rock from Yellowknife Bay in the Bradbury Fm. to Glen Torridon in the Murray Fm. and Carolyn Shoemaker Fm., all occurring in lacustrine and fluvial mudstones/sandstones. These observations inform and provide ground truth for earlier studies based on orbital infrared imagery and reflectance spectra that proposed multiple hypotheses for clay mineral paragenesis [66,95].

Curiosity analyzed eight different drill samples from the Glen Torridon region, both in the Murray Fm. and the overlying and conformal Carolyn Shoemaker Fm. [95] The Carolyn Shoemaker Fm., which first appeared in the GT region, is principally a sandstone, interpreted as a higher energy fluvial or near-shore environment relative to the Murray Fm. mudstone. The primary igneous mineralogy, type and amount of clay minerals present, amount and composition of the X-ray amorphous component, etc., are not strikingly different from other samples of the Murray mudstone, with the exception of phases that appear to be the result of late-stage post-depositional events, for example, hematite, jarosite, and the silica-rich amorphous component found in the Pahrump Hills—Marias Pass region.

Figure 22a shows four representative diffraction patterns of samples from Glen Torridon: Aberlady (AB, sol 2370, elevation −4160 m), Kilmarie (KM, sol 2384, elevation −4160 m), Mary Anning 3 (MA3, sol 2888, elevation −4130 m), and Groken (GR, sol 2912, elevation −4130 m). Figure 22b shows the 2θ region of the (001) clay mineral maximum in these patterns. In addition to the 10\AA (001) maximum due to collapsed smectite, an additional sharp maximum at 9.22\AA is seen in the patterns. The CheMin team searched the entire American Mineralogist Crystal Structure Database [96] but did not find a conclusive match, based on both diffraction data and elemental composition. Two hypotheses have been proposed: Bristow et al. [31] hypothesized a mixed-layer serpentine/talc based on

extensive modeling (e.g., [31] Appendix A) and considered it to be sedimentary detritus transported in from the erosion of older bedrock. Thorpe et al. [32] argued that this phase is a mixed-layer clay mineral (greenalite–minnesotaite, G-M) formed in situ, a result of the mixing of lake waters with subsurface fluids. Given the low concentration of this phase in Glen Torridon rocks (2.8 wt % in KM), the resolution of these two models will have to rest on sedimentological interpretations, perhaps augmented by future observations. Figure 22c shows the 02l region of these patterns, demonstrating that the predominant clay mineral present in Glen Torridon is fully dioctahedral Fe⁺³-rich smectite.

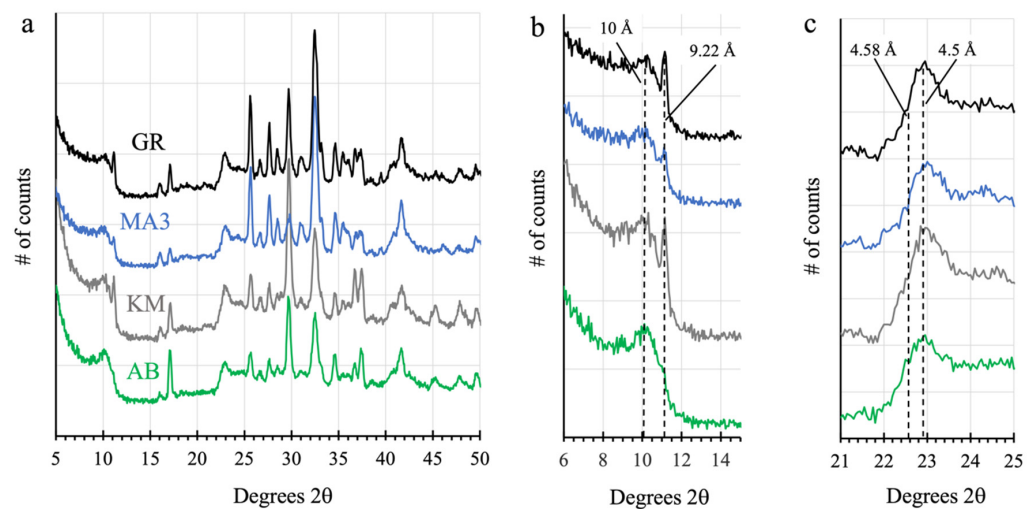


Figure 22. Diffraction patterns of four of the eight samples drilled from the Glen Torridon region of Gale crater. (a) Overall patterns of Aberlady (AB), Kilmalie (KM), Mary Anning 3 (MA3), and Groken (GK). (b) Low 2θ region showing the (001) maxima of clay minerals identified in Glen Torridon. All samples have the 10 Å (001) maximum typical of a collapsed smectite clay. KM, MA3, and GR also exhibit a sharp peak at 9.2 Å (the origin of which is a matter of debate; see discussion in the text). (c) The 2θ region of the 02l diffraction band of smectite clay minerals. All clay minerals are dioctahedral.

3.7.3. Brine-Driven Destruction of Clay Minerals in Vera Rubin Ridge

As described in Section 3.7.1, sedimentological observations during *Curiosity's* transect through the VRR and GT regions demonstrate that VRR is diagenetically altered Murray Fm. mudstone. Orbital imagery indicates that the Murray Fm. and Carolyn Shoemaker Fm. are conformably overlain by a ~400 m thick Sulfate-Bearing Unit (SBU) characterized as mono- and poly-hydrated magnesium sulfates (e.g., [5,97]). Magnesium sulfates are highly soluble and the supernatant brines resulting from Mg sulfate deposition would have been dense and silica-poor. Bristow et al. [31] propose a diagenetic mechanism for the local mobilization and recrystallization of iron from clay minerals in VRR, effected by the influx of dense, oxidizing silica-poor brines descending from the overlying Sulfate-Bearing Unit. These descending brines would cause local dissolution of clay minerals and other silicates in VRR, leaving Fe oxides and oxyhydroxides in their place. It follows that this diagenetic event must have occurred prior to lithification of the Murray Fm. Sediments, since there does not appear to be an unconformity between the Murray/Carolyn Shoemaker Fm. units and the overlying SBU. This mechanism could also explain calcium sulfate veining and secondary crystallization in the lower Murray Fm. below the VRR.

Bristow et al. [31] suggest that top-down diagenesis of clay minerals by dense, silica-poor brines, while rare on Earth, could be widespread on Mars. Orbital observations have shown that sulfate deposits similar to those seen in Gale crater were distributed planet-wide at a time when Mars was experiencing a shrinking hydrological budget and desiccation of the surface environment [89].

3.8. Mineralogical Characterization of the Sulfate-Bearing Unit

One of the principal goals of the MSL mission is to investigate the transition from the phyllosilicate-rich strata of the Glen Torridon region to the overlying sulfate-rich strata of the Sulfate-Bearing Unit (SBU) identified from orbital IR imagery [5], updated by [97]. This transition has been observed planet-wide in similar-aged terrains and was hypothesized by Bibring et al. [89] to evidence a change in climate from an early, relatively warm and wet Mars to a present-day cold and dry Mars. The juxtaposition of clay mineral, sulfate mineral, and oxide mineral strata in sedimentary sequences on a global scale was seen to correlate with a notional understanding of the geological history of the planet (“Phyllosian,” loosely correlated with the Noachian, 4.5–3.6 Ga; “Theikian,” loosely correlated with the Hesperian, 3.6–2.6 Ga, and “Siderikian,” loosely correlated with the Amazonian, 2.6 Ga—present [4,89]).

3.8.1. The Clay Mineral—Sulfate Mineral Transition Region

The MSL science team studied the sedimentology and geochemistry/mineralogy of rocks in the clay mineral—sulfate mineral transition region between Glen Torridon and the overlying Sulfate-Bearing Unit (SBU) from sols 3052 to 3572. *Curiosity* collected six drill samples in the transition region: Nontron (NT, sol 3056 elevation −4073.5 m), Bardou (BD, sol 3113 elevation −4066.5 m), Pontours (PT, sol 3171 elevation −4041.2 m), Maria Gordon (MG, sol 3232 elevation −4016.1 m), Zechstein (ZE, sol 3229 elevation −3992.0 m), and Avanavero (AV, sol 3517 elevation −3910.0 m). CheMin documented a decrease in clay minerals (indeed, all samples above PT lacked phyllosilicate), and goethite was detected for the first time in NT and increased in concentration from NT to AV. These mineralogical changes are proposed to be the result of a change from fluvial/lacustrine conditions to dry, aeolian conditions [98].

3.8.2. The Sulfate-Bearing Unit

Curiosity is now investigating sulfate-bearing mudstones and sandstones of the SBU. The hydrated magnesium sulfate mineral starkeyite (the four-hydrate of MgSO_4) was first identified in the drill sample Canaima (CA, sol 3614 elevation −3879 m) from an aeolian sandstone (Figure 23). Table 7 lists the eight known crystalline Mg-sulfate hydrate minerals, in addition to amorphous MgSO_4 (Am- MgSO_4). The overall mineralogical composition of CA is shown in Table 8. While the measured amount of starkeyite is low (2.3 wt.% of the total), the sample contains 62% X-ray amorphous material, with the result that starkeyite comprises 8.2% of the crystalline phases present. In the second and third analyses (2 and 12 sols, respectively, after the first analysis), starkeyite is below CheMin’s detection limit (<~0.3 wt %). For the duration of the analysis of CA, the temperature inside the rover body (and inside CheMin) varied from ~6–30° C, resulting in a relative humidity (RH) <<0.1% [99]. It is known from experimental studies that many hydrated Mg sulfates lose their waters of hydration, and some revert to an amorphous state under these conditions [100–105]. Gypsum ($\text{CaSO}_4 \cdot 2\text{H}_2\text{O}$) is also seen to decrease with a concomitant increase in bassanite ($\text{CaSO}_4 \cdot 0.5\text{H}_2\text{O}$). This has been observed in previous samples that contain gypsum and is described in [106,107]. Rhyolitic glass and Am- MgSO_4 were found to best fit the broad mid-range maximum in the pattern, but basaltic glass could also have been present, since it has a scattering distribution similar to Am- MgSO_4 . Disordered silicates (palagonite, allophane, and ferrihydrite) were used to fit the low 2θ (<10°) rise in the pattern. Chipera et al. [99] supported this diffraction-based result using mass balance calculations [41] from full-pattern fitting analysis of CheMin mineralogical data using FULLPAT [35,36] (method fully described in [99] Appendix A), bulk compositional data measured by APXS [11,108], and water content from ChemCam [109], i.e., see Table 9. Elevated MgO and SO_3 in the amorphous component strongly suggest that Am- MgSO_4 is present, with a calculated maximum abundance of ~28 wt%. The first night’s analysis of the CA sample occurred after half of a diurnal temperature cycle, and it is likely that

the starkeyite abundance was in fact higher, some having reacted to Am-MgSO₄ inside the rover before the first analysis was conducted [99].

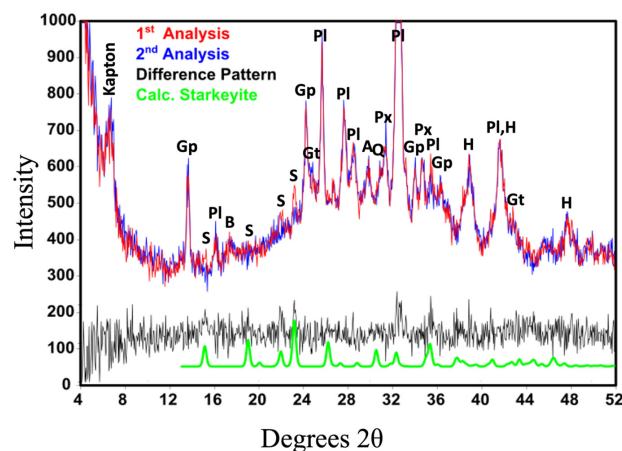


Figure 23. Diffraction pattern from the first night of analysis of Canaima, in the Sulfate-Bearing Unit. Low angle peak labeled Kapton is due to the cell window material. Gp = gypsum, S = starkeyite, Pl = plagioclase feldspar, B = bassanite, A = anhydrite, Px = pyroxene, H = hematite. Broad scattering peak between 15° and 45° 2 θ and low angle rise below 10° 2 θ are due to X-ray amorphous material which accounts for 62% of the sample (redrawn from [99]).

Table 7. Known MgSO₄ hydrate minerals and their formulae.

| Mineral | Formula |
|-----------------------------|--|
| Kieserite | MgSO ₄ ·H ₂ O |
| Sanderite | MgSO ₄ ·2H ₂ O |
| Starkeyite | MgSO ₄ ·4H ₂ O |
| Cranswickite | MgSO ₄ ·4H ₂ O |
| Pentahydrate | MgSO ₄ ·5H ₂ O |
| Hexahydrate | MgSO ₄ ·6H ₂ O |
| Epsomite | MgSO ₄ ·7H ₂ O |
| Meridianiite | MgSO ₄ ·11H ₂ O |
| Amorphous MgSO ₄ | MgSO ₄ ·nH ₂ O (n varies from ~1 to 2) |

Table 8. Mineralogical composition of Canaima. Amorphous abundances obtained using full-pattern fitting [35], data from [99].

| Phase | 1st Night | 3rd Night | 13th Night |
|--|------------|------------|------------|
| Starkeyite | 2.3 ± 0.3 | 0.1 ± 0.2 | --- |
| Andesine | 16.9 ± 0.6 | 15.5 ± 0.6 | 18.0 ± 0.5 |
| Gypsum | 4.0 ± 0.2 | 4.1 ± 0.2 | 1.5 ± 0.2 |
| Bassanite | 0.4 ± 0.3 | 0.8 ± 0.4 | 1.76 ± 0.3 |
| Anhydrite | 0.6 ± 0.3 | 1.0 ± 0.4 | 0.9 ± 0.5 |
| Hematite | 4.7 ± 0.4 | 4.7 ± 0.6 | 4.8 ± 0.5 |
| Goethite | 2.2 ± 0.6 | 2.2 ± 0.7 | 2.2 ± 0.6 |
| Quartz | 0.5 ± 0.2 | 0.5 ± 0.3 | 0.5 ± 0.2 |
| Sanidine | 3.2 ± 0.4 | 2.7 ± 0.6 | 3.4 ± 0.4 |
| Pyroxene | 3.2 ± 1.1 | 3.4 ± 0.8 | 3.7 ± 1.1 |
| Amorphous MgSO ₄ ·nH ₂ O | 19.4 ± 3.5 | 20.9 ± 3.5 | 20.0 ± 3.5 |
| Other Amorphous | 29.5 ± 7.4 | 28.5 ± 7.1 | 28.7 ± 7.2 |
| Palagonite-Like Material | 13.0 ± 3.2 | 13.0 ± 3.2 | 14.3 ± 3.6 |
| Total | 100.0 | 100.0 | 100.0 |

Table 9. Oxide wt% composition of Canaima (bulk, crystalline component, and amorphous component) from [99].

| Oxide | Chemical Analysis (Wt%) ^{1,4} | Crystalline Component (Wt%) ^{2,4} | Amorphous Component (Wt %) ^{3,4} |
|--------------------------------|--|--|---|
| SiO ₂ | 29.35 ± 0.37 | 14.1 ± 5.9 | 15.2 ± 5.7 |
| TiO ₂ | 0.77 ± 0.03 | --- | 0.77 ± 0.03 |
| Al ₂ O ₃ | 5.67 ± 0.16 | 5.3 ± 2.2 | 0.4 ± 2.1 |
| Cr ₂ O ₃ | 0.25 ± 0.01 | --- | 0.25 ± 0.01 |
| FeO _(T) | 15.5 ± 0.17 | --- | 8.7 ± 2.6 |
| FeO | --- | 0.4 ± 0.4 | --- |
| Fe ₂ O ₃ | --- | 6.7 ± 2.9 | --- |
| MnO | 0.18 ± 0.01 | --- | 0.18 ± 0.01 |
| MgO | 9.16 ± 0.21 | 1.2 ± 0.6 | 7.9 ± 0.6 |
| CaO | 4.25 ± 0.05 | 3.6 ± 1.5 | 0.7 ± 1.4 |
| Na ₂ O | 1.88 ± 0.12 | 1.2 ± 0.6 | 0.7 ± 0.5 |
| K ₂ O | 0.58 ± 0.02 | 0.3 ± 0.3 | 0.3 ± 0.2 |
| P ₂ O ₅ | 0.75 ± 0.04 | --- | 0.75 ± 0.04 |
| SO ₃ | 16.48 ± 0.19 | 3.4 ± 1.4 | 13.0 ± 1.5 |
| Cl | 1.09 ± 0.03 | --- | 1.09 ± 0.03 |
| H ₂ O | 14.20 ± 2.3 | 2.0 ± 0.8 | 12.1 ± 2.4 |

¹ Oxide wt% from APXS measurement of dump pile [108]; H₂O wt% from ChemCam [109]. ² Oxide wt% calculated from CheMin diffraction data using refined lattice parameter vs. composition equations from [24]. ³ Oxide wt % of bulk sample, crystalline component, and amorphous component, calculated using mass balance calculations. The composition of the amorphous component is obtained by subtracting the composition of the crystalline component from the bulk composition [41]. ⁴ Precision errors are 1s values.

At summer daytime temperatures on Mars, when the RH remains below a few %, it is likely that starkeyite will transform to Am-MgSO₄. At lower temperatures (and higher humidity) such as nighttime and winter conditions, both starkeyite and Am-MgSO₄ will be metastable, but the kinetics of transformation to more stable higher-hydrates are sluggish [104]. Starkeyite and Am-MgSO₄ will persist for durations longer than a Mars year and are the expected phases on the surface of Mars (see, for example, Figure 8 of [99]). Kieserite, the one-hydrate of MgSO₄ has been identified from orbit and has also been directly detected by CheMin in Tapo Caparo (TC, sol 3755, elevation −3880 m). The detection of kieserite is puzzling, since it should only form at temperatures above 50 °C; further analyses as *Curiosity* continues to climb the lower elevations of Mt. Sharp could provide some clues to its origin.

Mg sulfate hydrates are sensitive environmental indicators. The first Mg sulfate hydrate to form from a concentrated aqueous solution is either meridianite or epsomite, depending on temperature [99], and would dehydrate stepwise under warmer and drier conditions to produce starkeyite. The Martian environment(s) under which these higher hydrates of MgSO₄ were initially deposited (playa lake, efflorescence from subsurface brine, etc.) are not presently known because none of the detected sulfates appear to be primary. Once formed, aeolian weathering could have redeposited the sulfates in the sandstone sampled at Canaima. Mg sulfates are highly soluble; since the eolian sandstone hosting the sulfates is cemented, there must have been a cycle of wetting, drying, and cementation prior to the emplacement of the sulfates in their present form.

3.9. The Ubiquitous Amorphous Component

The aqueous dissolution of olivine, pyroxene, and basaltic glass should have resulted in significant quantities of amorphous silica (e.g., opal-A) on an early warm and wet Mars [110]. This was validated when opaline silica was discovered by the MER rover *Spirit* at Meridian Planum in concentrations as high as 90% [111], by the MER rover *Opportunity*

in Gusev Crater [112], and in a variety of locations from visible/near IR orbital data (e.g., [113]). However, it is enigmatic that amorphous materials are seen to persist in 3–3.5 Ga regolith on Mars since, in terrestrial settings, amorphous silica is uncommon in rocks more than a few million years old (e.g., [114]). Tosca and Knoll [115] discuss “juvenile precipitates”—precipitates that have undergone little diagenetic modification since their formation on Mars and conclude that the anomalous preservation of silica could result from a water-limited environment following their deposition, or from differences in the styles of tectonism and sedimentation between Earth and Mars.

Curiosity's discovery that nearly all the ~3.5 Ga old sedimentary rocks analyzed to date at Gale crater contain 15–70 wt.% X-ray amorphous material (e.g., [18,29,42,45,68,75,89,116–118]) only deepens this mystery. These amorphous materials could be glassy materials in the true sense, such as basaltic glass, or nanophase materials having only short-range order. Calculations of the quantity and composition of amorphous components using full-pattern fitting (FULLPAT; [35]) and mass balance equations [41] introduce systemic inaccuracies that can affect the resulting values to some extent; nevertheless, ancient amorphous materials appear to be both abundant and ubiquitous on Mars.

The calculated compositions of the amorphous components in Mars soil, and Bradbury Fm., Murray Fm., altered Murray Fm., Stimson Fm., altered Stimson Fm., and Sulfate-Bearing Unit (SBU) rocks exhibit distinct differences both within and between formations and lithologic units [68,118]. The major chemical species common to all amorphous components are FeO_t, SiO₂, and SO₃. Smith et al. [118,119] calculate the mixing relationship between FeO_t and SiO₂ and conclude that the hypothetical compositional endmembers are inconsistent with a volcanic or impact glass origin—they must therefore be the result of aqueous processes. This conclusion is supported by SAM-EGA data in which the volatile release temperatures of H₂O and SO₂ indicate that they are associated with the amorphous component (e.g., [61,120]). Cross-cutting relationships between stratigraphic units suggest that the most SiO₂-rich amorphous components result from interactions with localized fluids during late diagenesis. Low to moderate silica enrichments occurred during sediment deposition or early diagenesis. Table 10 lists the compositions of amorphous components in a representative sampling of rocks analyzed by *Curiosity*.

Table 10. Composition of the amorphous components of selected aeolian soil, Bradbury Fm., Murray Fm., Stimson Fm., and Sulfate-Bearing Unit samples analyzed by CheMin. RN = Rocknest, CB = Cumberland, MJ2 = Mojave 2, BK = Buckskin, BS = Big Sky, GH = Greenhorn, Ca = Canaima.

| Oxide % | Soil Avg. (RN, GB) | Bradbury Fm. (CM) | Murray Fm. (MJ 2) | Altered Murray Fm. (BK) | Stimson Fm. (BS) | Altered Stimson Fm. (GH) | Sulfate- Bearing Unit (CA) |
|--------------------------------|-----------------------|----------------------|----------------------|-------------------------------|---------------------|--------------------------------|----------------------------------|
| SiO ₂ | 37.50 | 25.557 | 55.725 | 75.9 | 24.133 | 63.525 | 30.5 |
| TiO ₂ | 2.711 | 3.659 | 2.487 | 2.18 | 6.587 | 1.537 | 1.54 |
| Al ₂ O ₃ | 4.253 | 0.000 | 7.196 | 0 | 0.123 | 0.000 | 0.8 |
| Cr ₂ O ₃ | 1.765 | 1.700 | 0.773 | 0.179 | 3.359 | 0.692 | 0.5 |
| FeO _T | 19.80 | 18.033 | 12.269 | 4.796 | 17.478 | 10.159 | 17.42 |
| MnO | 1.568 | 1.086 | 0.831 | 0.161 | 2.641 | 0.211 | 0.4 |
| MgO | 0.000 | 17.534 | 5.794 | 1.467 | 14.676 | 1.462 | 15.8 |
| CaO | 4.085 | 11.119 | 0.000 | 2.145 | 0.000 | 5.470 | 1.4 |
| Na ₂ O | 4.387 | 1.658 | 1.819 | 1.15 | 6.030 | 2.076 | 1.4 |
| K ₂ O | 1.903 | 0.532 | 1.111 | 0.847 | 1.402 | 0.461 | 0.6 |
| P ₂ O ₅ | 3.469 | 3.179 | 0.754 | 2.237 | 1.686 | 1.767 | 1.5 |
| SO ₃ | 16.13 | 11.544 | 10.342 | 7.75 | 17.076 | 11.934 | 26 |
| Cl | 2.418 | 4.398 | 0.899 | 0.52 | 4.809 | 0.707 | 2.2 |
| F | -- | 0.000 | 0.159 | 0 | 0.049 | 0.000 | --- |
| Proportion ¹ | 0.28 | 0.26 | 0.47 | 0.558 | 0.14 | 0.64 | |

¹ Proportion of X-ray amorphous material in the sample.

Smith et al. [118] speculate that, on Earth, amorphous materials are less likely to accumulate in the source-to-sink sedimentary rock cycle and are less likely to persist after burial (a consequence of plate tectonics). On Mars, conditions that existed during the deposition and diagenesis of amorphous materials appear to be more permissive of their

accumulation and preservation. However, the preservation of these amorphous materials for more than 3.5 Ga, a phenomenon unknown in terrestrial settings, remains a mystery.

Smith et al. [119] explore the nature of the amorphous sulfur-bearing phases in Murray Fm. sedimentary rocks. These authors report that 20 to 90% of the SO_3 resides in the amorphous component, consistent with Mg-S, Fe-S, and possibly Ca-S phases. The SAM Evolved Gas Analyzer (EGA) detects SO_2 with release temperatures and peak shapes consistent with Fe- and Mg-sulfur-bearing materials in most rocks analyzed prior to *Curiosity's* arrival at the Sulfate-Bearing Unit. Vaniman et al. [106] have shown that gypsum transforms to bassanite in the low-RH environment of the CheMin instrument over a period of several sols, and Chipera et al. [99] have shown that starkeyite ($\text{MgSO}_4 \cdot 4\text{H}_2\text{O}$) transforms to amorphous $\text{MgSO}_4 \cdot n\text{H}_2\text{O}$ in a matter of a few hours. Smith et al. [119] argue that the amorphous sulfur-bearing phase(s) were likely crystalline and became amorphous through dehydration in either the current Martian atmosphere or inside the CheMin instrument. The fact that CheMin did not detect these phases means that they are either below CheMin's detection limit (~1%), they were originally X-ray amorphous, or they became X-ray amorphous inside *Curiosity* prior to analysis by CheMin.

4. Discussion and Conclusions

As the first in situ crystallography instrument sent to another planet, CheMin has been responsible for a number of discoveries, many of which are described in Section 3. Three that are particularly noteworthy are highlighted below.

1. Discovery and characterization of habitable environments on early Mars. This was one of the principal goals of the MSL mission and was achieved with the first drilled sample at Yellowknife Bay. Requirements for habitability (“life as we know it”) include a source of the biogenic elements (H, C, O, N, P, S), a source of energy (minerals with variable redox states), high to moderate water activity, moderate temperatures, and moderate to neutral pH. A surprising discovery is that through hundreds of meters of lacustrine mudstones, corresponding to hundreds of thousands to millions of years [76], these requirements are satisfied, suggesting that habitable environments were common on early Mars. Mineralogical data are critical to the discovery and characterization of ancient habitable environments, and provide context for the morphologic, isotopic, and chemical data used to evaluate putative evidence of biogenicity. Equally importantly, post-depositional conditions of pressure, temperature, and chemical composition (P, T, X)—determined with a knowledge of the assemblage of minerals and mineral stability ranges—can through their actions preserve evidence of habitability or erase such evidence entirely.
2. The paragenesis of clay minerals. Prior to *Curiosity's* arrival in Gale crater, the paragenesis of clay minerals identified from orbital near-infrared reflectance spectra was poorly understood [5,6,66,121]. CheMin mineralogical results in combination with sedimentological observations demonstrate that (in all but two cases, whose origin is a matter of debate) the trioctahedral and dioctahedral smectites found were either authigenic or early diagenetic, formed in place in the sediments. CheMin data provided the ground truth for the orbital clay mineral detections at Glen Torridon, but clay minerals are also found in many areas in Gale crater traversed by *Curiosity* that do not exhibit clay mineral signatures in orbital data.
3. The ubiquitous presence of X-ray amorphous material in Gale crater sedimentary rocks. X-ray amorphous materials, whether they are glasses in the true sense or nanophase materials that lack long-range order, are found throughout Gale crater's sedimentary rocks. The discovery of amorphous materials in ~3.5 Ga on Mars is confounding, given that amorphous materials, inherently unstable, should crystallize in geologically short time periods. The amount and the elemental chemistry of the amorphous components vary in ways that suggest that they are the product of diagenetic events unique to the formations in which they are found.

In the nearly twelve years that *Curiosity* has been investigating Gale crater, the MSL science team has studied and documented over 800 vertical meters of flat-lying strata deposited and diagenetically altered on lower Mt. Sharp (e.g., Figure 10 and [75]). The sedimentology of these rocks reveals what in effect constituted the rock cycle on early Mars: in the absence of plate tectonics, sediments were deposited in fluvial, lacustrine, and aeolian environments, diagenetically altered and lithified. Subsequent exhumation/erosion by aeolian forces was followed by the deposition of younger sediments, which themselves were diagenetically altered, lithified, and eroded [84].

There is uncertainty as to the timing, quantity, and mechanism(s) of sediment infilling of Gale crater. Malin and Edgett [4], Grotzinger et al. [121] and Day and Kocurek [122], suggest that the crater had been completely infilled with sediment and later partially exhumed by aeolian forces. Kite et al. [123] propose a model in which the central mound of Gale was the result of aeolian infilling, achieving the approximate shape and size that it is today. This result is supported by the measurement of shallow dips ($\sim 3^\circ$) of sedimentary layers in directions away from the mound center, suggesting that there were 3 to 4 km of pre-erosional stratigraphic relief in the mound. Borlina et al. [124] utilize predicted thermal gradients and patterns of diagenesis (e.g., lack of evidence of the smectite to illite transition) to suggest that Yellowknife Bay sediments were never buried deeper than ~ 2 km. However, because the timing of the deposition of Yellowknife Bay sediments is not known with certainty, they could post-date the deposition of Mt. Sharp sediments. Lewis et al. [125] utilized accelerometers on the rover to measure the density of the sedimentary rock in lower Mt. Sharp and compared this result to calculated rock density based on CheMin mineralogy. These authors calculated a porosity of $40 \pm 6\%$, and estimated from this measurement that the upper limit of burial of these sediments was 1600–1800 m.

Palucis et al. [126] describe the physical sedimentology of Gale crater using orbital HiRISE (High Resolution Imaging Science Experiment) topographic data. These authors propose that there were at least three major lake stands within Gale crater, each persisting for perhaps 10^4 to 10^5 Earth years—all of which occurred after Mt. Sharp had attained its present size and approximate shape. The location and elevation of alluvial fans and deltas originating from the crater rim and from Mt. Sharp suggest that these lakes were as much as 700 m deep, covering the lower flank of Mt. Sharp and much of the stratigraphy traversed by *Curiosity*. The absolute ages of the lakes and the depositional events associated with them are not known with certainty, since many of the features are too small for crater counting to be useful. From [126] and references therein, the age of Gale crater is estimated to be ~ 3.8 to ~ 3.5 Ga, the age of the deposition of Mt. Sharp sediments and their subsequent erosion ~ 3.5 to ~ 3.1 Ga, and the age of deposition of the lacustrine, fluvial, and aeolian sediments traversed by *Curiosity* ~ 3.3 to 3.2 Ga. The timing of two events known with more certainty are the formation age of the detrital minerals in basaltic sediments of the Yellowknife Bay Fm. (4.21 ± 0.35 Ga, [65]) and the diagenetic age of jarosite in the Murray Fm. (2.12 ± 0.36 Ga, [80]) The latter suggests that subsurface aqueous diagenesis persisted (or recurred) for ~ 0.5 Ga after the last lake system dried up. Taken together, one can conclude that aqueous habitable environments (confirmed with mineralogical data) existed for hundreds of millions of years, at a time when evidence for primitive microbial life is found in rocks of equivalent age on Earth.

Given the complex depositional and diagenetic history of the sedimentary rocks traversed by *Curiosity*, it is perhaps not surprising that multiple and sometimes conflicting hypotheses have been put forward to explain the same observations. Nevertheless, there is no evidence that the sediments were ever deeply buried or extensively heated and, in many cases, primary sedimentary structures and original mineralogy remain. By way of comparison, as a consequence of plate tectonics, nearly all terrestrial rocks of this age have either been subducted and destroyed or metamorphically altered to the extent that little evidence remains of their provenance. Early Mars acts as a surrogate for early Earth in this regard, in the study of environments habitable for, and perhaps inhabited by, early life.

In the solar system, Mars is the only planet (other than Earth) that can be studied in this way. Of the other terrestrial planets, Venus has a surface temperature of $\sim 470^\circ\text{C}$, with the result that any early sedimentary record would have been highly altered. In addition, Venus has been extensively resurfaced so that no heavily cratered (i.e., ancient and unaltered) surfaces remain. The planet Mercury is a geochemical end member among the terrestrial planets, whose surface temperature varies from 430°C to -180°C . Little is known of the mineralogy of Mercury because the surface lacks diagnostic spectral absorption features in the UV-VIS region and spacecraft have never landed there. While future robotic missions are envisioned to each of these planets in the coming decades [127], they will be relatively short-lived landers (not rovers) and the ability to make scientific observations will be limited by the extremes of the environments.

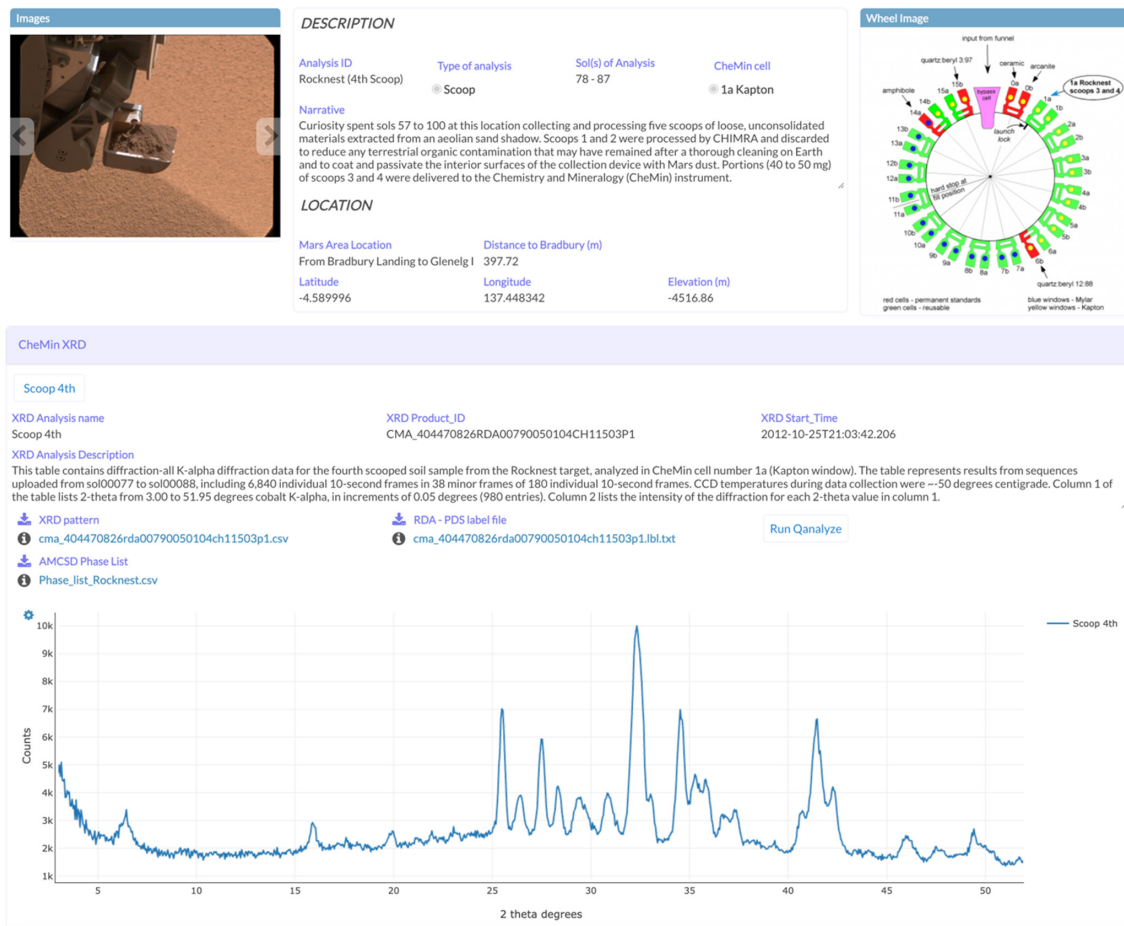
Hazen et al. [128] summarize what is currently known about the diversity and formation modes of Martian minerals and make comparison with the mineral diversity and mineral formation modes of Earth (e.g., [129,130] and references therein). The Martian data set includes results from both orbital and landed in situ observations and measurements from Martian meteorites. These authors conclude that the total mineral diversity of Mars is an order of magnitude less than that of the Earth, largely due to the absence of plate tectonics on Mars, and the presence of biologically mediated mineralization on the Earth.

Curiosity's in situ mineralogical analyses with CheMin have shown a wealth of detail not seen from orbit, and future missions of this type would undoubtedly provide more insights into Martian mineral diversity and mineral paragenetic modes. Dozens of geologically diverse and scientifically compelling landing sites have been identified and characterized from orbit as a result of the MER, MSL, and Mars 2020 site selection workshops [131–133]. To characterize the full mineralogical diversity of Mars, its early habitability, and its potential to support in situ resource utilization (ISRU) and eventual human exploration, comprehensive in situ science investigations are required at many diverse sites. A follow-on landed mission to Mars, the Mars 2020 *Perseverance* rover, arrived in Jezero crater in February 2021 [134]. *Perseverance* is characterizing and collecting samples of rock and regolith for possible return to Earth. The next proposed in situ mission to Mars is the Mars Life Explorer (MLE), a lander intended to drill and analyze a 2 m-long core of rock. CheMinX, a next generation powder XRD, is included in the strawman payload of that mission [135,136].

For the next several decades, pending NASA approval of the MLE mission or Mars Sample Return, CheMin data from MSL *Curiosity* will be the only in situ quantitative mineralogy available from Mars. CheMin data are archived at the Planetary Data System Geosciences Node (<https://pds-geosciences.wustl.edu/missions/msl/chemin.htm>, accessed on 3 May 2024) as are SAM data (<https://pds-geosciences.wustl.edu/missions/msl/sam.htm>, accessed on 3 May 2024) APXS data (<https://pds-geosciences.wustl.edu/missions/msl/apxs.htm>, accessed on 3 May 2024) and data from the other MSL *Curiosity* instruments. The “Gale Crater Mineralogy and Geochemistry Sample Database” [19] is a living repository of CheMin, SAM, and APXS data for each analyzed sample, from which all raw data, sample descriptions, on-line analysis tools, and open-access publications from the CheMin team can be downloaded. Figure 24 shows a screenshot of two data fields from a single CheMin data record. QAnalyze (<https://www.qanalyze.com/>) is a cloud-based whole-pattern fitting program that can be selected from within each data record or accessed as a standalone application. If chosen from within the database, QAnalyze will uplink the X-ray diffraction pattern for that sample as well as the list of the CheMin team's preferred AMCSD phases chosen for that analysis. The program returns whole-pattern fitting results, refined lattice parameters for each mineral, and allows the user to add or subtract phases from the AMCSD database to try to improve the fit.

MSL *Curiosity* will continue to climb Mt. Sharp for the coming Mars year (equivalent to about two Earth years) and perhaps longer, and we anticipate that there will be eight (or more) additional drilled sample analyses prior to mission's end. Orbital images show that many interesting features remain to be examined in detail on *Curiosity's* journey. One

of *Curiosity's* ultimate goals is a feature identified in orbital images called the “boxwork structure” [3,137], comprised of decameter-scale polygonal ridges that appear to be early diagenetic features formed in a subsurface phreatic groundwater zone [138]. The ridges in the boxwork structure, which are on average 5 m in width, are cemented fracture systems that are more resistant to erosion than the surrounding rock. The boxwork structures are exposed at an elevation of -3620 ± 50 m and extend along bedding for at least 10 km at this elevation. These structures could be a “Rosetta Stone” for deciphering the late-stage groundwater activity in Gale crater and globally, providing deeper insight into the geology and conditions of habitability of early Mars.



Morrison) and A.V.; investigation, D.B., V.T., T.B., E.R., D.V., S.C., P.S., R.M., S.M. (Shaunna Morrison), A.Y., R.D., R.H., A.T., D.M., G.D., C.A., N.C., T.P., D.D.M., P.C., B.L., B.T., E.H., S.S., R.W., M.T., J.M., A.P., M.G., P.D., J.B., L.T., A.M., C.O.-C., B.S., J.M.M., A.F., J.G., K.S., S.M. (Shaunna Morrison), A.V. and R.G.; formal analysis, D.B., V.T., T.B., E.R., D.V., S.C., P.S., R.M., S.M. (Shaunna Morrison), A.Y., R.D., R.H., A.T., D.M., G.D., C.A., N.C., T.P., D.D.M., P.C., B.L., B.T., E.H., S.S., R.W., M.T., J.M., A.P., M.G., P.D., J.B., L.T., A.M., C.O.-C., B.S., J.M.M., A.F., J.G., K.S., S.M. (Shaunna Morrison) and A.V.; investigation, D.B., M.T., T.B., E.R., D.V., S.C., P.S., R.M., S.M. (Shaunna Morrison), A.Y., R.D., R.H., A.T., D.M., G.D., C.A., N.C., T.P., D.D.M., P.C., B.L., B.T., E.H., S.S., R.W., M.T., J.M., A.P., M.G., P.D., J.B., L.T., A.M., C.O.-C., B.S., J.M.M., A.F., J.G., K.S., S.M. (Shaunna Morrison) and A.V.; data curation, D.B., T.B. and E.R.; writing—original draft preparation, D.B.; writing—review and editing, D.B. and V.T.; visualization, D.B. All authors have read and agreed to the published version of the manuscript.

Funding: Some of this research was carried out at the Jet Propulsion Laboratory, California Institute of Technology, under a contract with the National Aeronautics and Space Administration (NASA). All phases of CheMin development, deployment and surface operations were supported by NASA’s Science Mission Directorate under grant #MSL04-0014-0006.

Data Availability Statement: Publicly available datasets were analyzed in this study. These data can be found here: <https://pds.nasa.gov>, accessed on 23 July 2021. Additional contextual information can be found in the publicly available Gale crater Mineralogy and Geochemistry Sample Database found here: <https://doi.org/10.48484/JN48-YW52> (accessed on 7 May 2024).

Acknowledgments: We acknowledge the support of the Jet Propulsion Laboratory engineering and management teams and the MSL science team members who participated in tactical and strategic operations, without whom the data presented here could not have been collected.

Conflicts of Interest: The authors declare no conflicts of interest.

Appendix A

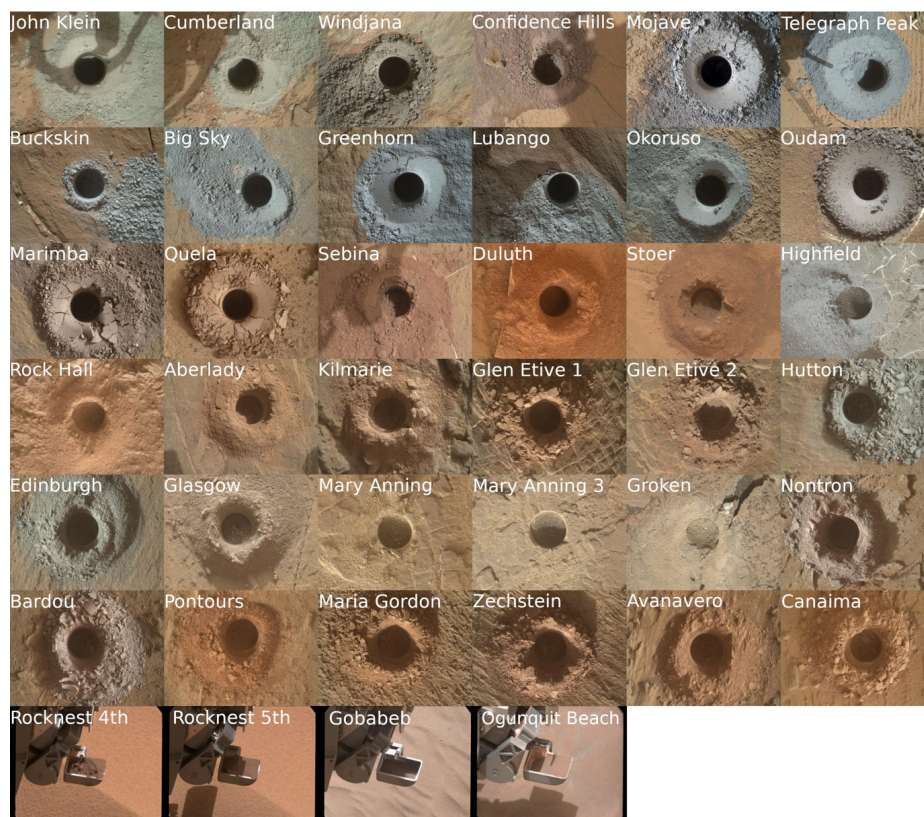


Figure A1. Images of drill holes and scooped aeolian material analyzed by CheMin to date.

Table A1. Details of CheMin drill samples and scooped aeolian soil during the 12-year deployment of MSL Curiosity on Mars.

| Analysis ID | Mars Area Location | Analysis Type | CheMin Cell | XRD Sol(s) of Analysis | Drill Sol | Elevation (m) |
|----------------------|--|---------------|-------------|------------------------|-----------|---------------|
| Rocknest (4th Scoop) | From Bradbury Landing to Glenelg Intrigue | Scoop | 1a Kapton | 78–87 | 74 | −4516.86 |
| Rocknest (5th scoop) | From Bradbury Landing to Glenelg Intrigue | Scoop | 7a mylar | 94–119 | 93 | −4516.86 |
| John Klein | Yellowknife Bay | Drill | 13b mylar | 195–272, 473–488 | 182 | −4520.46 |
| Cumberland | Yellowknife Bay | Drill | 12b mylar | 282–432 | 279 | −4520.24 |
| Windjana | Kimberley | Drill | 13a mylar | 623–694 | 621 | −4478.55 |
| Confidence Hills | Pahrump Hills, Murray formation | Drill | 12a mylar | 765–785 | 756 | −4460.62 |
| Mojave2 | Pahrump Hills, Murray formation | Drill | 6a Kapton | 884–894 | 867 | −4459.71 |
| Telegraph Peak | Pahrump Hills, Murray formation | Drill | 5b Kapton | 922–949 | 905 | −4453.51 |
| Buckskin | Pahrump Hills, Murray formation | Drill | 14b Kapton | 1061–1078 | 1060 | −4447.04 |
| Big Sky | Naukluft Plateau | Drill | 7b mylar | 1121–1131 | 1116 | −4434.42 |
| Greenhorn | Naukluft Plateau | Drill | 8a mylar | 1139–1148 | 1134 | −4434.23 |
| Gobabeb | Bagnold Dune Field | Scoop | 7a mylar | 1227–1280 | 1224 | −4423.76 |
| Lubango | Naukluft Plateau | Drill | 8a mylar | 1323–1330 | 1320 | −4429.04 |
| Okoruso | Naukluft Plateau | Drill | 7b mylar | 1334–1346 | 1332 | −4429.17 |
| Oudam | Hartmann’s Valley member, Murray formation | Drill | 12a mylar | 1362–1369 | 1361 | −4435.68 |
| Oudam 13a | Hartmann’s Valley member, Murray formation | Drill | 13a mylar | 1375–1387 | 1375 | −4435.59 |
| Marimba2 | Karasburg member, Murray formation | Drill | 8b mylar | 1425–1436 | 1422 | −4410.68 |
| Quela | Karasburg member, Murray formation | Drill | 5a Kapton | 1470–1480 | 1464 | −4379.26 |
| Sebina | Sutton Island member, Murray formation | Drill | 4b Kapton | 1496–1507 | 1495 | −4360.89 |
| Ogunquit Beach | Bagnold Dune | Scoop | 1a Kapton | 1832–1931 | 1829? | −4299.95 |
| Duluth | Blunts Point member, Vera Rubin ridge | Drill | 13b mylar | 2068–2095 | 2057 | −4191.63 |
| Stoer | Pettegrove Point member, Vera Rubin ridge | Drill | 10a mylar | 2141–2151 | 2136 | −4170.39 |
| Highfield | Jura member, Vera Rubin ridge | Drill | 10a mylar | 2226–2242 | 2224 | −4146.75 |
| Rock Hall | Jura member, Vera Rubin ridge | Drill | 7b mylar | 2264–2284 | 2261 | −4143.69 |
| Aberlady | Clay-bearing unit—Glen Torridon | Drill | 8a mylar | 2373–2384 | 2370 | −4157.79 |
| Kilmarie | Clay-bearing unit—Glen Torridon | Drill | 9b mylar | 2388–2400 | 2384 | −4157.93 |
| Glen Etive 1 | Glen Torridon | Drill | 8b mylar | 2492–2503 | 2486 | −4132.99 |
| Glen Etive 2 | Glen Torridon | Drill | 8a mylar | 2543–2555 | 2527 | −4132.95 |
| Hutton | Glen Torridon | Drill | 12a mylar | 2672–2678 | 2668 | −4095.84 |
| Edinburgh | Glen Torridon | Drill | 7b mylar | 2715–2723 | 2711 | −4088.44 |
| Glasgow | Glen Torridon | Drill | 7b mylar | 2758–2774 | 2754 | −4107.93 |
| Mary Anning | Glen Torridon | Drill | 7a mylar | 2842–2854 | 2828? | −4128.06 |
| Mary Anning 3 | Glen Torridon | Drill | 7a mylar | 2888–2894 | 2870 | −4128.06 |
| Groken | Glen Torridon | Drill | 9a mylar | 2912–2930 | 2910 | −4127.91 |
| Nontron | Clay mineral—Sulfate mineral transition region | Drill | 9a mylar | 3058–3077 | 3056 | −4072.91 |
| Bardou | Clay mineral—Sulfate mineral transition region | Drill | 4a Kapton | 3097–3113 | 3094 | −4066.48 |
| Pontours | Clay mineral—Sulfate mineral transition region | Drill | 1a Kapton | 3172 | 3170 | −4041.25 |
| Maria Gordon | Clay mineral—Sulfate mineral transition region | Drill | 1a Kapton | 3232 | 3229 | −4015.23 |
| Zechstein | Clay mineral—Sulfate mineral transition region | Drill | 1a Kapton | 3292 | 3289 | −3991.11 |
| Avanavero | Clay mineral—Sulfate mineral transition region | Drill | 15a Kapton | 3517–3520 | 3512 | −3920 |
| Canaima | Sulfate Bearing Unit | Drill | 15a Kapton | 3614 | 3612 | −3880 |
| Tapo Caparo | Sulfate Bearing Unit | Drill | 15a Kapton | 3755 | 3752 | −3860 |
| Ubajara | Sulfate Bearing Unit | Drill | 15a Kapton | 3825–3827 | 3823 | −3800 |
| Sequoia | Sulfate Bearing Unit | Drill | 1b Kapton | 3982–3991 | 3982 | −3760 |
| Mineral King | Sulfate Bearing Unit | Drill | 2a Kapton | 4113 | 4110 | |

References

1. Anderson, R.C.; Jandura, L.; Okon, A.B.; Sunshine, D.; Roumeliotis, C.; Beegle, L.W.; Hurowitz, J.; Kennedy, B.; Limonadi, D.; McCloskey, S.; et al. Collecting Samples in Gale Crater, Mars; an Overview of the Mars Science Laboratory Sample Acquisition, Sample Processing and Handling System. *Space Sci. Rev.* **2012**, *170*, 57–75. [[CrossRef](#)]
2. Blake, D.; Vaniman, D.; Achilles, C.; Anderson, R.; Bish, D.; Bristow, T.; Chen, C.; Chipera, S.; Crisp, J.; Marais, D.D.; et al. Characterization and Calibration of the CheMin Mineralogical Instrument on Mars Science Laboratory. *Space Sci. Rev.* **2012**, *170*, 341–399. [[CrossRef](#)]
3. Thomson, B.J.; Bridges, N.T.; Milliken, R.; Baldrige, A.; Hook, S.J.; Crowley, J.K.; Marion, G.M.; de Souza Filho, C.R.; Brown, A.J.; Weitz, C.M. Constraints on the origin and evolution of the layered mound in Gale Crater, Mars using Mars Reconnaissance Orbiter data. *Icarus* **2011**, *214*, 413–432. [[CrossRef](#)]
4. Malin, M.C.; Edgett, K.S. Sedimentary rocks of early Mars. *Science* **2000**, *290*, 1927–1937. [[CrossRef](#)] [[PubMed](#)]
5. Milliken, R.E.; Grotzinger, J.P.; Thomson, B.J. Paleoclimate of Mars as captured by the stratigraphic record in Gale Crater. *Geophys. Res. Lett.* **2010**, *37*, L04201. [[CrossRef](#)]
6. Fraeman, A.A.; Arvidson, R.E.; Catalano, J.G.; Grotzinger, J.P.; Morris, R.V.; Murchie, S.L.; Stack, K.M.; Humm, D.C.; McGovern, J.A.; Seelos, F.P.; et al. A hematite-bearing layer in Gale Crater, Mars: Mapping and implications for past aqueous conditions. *Geology* **2013**, *41*, 1103–1106. [[CrossRef](#)]
7. Fraeman, A.A.; Ehlmann, B.L.; Arvidson, R.E.; Edwards, C.S.; Grotzinger, J.P.; Milliken, R.E.; Quinn, D.P.; Rice, M.S. The stratigraphy and evolution of lower Mount Sharp from spectral, morphological, and thermophysical orbital data sets. *J. Geophys. Res. Planets* **2016**, *121*, 1713–1736. [[CrossRef](#)] [[PubMed](#)]
8. Grotzinger, J.P.; Crisp, J.; Vasavada, A.R.; Anderson, R.C.; Baker, C.J.; Barry, R.; Blake, D.F.; Conrad, P.; Edgett, K.S.; Ferdowski, B.; et al. Mars Science Laboratory Mission and Science Investigation. *Space Sci. Rev.* **2012**, *170*, 5–56. [[CrossRef](#)]
9. Edgett, K.S.; Yingst, R.A.; Ravine, M.A.; Caplinger, M.A.; Maki, J.N.; Ghaemi, F.T.; Schaffner, J.A.; Bell, J.F.; Edwards, L.J.; Herkenhoff, K.E.; et al. Curiosity's Mars Hand Lens Imager (MAHLI) Investigation. *Space Sci. Rev.* **2012**, *170*, 259–317. [[CrossRef](#)]
10. Malin, M.C.; Caplinger, M.A.; Edgett, K.S.; Ghaemi, F.T.; Ravine, M.A.; Schaffner, J.A.; Baker, J.M.; Bardis, J.D.; DiBiase, D.R.; Maki, J.N.; et al. The Mars Science Laboratory (MSL) Mast-mounted Cameras (Mastcams) Flight Instruments. In Proceedings of the 41st Lunar and Planetary Science Conference, The Woodlands, TX, USA, 1–5 March 2010. Available online: <https://www.lpi.usra.edu/meetings/lpsc2010/pdf/1123.pdf> (accessed on 3 May 2024).
11. Gellert, R.; Rieder, R.; Brückner, J.; Clark, B.C.; Dreibus, G.; Klingelhöfer, G.; Lugmair, G.; Ming, D.W.; Wänke, H.; Yen, A.; et al. Alpha Particle X-ray Spectrometer (APXS): Results from Gusev crater and calibration report. *J. Geophys. Res.* **2006**, *111*, E02S05. [[CrossRef](#)]
12. Campbell, J.L.; Perrett, G.M.; Gellert, R.; Andrushenko, S.M.; Boyd, N.I.; Maxwell, J.A.; King, P.L.; Schofield, C.D.M. Calibration of the Mars Science Laboratory Alpha Particle X-ray Spectrometer. *Space Sci. Rev.* **2012**, *170*, 319–340. [[CrossRef](#)]
13. Maurice, S.; Wiens, R.C.; Saccoccio, M.; Barraclough, B.; Gasnault, O.; Forni, O.; Mangold, N.; Baratoux, D.; Bender, S.; Berger, G.; et al. ChemCam Activities and Discoveries during the Nominal Mission of Mars Science Laboratory in Gale crater, Mars. *Space Sci. Rev.* **2012**, *170*, 95–166. [[CrossRef](#)]
14. Wiens, R.C.; Maurice, S.; Barraclough, B.; Saccoccio, M.; Barkley, W.C.; Bell, J.F., III; Bender, S.; Bernardin, J.; Blaney, D.; Blank, J.; et al. The ChemCam Instrument Suite on the Mars Science Laboratory (MSL) Rover: Body Unit and Combined System Tests. *Space Sci. Rev.* **2012**, *170*, 167–227. [[CrossRef](#)]
15. Mahaffy, P.R.; Webster, C.R.; Cabane, M.; Conrad, P.G.; Coll, P.; Atreya, S.K.; Arvey, R.; Barciniak, M.; Benna, M.; Bleacher, L.; et al. The Sample Analysis at Mars Investigation and Instrument Suite. *Space Sci. Rev.* **2012**, *170*, 401–478. [[CrossRef](#)]
16. Johnson, D.L.; Carroll, B.C.; Leland, R.S. MSL/CheMin Cryocooler System Requirements and Characterization Tests. In Proceedings of the 15th International Cryocooler Conference Long Beach, Long Beach, CA, USA, 9–12 June 2008; In Cryocoolers 15. pp. 621–630.
17. Lafuente, B.; Blake, D.; Bristow, T.; Rampe, E.; Downs, R.; Sarrazin, P.; Downs, G.; Stone, N.; Pires, A.; Vaniman, D.; et al. Gale Crater Mineralogy and Geochemistry Sample Database (GCMGS). [Data set]. *Open Data Repos.* **2021**. [[CrossRef](#)]
18. Morrison, S.M.; Downs, R.T.; Blake, D.F.; Vaniman, D.T.; Ming, D.W.; Hazen, R.M.; Treiman, A.H.; Achilles, C.N.; Yen, A.S.; Morris, R.V.; et al. Crystal Chemistry of Martian Minerals from Bradbury Landing through Naukluft Plateau, Gale crater, Mars. *Am. Miner.* **2018**, *103*, 857–871. [[CrossRef](#)]
19. Lafuente, B.; Downs, R.T.; Yang, H.; Stone, N. Highlights in Mineralogical Crystallography. Armbruster, T., Danisi, R.M., Eds.; W. De Gruyter: Berlin, Germany, 2015; pp. 1–30. Available online: <https://rruff.info/about/downloads/HMC1-30.pdf> (accessed on 3 May 2024).
20. Morris, R.V.; Vaniman, D.T.; Blake, D.F.; Gellert, R.; Chipera, S.J.; Rampe, E.B.; Ming, D.W.; Morrison, S.M.; Downs, R.T.; Treiman, A.H.; et al. Silicic volcanism on Mars evidenced by tridymite in high-SiO₂ sedimentary rock at Gale crater. *Proc. Natl. Acad. Sci. USA* **2016**, *113*, 7071–7076. [[CrossRef](#)] [[PubMed](#)]
21. Dera, P.; Zhuravlev, K.; Prakapenka, V.; Rivers, M.L.; Finkelstein, G.J.; Grubor-Urosevic, O.; Tschauer, O.; Clark, S.M.; Downs, R.T. High pressure single-crystal micro-X-ray diffraction analysis with GSE_ADA/RSV software. *High Press. Res.* **2013**, *33*, 466–484. [[CrossRef](#)]
22. Bish, D.L.; Howard, S.A. Quantitative phase analysis using the Rietveld method. *J. Appl. Crystallogr.* **1988**, *21*, 86–91. [[CrossRef](#)]

23. Bish, D.L.; Post, J.E. Quantitative mineralogical analysis using the Rietveld full-pattern fitting method. *Am. Miner.* **1993**, *78*, 932–942.
24. Morrison, S.M.; Downs, R.T.; Blake, D.F.; Prabhu, A.E.; Vaniman, D.T.; Ming, D.W.; Rampe, E.B.; Hazen, R.M.; Achilles, C.N.; Treiman, A.H.; et al. Relationships between unit-cell parameters and composition for rock-forming minerals on Earth, Mars, and other extraterrestrial bodies. *Am. Miner.* **2018**, *103*, 848–856. [[CrossRef](#)]
25. Morrison, S.M.; David, F.B.; Thomas, F.B.; Nicholas, C.; Steve, J.C.; Patricia, I.C.; Robert, T.D.; Amed, E.; Robert, M.H.; Johannes, M.M.; et al. Expanded Insights into Martian Mineralogy: Updated Analysis of Gale Crater’s Mineral Composition via CheMin Crystal Chemical Investigations. *Minerals*, 2024; *in the press*.
26. Patterson, A.L. The Diffraction of X-rays by Small Crystalline Particles. *Phys. Rev.* **1939**, *56*, 972. [[CrossRef](#)]
27. Bristow, T.F.; Bish, D.L.; Vaniman, D.T.; Morris, R.V.; Blake, D.F.; Grotzinger, J.P.; Rampe, E.B.; Crisp, J.A.; Achilles, C.N.; Ming, D.W.; et al. The origin and implications of clay minerals from Yellowknife Bay, Gale crater, Mars. *Am. Mineral.* **2015**, *100*, 824–836. [[CrossRef](#)] [[PubMed](#)]
28. Bristow, T.F.; Rampe, E.B.; Achilles, C.N.; Blake, D.F.; Chipera, S.J.; Craig, P.; Crisp, J.A.; Marais, D.J.D.; Downs, R.T.; Gellert, R.; et al. Clay mineral diversity and abundance in sedimentary rocks of Gale crater, Mars. *Sci. Adv.* **2018**, *4*, eaar3330. [[CrossRef](#)] [[PubMed](#)]
29. Vaniman, D.T.; Bish, D.L.; Ming, D.W.; Bristow, T.F.; Morris, R.V.; Blake, D.F.; Chipera, S.J.; Treiman, A.H.; Rampe, E.B.; Rice, M.; et al. Mineralogy of a mudstone at Yellowknife Bay, Gale crater, Mars. *Science* **2014**, *343*, 1243480. [[CrossRef](#)] [[PubMed](#)]
30. Moore, D.M.; Reynolds, R.C., Jr. *X-ray Diffraction and the Identification and Analysis of Clay Minerals*; Oxford University Press: Oxford, UK, 1997; 400p, ISBN 9780195087130.
31. Bristow, T.F.; Grotzinger, J.P.; Rampe, E.B.; Cuadros, J.; Chipera, S.J.; Downs, G.W.; Fedo, C.M.; Frydenvang, J.; McAdam, A.C.; Morris, R.V.; et al. Brine Driven Diagenesis of Clay Minerals in Gale Crater, Mars. *Science* **2021**, *373*, 198–204. [[CrossRef](#)]
32. Thorpe, M.T.; Bristow, T.F.; Rampe, E.B.; Tosca, N.J.; Grotzinger, J.P.; Bennett, K.A.; Achilles, C.N.; Blake, D.F.; Chipera, S.J.; Downs, G.; et al. Mars Science Laboratory CheMin data from the Glen Torridon region and the significance of lake-groundwater interactions in interpreting mineralogy and sedimentary history. *JGR Planets* **2022**, *127*, e2021JE007099. [[CrossRef](#)]
33. Bergmann, J. Rietveld Analysis Program BGMN Manual. 2005. Available online: http://www.bgmn.de/BGMN_manual_2005.pdf (accessed on 3 May 2024).
34. McAdam, A.C.; Sutter, B.; Archer, P.D.; Franz, H.B.; Wong, G.M.; Lewis, J.M.T.; Eigenbrode, J.L.; Stern, J.C.; Knudson, C.A.; Clark, J.; et al. Constraints on the mineralogy and geochemistry of Vera Rubin ridge, Gale crater, Mars, from Mars Science Laboratory Sample Analysis at Mars evolved gas analyses. *J. Geophys. Res. Planets* **2020**, *125*, e2019JE006309. [[CrossRef](#)]
35. Chipera, S.J.; Bish, D.L. FULLPAT: A full-pattern quantitative analysis program for X-ray powder diffraction using measured and calculated patterns. *J. Appl. Crystallogr.* **2002**, *35*, 744–749. [[CrossRef](#)]
36. Chipera, S.J.; Bish, D.L. Fitting full X-ray diffraction patterns for quantitative analysis: A method for readily quantifying crystalline and disordered phases. *Adv. Mater. Phys. Chem.* **2013**, *3*, 47. [[CrossRef](#)]
37. Chung, F.H. Quantitative interpretation of X-ray diffraction patterns of mixtures. I. Matrix-flushing method for quantitative multicomponent analysis. *J. Appl. Crystallogr.* **1974**, *7*, 519–525. [[CrossRef](#)]
38. Chung, F.H. Quantitative Interpretation of X-ray Diffraction Patterns of Mixtures. II. Adiabatic Principle of X-ray Diffraction Analysis of Mixtures. *J. Appl. Crystallogr.* **1974**, *7*, 526–531. [[CrossRef](#)]
39. Achilles, C.N.; Morris, R.V.; Chipera, S.J.; Ming, D.W.; Rampe, E.B. X-ray diffraction reference intensity ratios of amorphous and poorly crystalline phases: Implications for CheMin on the Mars Science Laboratory Mission. In Proceedings of the 44th Lunar and Planetary Science Conference, The Woodlands, TX, USA, 18–22 March 2013. Available online: <https://www.lpi.usra.edu/meetings/lpsc2013/pdf/3072.pdf> (accessed on 3 May 2024).
40. Rampe, E.B.; Bish, D.L.; Chipera, S.J.; Morris, R.V.; Achilles, C.N.; Ming, D.W.; Blake, D.F.; Anderson, R.C.; Bristow, T.F.; Crisp, J.A.; et al. Detecting Nanophase Weathering Products with CheMin: Reference Intensity Ratios of Allophane, Aluminosilicate Gel, and Ferrihydrite. In Proceedings of the 44th Lunar and Planetary Science Conference, The Woodlands, TX, USA, 18–22 March 2013; Available online: <https://www.lpi.usra.edu/meetings/lpsc2013/pdf/1188.pdf> (accessed on 3 May 2024).
41. Smith, R.J.; Rampe, E.B.; Horgan, B.H.N.; Dehouck, E. Deriving amorphous component abundance and composition of rocks and sediments on Earth and Mars. *J. Geophys. Res. Planets* **2018**, *123*, 2485–2505. [[CrossRef](#)]
42. Blake, D.F.; Morris, R.V.; Kocurek, G.; Morrison, S.M.; Downs, R.T.; Bish, D.; Ming, D.W.; Edgett, K.S.; Rubin, D.; Goetz, W.; et al. Characterization and analysis of the Rocknest sand shadow. *Science* **2013**, *341*, 1239505. [[CrossRef](#)]
43. Bish, D.L.; Blake, D.F.; Vaniman, D.T.; Chipera, S.J.; Morris, R.V.; Ming, D.W.; MSL Team. X-Ray Diffraction Results from Mars Science Laboratory: Mineralogy of Rocknest Aeolian Bedform at Gale crater. *Science* **2013**, *341*, 1238932. [[CrossRef](#)]
44. Bish, D.; Blake, D.; Vaniman, D.; Sarrazin, P.; Bristow, T.; Achilles, C.; Dera, P.; Chipera, S.; Crisp, J.; Downs, R.T.; et al. The first X-ray diffraction measurements on Mars. *IUCrj* **2014**, *1*, 514–522. [[CrossRef](#)]
45. Achilles, C.N.; Downs, R.T.; Ming, D.W.; Rampe, E.B.; Morris, R.V.; Treiman, A.H.; Morrison, S.M.; Blake, D.F.; Vaniman, D.T.; Ewing, R.C.; et al. Mineralogy of an active eolian sediment from the Namib dune, Gale crater, Mars. *J. Geophys. Res. Planets* **2017**, *122*, 2344–2361. [[CrossRef](#)]
46. Ehlmann, B.L.; Edgett, K.S.; Sutter, B.; Achilles, C.N.; Litvak, M.L.; Lapotre, M.G.A.; Sullivan, R.; Fraeman, A.A.; Arvidson, R.E.; Blake, D.F.; et al. Chemistry, mineralogy, and grain properties at Namib and High dunes, Bagnold dune field, Gale crater, Mars: A synthesis of Curiosity rover observations. *J. Geophys. Res. Planets* **2017**, *122*, 2510–2543. [[CrossRef](#)]

47. Lapotre, M.G.A.; Rampe, E.B. Curiosity's Investigation of the Bagnold Dunes, Gale Crater: Overview of the Two-Phase Scientific Campaign and Introduction to the Special Collection. *Geophys. Res. Lett.* **2018**, *45*, 10200–10210. [[CrossRef](#)]
48. Rampe, E.B.; Lapotre, M.G.A.; Bristow, T.F.; Arvidson, R.E.; Morris, R.V.; Achilles, C.N.; Weitz, C.; Blake, D.F.; Ming, D.W.; Morrison, S.M.; et al. Sand Mineralogy Within the Bagnold Dunes, Gale Crater, as Observed In Situ and From Orbit. *J. Geophys. Res. Planets* **2018**, *45*, 9488–9497. [[CrossRef](#)]
49. Herkenhoff, K.E.; Grotzinger, J.; Knoll, A.H.; McLennan, S.M.; Weitz, C.; Yingst, A.; Anderson, R.; Archinal, B.A.; Arvidson, R.E.; Barrett, J.M.; et al. Surface processes recorded by rocks and soils on Meridiani Planum, Mars: Microscopic Imager observations during Opportunity's first three extended missions. *J. Geophys. Res.* **2008**, *113*, E12S32. [[CrossRef](#)]
50. Sullivan, R.; Banfield, D.; Bell, J.F., III; Calvin, W.; Fike, D.; Golombek, M.; Greeley, R.; Grotzinger, J.; Herkenhoff, K.; Jerolmack, D.; et al. Aeolian processes at the Mars exploration rover Meridiani Planum landing site. *Nature* **2005**, *436*, 58–61. [[CrossRef](#)]
51. Sullivan, R.; Arvidson, R.; Bell, J.F., III; Gellert, R.; Golombek, M.; Greeley, R.; Herkenhoff, K.; Johnson, J.; Thompson, S.; Whelley, P.; et al. Wind-driven particle mobility on Mars: Insights from Mars Exploration Rover observations at "El Dorado" and surroundings at Gusev Crater. *J. Geophys. Res.* **2008**, *113*, E06S07. [[CrossRef](#)]
52. Soderblom, L.A.; Anderson, R.C.; Arvidson, R.E.; Bell, J.F.; Cabrol, N.A.; Calvin, W.; Christensen, P.R.; Clark, B.C.; Economou, T.; Ehlmann, B.L.; et al. Soils of Eagle Crater and Meridian Planum at the Opportunity Rover Landing Site. *Science* **2004**, *306*, 1723–1726. [[CrossRef](#)] [[PubMed](#)]
53. Golombek, M.; Robinson, K.; McEwen, A.; Bridges, N.; Ivanov, B.; Tornabene, L.; Sullivan, R. Constraints on ripple migration at Meridiani Planum from Opportunity and HiRISE observations of fresh craters. *J. Geophys. Res.* **2010**, *115*, E00F08. [[CrossRef](#)]
54. Ward, W.R. Large-scale variations in the obliquity of Mars. *Science* **1973**, *181*, 260–262. [[CrossRef](#)] [[PubMed](#)]
55. Laskar, J.; Levrard, B.; Mustard, J.F. Large-scale variations in the obliquity of Mars. *Nature* **2002**, *419*, 375–377. [[CrossRef](#)]
56. Laue, M.; Friedrich, W.; Knipping, P. Die Wellentheorie der Röntgenstrahlen. *Sitzungsb. K. Bayer. Akad. Wiss. Math.-Phys. Klasse* **1912**, 303–322.
57. Ming, D.W.; Gellert, R.; Morris, R.V.; Arvidson, R.E.; Brückner, J.; Clark, B.C.; Cohen, B.A.; D'Uston, C.; Economou, T.; Fleischer, I.; et al. Geochemical properties of rocks and soils in Gusev crater, mars: Results of the alpha particle X-ray spectrometer from Cumberland Ridge to home plate. *J. Geophys. Res.* **2008**, *113*, E12S39. [[CrossRef](#)]
58. Morris, R.V.; Klingelhöfer, G.; Schröder, C.; Fleischer, I.; Ming, D.W.; Yen, A.S.; Gellert, R.; Arvidson, R.E.; Rodionov, D.S.; Crumpler, L.S.; et al. Iron mineralogy and aqueous alteration from Husband Hill through Home Plate at Gusev crater, Mars: Results from the Mössbauer instrument on the Spirit Mars Exploration Rover. *J. Geophys. Res.* **2008**, *113*, E12S42. [[CrossRef](#)]
59. McSween, H.Y., Jr.; Taylor, G.J.; Wyatt, M.B. Elemental composition of the Martian crust. *Science* **2009**, *324*, 736–739. [[CrossRef](#)]
60. Taylor, S.R.; McLennan, S.M. *Planetary Crusts: Their Composition, Origin and Evolution*; Cambridge University Press: Cambridge, UK, 2009; 378p.
61. Leshin, L.A.; Mahaffy, P.R.; Webster, C.R.; Cabane, M.; Coll, P.; Conrad, P.G.; Archer, P.D.; Atreya, S.K.; Brunner, A.E.; Buch, A.; et al. Volatile, isotope, and organic analysis of martian fines with the Mars Curiosity rover. *Science* **2013**, *341*, 1238937. [[CrossRef](#)]
62. Rice, M.S.; Gupta, S.; Treiman, A.H.; Stack, K.M.; Calef, F.; Edgar, L.A.; Grotzinger, J.; Lanza, N.; Le Deit, L.; Lasue, J.; et al. Geologic overview of the Mars Science Laboratory rover mission at the Kimberley, Gale crater, Mars. *J. Geophys. Res. Planets* **2017**, *122*, 2–20. [[CrossRef](#)]
63. Grotzinger, J.P.; Dietrich, W.E.; Gupta, S.; Sumner, D.Y.; Wiens, R.C.; Mangold, N.; Malin, M.C.; Edgett, K.S.; Maurice, S.; Forni, O.; et al. Variability in martian sinuous ridge form: Case study of Aeolis Serpens in the Aeolis Dorsa, Mars, and insight from the Mirackina paleoriver, South Australia. *Science* **2013**, *340*, 1068–1072. [[CrossRef](#)]
64. Treiman, A.H.; Morris, R.V.; Agresti, D.G.; Graff, T.G.; Achilles, C.N.; Rampe, E.B.; Bristow, T.F.; Ming, D.W.; Blake, D.F.; Vaniman, D.T.; et al. Ferrian saponite from the Santa Monica Mountains (California, USA, Earth): Characterization as an analog for clay minerals on Mars with application to Yellowknife Bay in Gale Crater. *Am. Min.* **2014**, *99*, 2234–2250. [[CrossRef](#)]
65. Farley, K.A.; Malespin, C.; Mahaffy, P.; Grotzinger, J.P.; Vasconcelos, P.M.; Milliken, R.E.; Malin, M.; Edgett, K.S.; Pavlov, A.A.; Hurowitz, J.A.; et al. In situ radiometric and exposure age dating of the Martian surface. *Science* **2014**, *343*, 1247166. [[CrossRef](#)] [[PubMed](#)]
66. Ehlmann, B.L.; Mustard, J.F.; Murchie, S.L.; Bibring, J.-P.; Meunier, A.; Fraeman, A.A.; Langevin, Y. Evidence for low-grade metamorphism, hydrothermal alteration, and diagenesis on Mars from phyllosilicate mineral assemblages. *Nature* **2011**, *479*, 53–60. [[CrossRef](#)] [[PubMed](#)]
67. Grotzinger, J.P.; Sumner, D.Y.; Kah, L.C.; Stack, K.; Gupta, S.; Edgar, L.; Rubin, D.; Lewis, K.; Schieber, J.; Mangold, N.; et al. A habitable fluvio-lacustrine environment at Yellowknife Bay, Gale Crater, Mars. *Science* **2014**, *343*, 1242777. [[CrossRef](#)] [[PubMed](#)]
68. Treiman, A.H.; Bish, D.L.; Vaniman, D.T.; Chipera, S.J.; Blake, D.F.; Ming, D.W.; Morris, R.V.; Bristow, T.F.; Morrison, S.M.; Baker, M.B.; et al. Mineralogy and genesis of the Windjana sandstone, Kimberley area, Gale Crater, Mars. *JGR Planets* **2015**, *121*, 75–106. [[CrossRef](#)] [[PubMed](#)]
69. Tu, V.M.; Rampe, E.B.; Bristow, T.F.; Thorpe, M.T.; Clark, J.V.; Castle, N.; Fraeman, A.A.; Edgar, L.A.; McAdam, A.; Bedford, C.; et al. A Review of the Phyllosilicates in Gale Crater as Detected by the CheMin Instrument on the Mars Science Laboratory, Curiosity Rover. *Minerals* **2021**, *11*, 847. [[CrossRef](#)]

70. Mangold, N.; Dehouck, E.; Fedo, C.; Forni, O.; Achilles, C.; Bristow, T.; Downs, R.; Frydenvang, J.; Gasnault, O.; L'Haridon, J.; et al. Chemical alteration of fine-grained sedimentary rocks at Gale crater. In Proceedings of the Fourth International Conference on Early Mars, Flagstaff, AZ, USA, 2–10 October 2017. Bibcode: 2017LPICo2014,3013M.
71. Fedo, C.; Grotzinger, J.; Gupta, S.; Stein, N.T.; Watkins, J.; Banham, S.; Edgett, K.S.; Minitti, M.; Schieber, J.; Sebach, K.; et al. Facies Analysis and Basin Architecture of the Upper Part of the Murray Formation, Gale Crater, Mars. In Proceedings of the Lunar and Planetary Science Conference 48, Woodlands, TX, USA, 20–24 March 2017; Available online: <https://www.hou.usra.edu/meetings/lpsc2017/pdf/1689.pdf> (accessed on 3 May 2024).
72. Stein, N.; Grotzinger, J.P.; Schieber, J.; Mangold, N.; Newsom, H.; Minitti, M.; Sumner, D.; Edgett, K.S.; Stack, K.; Fedo, C.; et al. Facies Analysis and Basin Architecture of the Upper Part of the Murray Formation, Gale Crater, Mars. In Proceedings of the Lunar and Planetary Science Conference 48, Woodlands, TX, USA, 20–24 March 2017. Available online: <https://www.hou.usra.edu/meetings/lpsc2017/pdf/2387.pdf> (accessed on 3 May 2024).
73. Rampe, E.B.; Bristow, T.F.; Morris, R.V.; Morrison, S.M.; Achilles, C.N.; Ming, D.W.; Vaniman, D.T.; Blake, D.F.; Tu, V.M.; Chipera, S.J.; et al. Mineralogy of Vera Rubin Ridge from the Mars Science Laboratory CheMin Instrument. *J. Geophys. Res. Planets* **2020**, *125*, e2019JE006306. [CrossRef]
74. Stack, K.M.; Grotzinger, J.P.; Lamb, M.P.; Gupta, S.; Rubin, D.M.; Kah, L.C.; Edgar, L.A.; Fey, D.M.; Hurowitz, J.A.; McBride, M.; et al. Evidence for plunging river plume deposits in the Pahrump Hills member of the Murray formation, Gale crater, Mars. *Sedimentology* **2019**, *66*, 1768–1802. [CrossRef]
75. Rampe, E.; Ming, D.; Blake, D.; Bristow, T.; Chipera, S.; Grotzinger, J.; Morris, R.; Morrison, S.; Vaniman, D.; Yen, A.; et al. Mineralogy of an ancient lacustrine mudstone succession from the Murray formation, Gale crater, Mars. *Earth Planet. Sci. Lett.* **2017**, *471*, 172–185. [CrossRef]
76. Grotzinger, J.P.; Gupta, S.; Malin, M.C.; Rubin, D.M.; Schieber, J.; Siebach, K.; Sumner, D.Y.; Stack, K.M.; Vasavada, A.R.; Arvidson, R.E.; et al. Deposition, exhumation and paleoclimate of an ancient lake deposit, Gale crater, Mars. *Science* **2015**, *350*, aac7575. [CrossRef] [PubMed]
77. Murad, E.; Cashion, J. *Mössbauer Spectroscopy of Environmental Materials and Their Industrial Utilization*; Springer: New York, NY, USA, 2004. [CrossRef]
78. Jolivet, J.-P.; Tronc, E.J. Interfacial electron transfer in colloidal spinel iron oxide. Conversion of Fe₃O₄-γ-Fe₂O₃ in aqueous medium. *J. Colloid Interface Sci.* **1988**, *125*, 688–701. [CrossRef]
79. Hurowitz, J.A.; Grotzinger, J.P.; Fischer, W.W.; McLennan, S.M.; Milliken, R.E.; Stein, N.; Vasavada, A.R.; Blake, D.F.; Dehouck, E.; Eigenbrode, J.L.; et al. Redox stratification of an ancient lake in Gale crater, Mars. *Science* **2017**, *356*, eah6849. [CrossRef] [PubMed]
80. Martin, P.E.; Farley, K.A.; Baker, M.B.; Malespin, C.A.; Schwenger, S.P.; Cohen, B.A.; Mahaffy, P.R.; McAdam, A.C.; Ming, D.W.; Vasconcelos, P.M.; et al. A two-step K-Ar experiment on Mars: Dating the diagenetic formation of jarosite from Amazonian groundwaters. *J. Geophys. Res.—Planets* **2017**, *122*, 2803–2818. [CrossRef]
81. Marchesini, B.; Tavani, S.; Mercuri, M.; Mondillo, N.; Pizzati, M.; Balsamo, F.; Aldega, L.; Carminati, E. Structural control on the alteration and fluid flow in the lithocap of the Allumiere-Tolfa epithermal system. *J. Struct. Geol.* **2024**, *179*, 105035. [CrossRef]
82. Payré, V.; Siebach, K.; Thorpe, M.; Antoshechkina, P.; Rampe, E. Tridymite in a lacustrine mudstone in Gale Crater, Mars: Evidence for an explosive silicic eruption during the Hesperian. *Earth Planet. Sci. Lett.* **2022**, *594*, 117694. [CrossRef]
83. Yen, A.S.; Morris, R.V.; Ming, D.W.; Schwenger, S.P.; Sutter, B.; Vaniman, D.T.; Treiman, A.H.; Gellert, R.; Achilles, C.N.; Berger, J.A.; et al. Formation of tridymite and evidence for a hydrothermal history at gale crater, Mars. *J. Geophys. Res. Planets* **2021**, *126*, e2020JE006569. [CrossRef]
84. Watkins, J.A.; Grotzinger, J.P.; Stein, N.T.; Banham, S.G.; Gupta, S.; Rubin, D.M.; Morgan, K.S.; Edgett, K.S.; Frydenvang, J.; Siebach, K.L.; et al. Burial and Exhumation of Sedimentary Rocks Revealed by the Base Stimson Erosional Unconformity, Gale Crater, Mars. *J. Geophys. Res. Planets* **2022**, *127*, e2022JE007293. [CrossRef]
85. Banham, S.G.; Gupta, S.; Rubin, D.M.; Watkins, J.A.; Sumner, D.Y.; Edgett, K.S.; Grotzinger, J.P.; Lewis, K.W.; Edgar, L.A.; Stack-Morgan, K.M.; et al. Ancient Martian aeolian processes and palaeomorphology reconstructed from the Stimson formation on the lower slope of Aeolis Mons, Gale crater, Mars. *Sedimentology* **2018**, *65*, 993–1042. [CrossRef]
86. Banham, S.G.; Gupta, S.; Rubin, D.M.; Bedford, C.C.; Edgar, L.A.; Bryk, A.B.; Dietrich, W.E.; Fedo, C.M.; Williams, R.M.; Caravaca, G.; et al. Evidence for Fluctuating Wind in Shaping an Ancient Martian Dune Field: The Stimson Formation at the Greenheugh Pediment, Gale Crater. *J. Geophys. Res. Planets* **2022**, *127*, e2021JE007023. [CrossRef]
87. Yen, A.; Ming, D.; Vaniman, D.; Gellert, R.; Blake, D.; Morris, R.; Morrison, S.; Bristow, T.; Chipera, S.; Edgett, K.; et al. Multiple stages of aqueous alteration along fractures in mudstone and sandstone strata in Gale Crater, Mars. *Earth Planet. Sci. Lett.* **2017**, *471*, 186–198. [CrossRef]
88. Szczerba, M.; Rampe, E.B.; Peretyazhko, T.S.; Bristow, T.F.; Morris, R.V.; Blake, D.F.; Vaniman, D.T.; Chipera, S.J.; Downs, R.T.; Hazen, R.M.; et al. Hematite Formation and Growth in Gale crater Seen through MSL CheMin X-ray Diffraction Data. In Proceedings of the 54th Lunar and Planetary Science Conference 2023, Houston, TX, USA, 13–17 March 2023. Available online: <https://www.hou.usra.edu/meetings/lpsc2023/pdf/1956.pdf> (accessed on 3 May 2024).
89. Bibring, J.-P.; Langevin, Y.; Mustard, J.F.; Poulet, F.; Arvidson, R.; Gendrin, A.; Gondet, B.; Mangold, N.; Berthé, M.; Gomez, C.; et al. Global mineralogical and aqueous Mars history derived from OMEGA/Mars Express data. *Science* **2006**, *312*, 400–404. [CrossRef] [PubMed]
90. Ehlmann, B.L.; Edwards, C.S. Mineralogy of the Martian surface. *Annu. Rev. Earth Planet. Sci.* **2014**, *42*, 291–315. [CrossRef]

91. Murchie, S.L.; Mustard, J.F.; Ehlmann, B.L.; Milliken, R.E.; Bishop, J.L.; McKeown, N.K.; Dobrea, E.Z.N.; Seelos, F.P.; Buczkowski, D.L.; Wiseman, S.M.; et al. A synthesis of Martian aqueous mineralogy after 1 Mars year of observations from the Mars Reconnaissance Orbiter. *JGR Planets* **2009**, *114*, E2. [CrossRef]
92. Bishop, J.L.; Lane, M.D.; Dyar, M.D.; Brown, A.J. Reflectance and emission spectroscopy study of four groups of phyllosilicates: Smectites, kaolinite-serpentines, chlorites and mica. *Clay Miner.* **2008**, *43*, 35–54. [CrossRef]
93. Grant, J.A.; Irwin, R.P., III; Grotzinger, J.P.; Milliken, R.E.; Tornabene, L.L.; McEwen, A.S.; Weitz, C.M.; Squyres, S.W.; Glotch, T.D.; Thompson, B.J. HiRISE imaging of impact megabreccia and sub-meter aqueous strata in Holden Crater, Mars. *Geology* **2008**, *36*, 195–198. [CrossRef]
94. Milliken, R.E.; Bish, D.L. Sources and sinks of clay minerals on Mars. *Philos. Mag.* **2010**, *90*, 2293–2308. [CrossRef]
95. Fedo, C.M.; Bryk, A.B.; Edgar, L.A.; Bennett, K.A.; Fox, V.K.; Dietrich, W.E.; Banham, S.G.; Gupta, S.; Stack, K.M.; Williams, R.M.E.; et al. Geology and stratigraphic correlation of the Murray and Carolyn Shoemaker formations across the Glen Torridon region, Gale crater, Mars. *J. Geophys. Res. Planets* **2022**, *127*, e2022JE007408. [CrossRef]
96. Downs, R.T.; Hall-Wallace, M. The American Mineralogist crystal structure database. *Am. Miner.* **2003**, *95*, 247–250. [CrossRef]
97. Sheppard, R.Y.; Milliken, R.E.; Parente, M.; Itoh, Y. Updated perspectives and hypotheses on the mineralogy of lower Mt. Sharp, Mars, as seen from orbit. *J. Geophys. Res. Planets* **2021**, *126*, e2020JE006372. [CrossRef]
98. Rampe, E.B.; Bristow, T.F.; Blake, D.F.; Chipera, S.J.; Vaniman, D.T.; Achilles, C.N.; Downs, R.T.; Ming, D.W.; Morris, R.V.; Morrison, S.M.; et al. Mineralogical Evidence for Environmental Change in the Clay-Sulfate Transition at Gale crater, Mars. In Proceedings of the 54th Lunar and Planetary Science Conference 2023, Houston, TX, USA, 13–17 March 2023; Available online: <https://www.hou.usra.edu/meetings/lpsc2023/pdf/1554.pdf> (accessed on 3 May 2024).
99. Chipera, S.J.; Chipera, S.J.; Vaniman, D.T.; Vaniman, D.T.; Rampe, E.B.; Rampe, E.B.; Bristow, T.F.; Bristow, T.F.; Martínez, G.; Martínez, G.; et al. Mineralogical Investigation of Mg-Sulfate at the Canaima Drill Site, Gale Crater, Mars. *JGR Planets* **2023**, *128*, e2023JE008041. [CrossRef]
100. Chipera, S.J.; Vaniman, D.T. Experimental stability of magnesium sulfate hydrates that may be present on Mars. *Geochim. Cosmochim. Acta* **2007**, *71*, 241–250. [CrossRef]
101. Vaniman, D.T.; Chipera, S.J. Transformations of Mg-and Ca-sulfate hydrates in Mars regolith. *Am. Miner.* **2006**, *91*, 1628–1642. [CrossRef]
102. Vaniman, D.T.; Chipera, S.J.; Bish, D.L.; Peterson, R.C. The Todilto Formation and Science Goals at North Meridiani. In Proceedings of the 7th International Conference on Mars, Houston, TX, USA, 9–13 July 2007. LPI Contribution No. 1353; Bibcode: 2007LPICo1353.3156V.
103. Wang, A.; Freeman, J.J.; Jolliff, B.L. Formation Rate of Amorphous Magnesium Sulfates at Low Temperatures Approaching the Current Surface Conditions on Mars. In Proceedings of the LPSC 38, Houston, TX, USA, 12–16 March 2007; Available online: <https://www.lpi.usra.edu/meetings/lpsc2007/pdf/1195.pdf> (accessed on 3 May 2024).
104. Wang, A.; Freeman, J.J.; Jolliff, B.L. Phase transition pathways of the hydrates of magnesium sulfate in the temperature range 50 °C to 5 °C: Implication for sulfates on Mars. *J. Geophys. Res.* **2009**, *114*, E04010. [CrossRef]
105. Wang, A.; Freeman, J.J.; Chou, I.-M.; Jolliff, B.L. Stability of Mg-sulfates at –10 °C and the rates of dehydration/rehydration processes under conditions relevant to Mars. *J. Geophys. Res.* **2011**, *116*, E12006. [CrossRef]
106. Vaniman, D.T.; Martinez, G.M.; Rampe, E.B.; Bristow, T.F.; Blake, D.F.; Yen, A.S.; Ming, D.W.; Rapin, W.; Meslin, P.-Y.; Morookian, J.M.; et al. Gypsum, bassanite, and anhydrite at Gale crater, Mars. *Am. Miner.* **2018**, *103*, 1011–1020. [CrossRef]
107. Vaniman, D.T.; Chipera, S.J.; Martinez, G.; Rapin, W.; Rampe, E.B.; Bristow, T.; Blake, D.F.; Meusberger, J.; Ming, D.W.; Downs, R.T.; et al. Near-Surface Dehydration of Salt Hydrates at Gale Crater, Mars. In Proceedings of the 55th LPSC 2024, Houston, TX, USA, 11–15 March 2024. Available online: <https://www.hou.usra.edu/meetings/lpsc2024/pdf/1327.pdf> (accessed on 3 May 2024).
108. Gellert, R.; Clark, B.C., III. The MER Science Teams. In Situ Compositional Measurements of Rocks and Soils with the Alpha Particle X-ray Spectrometer on NASA's Mars Rovers. *Elements* **2015**, *11*, 39–44. [CrossRef]
109. Rapin, W.; Meslin, P.-Y.; Maurice, S.; Wiens, R.; Laporte, D.; Chauviré, B.; Gasnault, O.; Schröder, S.; Beck, P.; Bender, S.; et al. Quantification of water content by laser induced breakdown spectroscopy on Mars. *Spectrochim. Acta Part B At. Spectrosc.* **2017**, *130*, 82–100. [CrossRef]
110. McLennan. Sedimentary silica on Mars. *Geology* **2003**, *31*, 315–318. [CrossRef]
111. Squyres, S.W.; Arvidson, R.E.; Ruff, S.; Gellert, R.; Morris, R.V.; Ming, D.W.; Crumpler, L.; Farmer, J.D.; Marais, D.J.D.; Yen, A.; et al. Detection of Silica-Rich Deposits on Mars. *Science* **2008**, *320*, 1063–1067. [CrossRef]
112. McLennan, S.; Bell, J.F., III; Calvin, W.; Christensen, P.; Clark, B.; de Souza, P.; Farmer, J.; Farrand, W.; Fike, D.; Gellert, R.; et al. Provenance and diagenesis of the evaporite-bearing Burns formation, Meridiani Planum, Mars. *Earth Planet. Sci. Lett.* **2005**, *240*, 95–121. [CrossRef]
113. Milliken, R.; Swayze, G.; Arvidson, R.; Bishop, J.; Clark, B.; Ehlmann, B.; Green, R.; Grotzinger, J.; Morris, R.; Murchie, S.; et al. Opaline silica in young deposits on Mars. *Geology* **2008**, *36*, 847–850. [CrossRef]
114. Maliva, R.G.; Knoll, A.H.; Siever, R. Secular Change in Chert Distribution: A Reflection of Evolving Biological Participation in the Silica Cycle. *Palaios* **1989**, *4*, 519–532. [CrossRef] [PubMed]
115. Tosca, N.J.; Knoll, A.H. Juvenile chemical sediments and the long-term persistence of water at the surface of Mars. *Earth Planet. Sci. Lett.* **2009**, *286*, 379–386. [CrossRef]

116. Achilles, C.N.; Rampe, E.B.; Downs, R.T.; Bristow, T.F.; Ming, D.W.; Morris, R.V.; Vaniman, D.T.; Blake, D.F.; Yen, A.S.; McAdam, A.C.; et al. Evidence for multiple diagenetic episodes in ancient fluvial-lacustrine sedimentary rocks in Gale crater, Mars. *JGR Planets* **2020**, *125*, e2019JE006295. [[CrossRef](#)] [[PubMed](#)]
117. Dehouck, E.; Gaudin, A.; Mangold, N.; Lajaunie, L.; Dauzères, A.; Grauby, O.; Le Menn, E. Weathering of olivine under CO₂ atmosphere: A martian perspective. *Geochim. Cosmochim. Acta* **2014**, *135*, 170–189. [[CrossRef](#)]
118. Smith, R.J.; McLennan, S.M.; Achilles, C.N.; Dehouck, E.; Horgan, B.H.N.; Mangold, N.; Rampe, E.B.; Salvatore, M.; Siebach, K.L.; Sun, V. X-ray Amorphous Components in Sedimentary Rocks of Gale Crater, Mars: Evidence for Ancient Formation and Long-Lived Aqueous Activity. *JGR Planets* **2021**, *126*, e2020JE006782. [[CrossRef](#)]
119. Smith, R.J.; McLennan, S.M.; Sutter, B.; Rampe, E.B.; Dehouck, E.; Siebach, K.L.; Horgan, B.H.N.; Sun, V.; McAdam, A.; Mangold, N.; et al. X-ray Amorphous Sulfur-Bearing Phases in Sedimentary Rocks of Gale Crater, Mars. *JGR Planets* **2022**, *127*, e2021JE007128. [[CrossRef](#)]
120. Sutter, B.; McAdam, A.C.; Mahaffy, P.R.; Ming, D.W.; Edgett, K.S.; Rampe, E.B.; Eigenbrode, J.L.; Franz, H.B.; Freissinet, C.; Grotzinger, J.P.; et al. Evolved gas analyses of sedimentary rocks and eolian sediment in Gale Crater, Mars: Results of the Curiosity rover's sample analysis at Mars instrument from Yellowknife Bay to the Namib Dune. *JGR Planets* **2017**, *122*, 2574–2609. [[CrossRef](#)]
121. Grotzinger, J.; Beaty, D.; Dromart, G.; Gupta, S.; Harris, M.; Hurowitz, J.; Kocurek, G.; McLennan, S.; Milliken, R.; Ori, G.G.; et al. Mars sedimentary geology: Key concepts and outstanding questions. *Astrobiology* **2011**, *11*, 77–87. [[CrossRef](#)]
122. Day, M.; Kocurek, G. Observations of an aeolian landscape: From surface to orbit in Gale Crater. *Icarus* **2016**, *280*, 37–71. [[CrossRef](#)]
123. Kite, E.S.; Lewis, K.W.; Lamb, M.P.; Newman, C.E.; Richardson, M.I. Growth and form of the mound in Gale Crater, Mars: Slope wind enhanced erosion and transport. *Geology* **2013**, *41*, 543–546. [[CrossRef](#)]
124. Borlina, C.S.; Ehlmann, B.L.; Kite, E.S. Modeling the thermal and physical evolution of Mount Sharp's sedimentary rocks, Gale Crater, Mars: Implications for diagenesis on the MSL Curiosity rover traverse. *J. Geophys. Res. Planets* **2015**, *120*, 1396–1414. [[CrossRef](#)]
125. Lewis, K.W.; Peters, S.; Gonter, K.; Morrison, S.; Schmerr, N.; Vasavada, A.R.; Gabriel, T. A surface gravity traverse on Mars indicates low bedrock density at Gale crater. *Science* **2019**, *363*, 535–537. [[CrossRef](#)] [[PubMed](#)]
126. Palucis, M.C.; Dietrich, W.E.; Williams, R.M.E.; Hayes, A.G.; Parker, T.; Sumner, D.Y.; Mangold, N.; Lewis, K.; Newsom, H. Sequence and relative timing of large lakes in Gale crater (Mars) after the formation of Mount Sharp. *J. Geophys. Res. Planets* **2016**, *121*, 472–496. [[CrossRef](#)]
127. National Academies of Sciences, Engineering, and Medicine. *Origins, Worlds, and Life: A Decadal Strategy for Planetary Science and Astrobiology 2023–2032*; The National Academies Press: Washington, DC, USA, 2022. [[CrossRef](#)]
128. Hazen, R.M.; Downs, R.T.; Morrison, S.M.; Tutolo, B.M.; Blake, D.F.; Bristow, T.F.; Chipera, S.J.; McSween, H.Y.; Ming, D.; Morris, R.V.; et al. On the Diversity and Formation Modes of Martian Minerals. *JGR Planets* **2023**, *128*, e2023JE007865. [[CrossRef](#)]
129. Hazen, R.M.; Papineau, D.; Bleeker, W.; Downs, R.T.; Ferry, J.M.; McCoy, T.J.; Sverjensky, D.A.; Yang, H. Mineral evolution. *Am Miner.* **2008**, *93*, 1693–1720. [[CrossRef](#)]
130. Hazen, R.M.; Morrison, S.M. On the paragenetic modes of minerals: A mineral evolution perspective. *Am. Miner.* **2022**, *107*, 1262–1287. [[CrossRef](#)]
131. Grant, J.A.; Golombek, M.P.; Parker, T.J.; Crisp, J.A.; Squyres, S.W.; Weitz, C.M. Selecting landing sites for the 2003 Mars Exploration Rovers. *Planet. Space Sci.* **2004**, *52*, 11–21. [[CrossRef](#)]
132. Grant, J.A.; Golombek, M.P.; Grotzinger, J.P.; Wilson, S.A.; Watkins, M.M.; Vasavada, A.R.; Griffes, J.L.; Parker, T.J. The science process for selecting the landing site for the 2011 Mars Science Laboratory. *Planet. Space Sci.* **2011**, *59*, 1114–1127. [[CrossRef](#)]
133. Grant, J.A.; Golombek, M.P.; Wilson, S.A.; Farley, K.A.; Williford, K.H.; Chen, A. The science process for selecting the landing site for the 2020 Mars rover. *Planet. Space Sci.* **2018**, *164*, 106–126. [[CrossRef](#)]
134. Farley, K.A.; Williford, K.H.; Stack, K.M.; Bhartia, R.; Chen, A.; de la Torre, M.; Hand, K.; Goreva, Y.; Herd, C.D.K.; Hueso, R.; et al. Mars 2020 Mission Overview. *Space Sci. Rev.* **2020**, *216*, 142. [[CrossRef](#)]
135. Rampe, E.B.; Bristow, T.F.; Blake, D.F.; Vaniman, D.T.; Chipera, S.J.; Downs, R.T.; Ming, D.W.; Morris, R.V.; Tu, V.M.; Thorpe, M.T.; et al. Mineralogical trends over the clay-sulfate transition in Gale Crater from the Mars Science Laboratory CheMin instrument. In Proceedings of the 53rd Lunar and Planetary Science Conference, Woodlands, TX, USA, 7–11 March 2022; Available online: <https://www.hou.usra.edu/meetings/lpsc2022/pdf/1532.pdf> (accessed on 3 May 2024).
136. Rampe, E.B.; Sarrazin, P.; Blake, D.F.; Bristow, T.F.; Yen, A.S.; Downs, R.T.; Tu, V.M.; Zacny, K.; Lafuente, B.; Thompson, K.; et al. Advances in X-ray Instruments to Support Mars Sample Return. In Proceedings of the 55th Lunar and Planetary Science Conference, Woodlands, TX, USA, 11–15 March 2024. Available online: <https://www.hou.usra.edu/meetings/lpsc2024/pdf/1510.pdf> (accessed on 3 May 2024).
137. Anderson, R.B.; Bell, J.F., III. Geologic mapping and characterization of Gale Crater and implications for its potential as a Mars Science Laboratory landing site. *Int. J. Mars Sci. Explor.* **2010**, *5*, 76–128. [[CrossRef](#)]
138. Siebach, K.L.; Grotzinger, J.P. Volumetric estimates of ancient water on Mount Sharp based on boxwork deposits, Gale Crater, Mars. *JGR Planets* **2013**, *119*, 189–198. [[CrossRef](#)]

Disclaimer/Publisher's Note: The statements, opinions and data contained in all publications are solely those of the individual author(s) and contributor(s) and not of MDPI and/or the editor(s). MDPI and/or the editor(s) disclaim responsibility for any injury to people or property resulting from any ideas, methods, instructions or products referred to in the content.